Y-NBS: Surveying Star Formation from the Epoch of Reionisation to the Local Universe

Heather Phoenix Wade

Physics
Department of Physics
Lancaster University

April 18, 2024

A thesis submitted to Lancaster University for the degree of
Doctor of Philosophy in the Faculty of Science and Technology

Supervised by
Dr. Julie Wardlow
Dr. David Sobral

Abstract

The first galaxies, inside the epoch of reionisation, are very different to those locally (13.7 billion years later) and understanding this evolution is one of the most fundamental areas of research in observational astrophysics. The star formation history of the Universe probes the growth of galaxies and shows that the star formation rate densities (SFRD) of galaxies increase from the early Universe, during the epoch of reionisation, until it peaks at $z = 2 - 3$, at cosmic noon. After cosmic noon, the star formation rate density of galaxies decreases to the present day. To understand this evolution and its causes requires measuring the evolving SFRD for different types of galaxies. One method to probe the Universe and its star formation history is to select samples of line emitting galaxies in a self-consistent way. In this work, we present a wide-area narrowband survey, Y-NBS, conducted on VLT/HAWK-I with the NB1060 filter in the COSMOS field. We complement this with a deeper archival VLT/HAWK-I pointing covering GOODS-S. We present the full data reduction pipeline for the COSMOS data and then combine it with complementary broadband and redshift data. Using spectroscopic redshifts, photometric redshifts and colour-colour selection, we select samples of Hα, [OIII] and [OII] emitting galaxies at $z = 0.62$, $z = 1.12$ and $z = 1.85$, respectively. Luminosity functions of these samples are plotted and Schechter functions are fitted with all three parameters free, which is only possible due to our simultaneously wide survey with deep regions. Our results for the faint-end slope (α) are $\alpha = -1.48^{+0.17}_{-0.17}$, $-1.95^{+0.18}_{-0.15}$ and $-2.43^{+0.19}_{-0.16}$ for Hα, [OIII] and [OII] respectively. Our measurements are consistent with previous studies of these luminosity functions at similar redshifts but we probe deeper or over a wider range of luminosities than many other surveys. Star formation rate densities calculated from our luminosity functions are consistent with others, but our [OII] result is ~ 0.3 dex higher than expected, likely because we observed a steeper faint-end slope than other surveys. Y-NBS also targets $z = 7.7$ Lyα emitters, probing into the epoch of reionisation. Although we do not find any, we place robust constraints on the $z = 7.7$ Lyα luminosity function, which are in agreement with spectroscopically confirmed sources at this redshift. We constrain the neutral fraction of hydrogen to be $\chi_{HI} > 0.4$ at $z = 7.7$, which is consistent with previous studies at $z = 7.0 - 7.3$. Overall, our work highlights the need for future narrowband surveys to be wide *and* deep, specifically in the same field, to help overcome cosmic variance and to simultaneously constrain both the faint and bright ends of the luminosities functions. If the deep and shallow regions were in the same field, it would help to rule out the possibility that any observed differences in the density betweeen the deep and shallow regions were the result of cosmic variance. Such work would further our understanding of the star formation history of the Universe from the epoch of reionisation, through cosmic noon, to the local Universe.

To Lilly, forever my baby sister and always a source of inspiration.

Acknowledgements

There are simply too many people to thank for making this thesis possible.

But first of all, the science: a huge thank you to David Sobral and Julie Wardlow, especially to Julie for adopting me even though I'm mean about your lack of pop culture references! Thank you for being such a great guide through the last few years, for working so hard to get this thesis finished, for always motivating and encouraging me and for reducing the silly number of times that I write 'we' or start a new paragraph or subsection unnecessarily.

Lancaster University has been my home for eight years now, and a huge part of that time has been with the Observational Astrophysics Group. To Isobel Hook, John Stott, Brooke Simmons, Julie Wardlow, David Sobral, Matthew Pitkin, Danil Kuzin, Klaas Wiersema and Young-Lo Kim: thank you for being the heart of the department and being great role models. A special thank you is needed for John Stott for being the greatest ever MPhys supervisor and encouraging this whole PhD malarkey to come about! Thank you to my wonderful office mates, past and present: João Calhau (for throwing me in at the deep end), Sergio Santos (whose thesis has been a saviour these past months), Emma Dodd (always my favourite astro girly), Jon Carrick, Matthew Chan, Matthew Fahey, David O'Ryan, Rahul Rana, Jamie Dumayne, Harry Stephenson, Andrew Milligan and Evie Day. The highlight of my time as a PhD student was observing in La Palma, so a special thank you goes to the best observing companions around: Tom Cornish, Aruba Mohammed, Amy Hewitt, Izzy Garland, Matthew Thorne, Pascale Desmet and of course, Nick Amos, wizard of the Isaac Newton Telescope. This group has been so kind and supportive and I loved every second of being a part of it. I feel like no future work

social I go to will be as good as ours were. To all future Lancaster Observation Astrophysics group members: you're in good hands.

A huge thank you to all of my co-authors for your guidance and helping to get this work get into a good science level: Jorryt Matthee, Brooke Simmons, Ana Paulino-Afonso, Ali Khostovan and Ian Smail. Thank you for STFC and Lancaster University's FST for the funding.

To my friends, near and far, who have helped distract me from the horrors of data reduction and thesis writing: Phil, Jack F, Elle, Juliane, Elizabeth, Jo, Alex, Ciarán, Jack B, Pascale, Isabella, Emma, Amaia, Katherine, Christine, Adam, Becca and baby Freya. Thank you for your friendship.

And of course, my source of constant support and love through the PhD and my whole life: my family. Thank you to my parents, my Nana and Lilly, for visiting Lancaster and buying me lunch, for listening to my near-constant complaints and, most importantly, for encouraging me to be anything I want to be.

And finally, to Tom Cornish, without whom none of this would have been possible. I love you to the moon and to Saturn.

Declaration

This thesis is my own work and no portion of the work referred to in this thesis has been submitted in support of an application for another degree or qualification at this or any other institute of learning.

Chapter 2, Sections 2.1.2.1, 2.1.2.2 and sections 2.3 to 2.5.2.3 inclusive and Chapter 3 are based on the paper '*Y-band Narrowband Survey in COSMOS (Y-NBS): the constrained faint end slopes of the Hα, [OIII] and [OII] luminosity functions*' by Wade et al.. This paper is awaiting the 2nd round of co-author comments before being submitted to *MNRAS*.

Chapter 4 is based on the paper '*Y-NBS in the epoch of reionisation: the Lyα luminosity function at* $z = 7.7$' by Wade et al.. This paper is awaiting co-author comments before being sent to *MNRAS* for the reviewing process.

“No woman should be made to fear that she was not enough.”

- *The Priory of the Orange Tree*, Samantha Shannon

“Yay space!”

- *Barbie* (2023), written and directed by Greta Gerwig

Contents

List of Figures

List of Tables

Relevant Publications by the Author

Chapter 2 and 3

- "Y-band Narrowband Survey in COSMOS (Y-NBS): the constrained faint-end slopes of the Hα, [OIII] and [OII] luminosity functions"; **Wade H.**, Cornish T., Wardlow J., Sobral D., Matthee J., Khostovan A., Paulino-Afonso A., Simmons B. (**in prep.**)

Chapter 4

- "Y-NBS in the epoch of reionisation: the Lyα luminosity function at $z = 7.7$"; **Wade H.**, Cornish T., Wardlow J., Sobral D., Matthee J., Khostovan A. (**in prep.**)

Chapter 1

Introduction

From early civilisations constructing stories from the constellations, to the discovery of galaxies beyond our own, to modern telescopes finding the most distant objects known to humanity, astrophysics is a fundamental part of science and the human experience. Pushing towards an understanding of the origins and evolution of the Universe is a complex problem but each day the astrophysics community takes one step closer. This chapter introduces some of the key concepts of observational astrophysics and offers a glimpse at our current understanding of the Universe, including galaxy evolution, the star formation history of the Universe and the epoch of reionisation.

1.1 A Brief Synopsis of the Universe

1.1.1 Cosmological Overview

Cosmology is the framework upon which our study of galaxies lies, as it sets the initial conditions for the observable Universe to evolve from. The current 'standard model' of Big Bang cosmology is the ΛCDM model (Λ Cold Dark Matter). The ΛCDM model splits the Universe into three components: Λ, Cold Dark Matter and ordinary matter. Λ is the cosmological constant which accounts for dark energy and explains the accelerating expansion of the Universe (Perlmutter et al.

1999; Riess et al. 1998). Cold Dark Matter is hypothesised to be non-baryonic, cold and collisionless matter. Ordinary matter is that which we interact with daily and can directly observe in stars and galaxies. ΛCMD follows the cosmological principle: at large scales the Universe is homogeneous (the same at all positions) and isotropic (the same in all directions).

The model can also explain important properties of our Universe, such as its accelerating expansion, the creation and anisotropy (directional dependence) of the Cosmic Microwave Background (CMB, Penzias & Wilson 1965; Planck Collaboration et al. 2020) and the cosmic web of galaxy structure.

In the cosmological model there are three main parameters: H_0 is the Hubble constant which describes the current rate of expansion of the Universe, Ω_M is the density parameter for matter, and Ω_Λ is the density parameter for dark energy. The cosmological model used affects this thesis as the parameters are used to calculate values such as luminosity and volume. Although recent results from Planck Collaboration et al. (2020) place new constraints on these values, we use $H_0 = 70\,\mathrm{kms}^{-1}\ \mathrm{Mpc}^{-1}$, $\Omega_M = 0.3$ and $\Omega_\Lambda = 0.7$ to allow for direct comparison with other results that also use this cosmology. These values mean that the Universe is 70% dark energy and 30% matter, including dark matter, baryonic matter and radiation.

1.1.2 Timeline of the Universe

Figure 1.1 shows a visual timeline of the Universe, according the ΛCDM cosmology and observations. It begins with the Big Bang, a model that suggests that the Universe was initially an extremely dense and hot singularity which then began to expand, becoming less dense and cooling down. Inflation was a short period just 10^{-36} seconds after the Big Bang during which the Universe expanded exponentially and cooled significantly (Guth 1981). On cosmological scales, the Universe can be considered homogenous. However, the non-uniform distribution of galaxies across the sky shows that the Universe is inhomogeneous on small scales. It is thought that the process of inflation magnified the early quantum fluctuations into the large scale structures of the Universe.

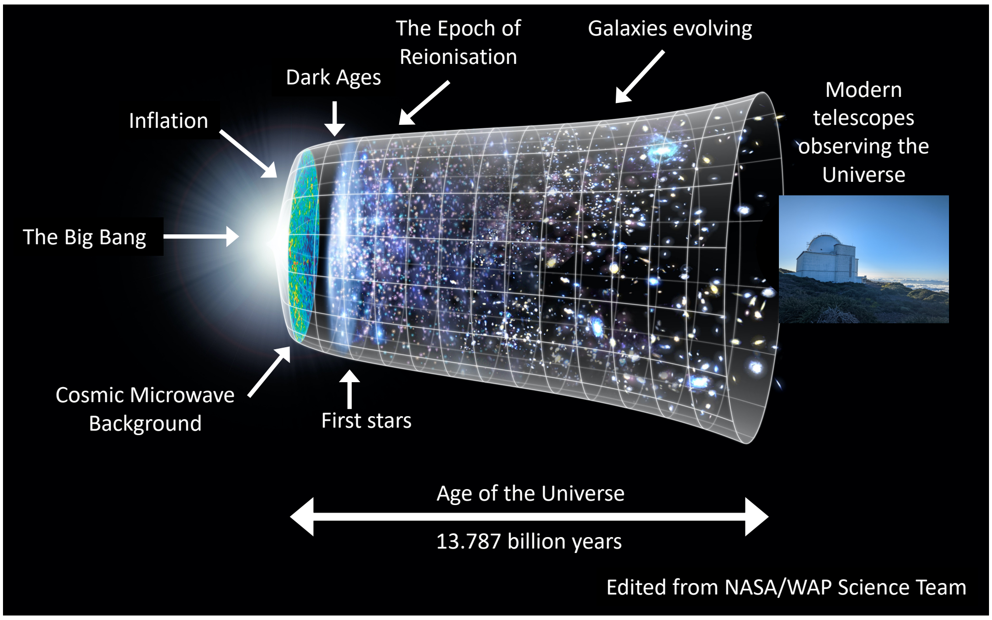

Figure 1.1: Illustration of the Universe from the Big Bang through to nearby galaxies. The telescope pictured on the right is the Isaac Newton Telescope in La Palma, photographed by me during an observing run in May 2022. (Main diagram edited from the NASA/WAP Science Team.)

The Cosmic Microwave Background (CMB) is an observable afterglow of a period early in the Universe's history, but after inflation (e.g. Penzias & Wilson 1965). As the Universe expanded it also cooled and eventually, at around $z \sim 1100$, or ~ 0.4 million years after the Big Bang, the Universe was cool enough for the decoupled electrons and protons to combine into neutral hydrogen in a process called recombination. Recombination was the first major phase transition of hydrogen and enabled photons to travel freely to eventually reach our telescopes.

The formation of the CMB is followed by the cosmic dark ages, so-called because there are no new sources of light. During this period structure began to form as dark matter gravitationally collapsed into filaments, with baryonic matter following and cooling until the conditions for the first stars to form are met (e.g. Davis et al. 1985; Peebles 1982; Press & Schechter 1974).

We have not yet observed the first stars directly and unambiguously. They likely formed around 0.2 billion years after the Big Bang, when the density perturbations allowed gravity to dominate and matter was gravitationally drawn into high density regions of space (e.g. Abel et al. 2002). In these dense regions, with gravitational attraction, the matter formed stars and eventually galaxies. For more on how galaxies form see Section 1.2. Stars form when clouds of gas and dust undergo gravitational collapse due to becoming too massive to be in a state of hydrostatic equilibrium. The increased gravity and density of the collapsed cloud forms a dense core, which gravitationally attracts more dust and gas. When the core is dense enough, fusion can begin whereby the hydrogen is fused into helium, emitting significant amounts of energy.

The first galaxies are somewhat obscured from view due to the neutral hydrogen surrounding them, as this scatters photons so that they cannot reach us. By around $z \sim 6$ (Fan et al. 2006) the epoch of reionisation has ended and the IGM is now neutral, marking the second and last major phase transition of hydrogen. High-energy, ionising UV photons from AGN, massive stars, faint galaxies and bright galaxies all likely helped to ionise the Universe's hydrogen. After reionisation was complete the full spectrum of light could travel through the Universe without being scattered by neutral hydrogen. The epoch of reionisation is still yet to be fully constrained and understood; see Section 1.3 for more detail.

From $z \sim 6$ to $z \sim 0$, galaxies evolve: forming stars from gas, merging with nearby galaxies, falling into galaxy clusters or simply evolving into spiral galaxies like our Milky Way. Section 1.2 discusses galaxy evolution in more detail.

Which finally leads us to us! Now humanity is observing back into the 13.787 Gyrs (Planck Collaboration et al. 2020) of history that the Universe has to offer, with cutting-edge technology that improves significantly decade on decade.

1.2 Galaxy Formation and Evolution

Since Edwin Hubble first realised that the 'spiral nebulae' observed in the sky were actually galaxies outside of our own (Hubble 1926) almost 100 years ago, extragalactic astrophysicists have studied the vast variations in galaxies, for example: masses, colours, morphologies and star formation rates. This section discusses how galaxies form and evolve from the early Universe to the local Universe, and describes some of the important properties of galaxies.

As mentioned in Section 1.1.2, during the cosmic dark ages dark matter gravitationally collapses to form haloes and then filaments. This process follows a ‘hierarchical paradigm’, meaning that low mass dark matter haloes form first, then these merge together to create larger haloes and filaments with time (e.g. Davis et al. 1985; Peebles 1982; Press & Schechter 1974).

Galaxies are made up from gas, stars and dust, all surrounded by a dark matter halo, whose presence we can infer from galaxy rotation curves (e.g. Navarro et al. 1996; Rubin et al. 1980), amongst other things. The baryonic mass then traces the gravitational potential well created by the dark matter halo. The movement from the infall causes an increase in the pressure, causing the gas to be shock heated and expand to fill the halo. Eventually, the gas cools enough to form the first generation of stars.

1.2.1 The First Stars and Galaxies

It is thought that the first stars, called Population III stars, likely had very different compositions and lifetimes compared to our Sun and other stars in the Milky Way. This is because the gas clouds they formed from only contained hydrogen and helium; heavier elements had not yet been synthesised in stars and distributed by supernovae. The metallicity of a star or galaxy is a measure of how abundant metals (elements heavier than helium) are within the object. Due to the early stars having low metallicities, they were very inefficient at cooling (e.g. Palla et al. 1983; Silk 1977) so they could grow to be massive: $\sim 100 - 1000 M_\odot$ (e.g. Nakamura & Umemura 2001), though some authors suggest that fragmentation could lead to lower mass Population III stars (e.g. Bromm & Larson 2004). If massive, these stars were also highly luminous and therefore short-lived. The death of these early stars formed some of the heavier elements, meaning that the next generation of stars were made from this enriched gas. The properties of Population III stars make them potential candidates for reionisation – they emitted a large amount of ionising radiation in a short time (e.g. Couchman & Rees 1986; Fukugita & Kawasaki 1994; Ostriker & Gnedin 1996).

The very first galaxies are challenging to observe as current facilities cannot yet probe to low enough fluxes to detect such distant, faint, compact objects (Bromm

& Yoshida 2011). However, samples of bright early galaxies have been identified, specifically with wide-field ground-based surveys (e.g. Bowler et al. 2014; Hu et al. 2016; Jiang et al. 2017; Matthee et al. 2015; Santos et al. 2016; Shibuya et al. 2017; Zheng et al. 2017), and they can provide an insight into the very early Universe. The Hubble Space Telescope and JWST have smaller fields of view than many ground-based telescopes but still yield samples of bright early galaxies with both imaging and spectroscopy (e.g. Bouwens et al. 2015; Bowler et al. 2017a; Bunker et al. 2023; Finkelstein et al. 2023). By observing the ultraviolet slopes of these high-redshift galaxies, it has been observed that they are relatively dust free (e.g. Dunlop et al. 2012; Ota et al. 2014; Schaerer et al. 2015; Wilkins et al. 2016). They have also been observed to have multiple components (more than one 'blob' in the structure) in rest-frame ultraviolet observations (e.g. Bowler et al. 2017a; Matthee et al. 2017b; Sobral et al. 2015b) and in the rest-frame far-infrared (e.g. Carniani et al. 2018; Jones et al. 2017; Maiolino et al. 2015; Matthee et al. 2017c). These irregular structures tend to be smaller than more local galaxies (Section 1.2.2), and as they have been selected via their brightness, they are intensely star-forming (Sobral et al. 2017); instrument limitations stop us from understanding the star-formation rates of the full population of galaxies at high-redshift.

More specifically, we can study individual high-redshift galaxies with multiple telescopes across multiple wavelengths to understand them in great detail. For example, the galaxy CR7 (COSMOS Redshift 7, Matthee et al. 2015; Sobral et al. 2015b) is at $z = 6.6$ and is one of the brightest known galaxies in the early Universe. Since its discovery with a narrowband survey using Subaru it has had follow-up observations with *HST*, ALMA and the VLT. Figure 1.2 (originally from Sobral et al. (2019)) shows CR7 and all the information that these telescopes have unveiled. *HST* observations (the greyscale background image in Figure 1.2) show that CR7 is formed of three UV clumps labelled A, B and C in order of decreasing brightness. The dynamical masses of these clumps were also estimated via the ALMA data, which each being on the order of $10^{10} M_{\odot}$. ALMA observations of the [CII] emission (red, green and cyan contours) of this galaxy confirmed the redshifts of these three clumps, confirming that they are all in the same system. The blue contours show the Lyα halo (the extended Lyα emission region due to scattering)

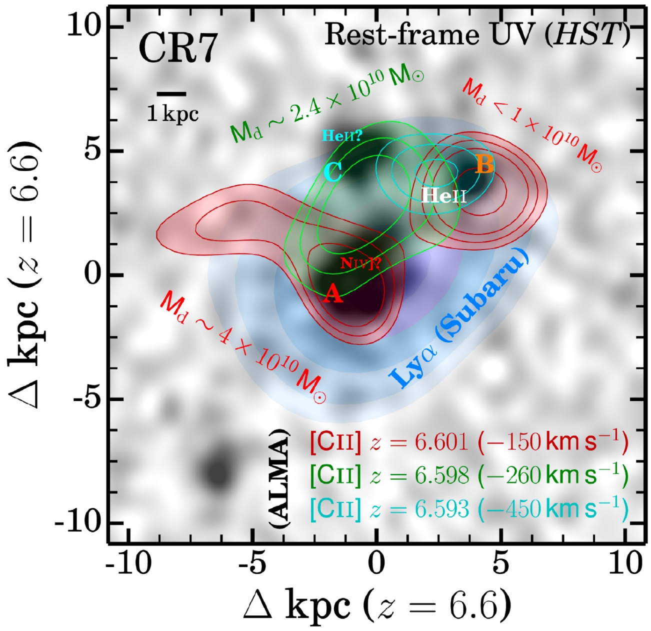

Figure 1.2: Multi-wavelength analysis of the galaxy CR7 ($z = 6.6$) from *HST*, Subaru, ALMA and the VLT, showing three main clumps and their masses, [CII] emission, a Lyα blob and and a HeII region. (From Sobral et al. (2019).)

observed with Subaru. This region is overlapping with the *HST* clumps, showing that the strongest Lyα emission aligns with the strongest UV emission. Using the X-SHOOTER instrument on the VLT, HeII and potential NV emission was observed, with some of the HeII emission misaligned from clump B, suggesting the possibility of a fourth component. Clearly, CR7 is a very complex system and multi-wavelength analysis has unlocked a wealth of knowledge about it. (This analysis is summarised from Sobral et al. (2019) and uses data presented in Sobral et al. (2015b) and Matthee et al. (2017b).) Galaxies in the early Universe are unknown entities and observing them in many wavelengths reveales more about the high-redshift Universe.

1.2.2 Galaxy Morphologies

The local Universe is very different to the high-redshift Universe. In terms of galaxy morphology CR7, (Section 1.2.1) is very different in shape to the spiral nature of the Milky Way and other local galaxies like M87. Local galaxies (those

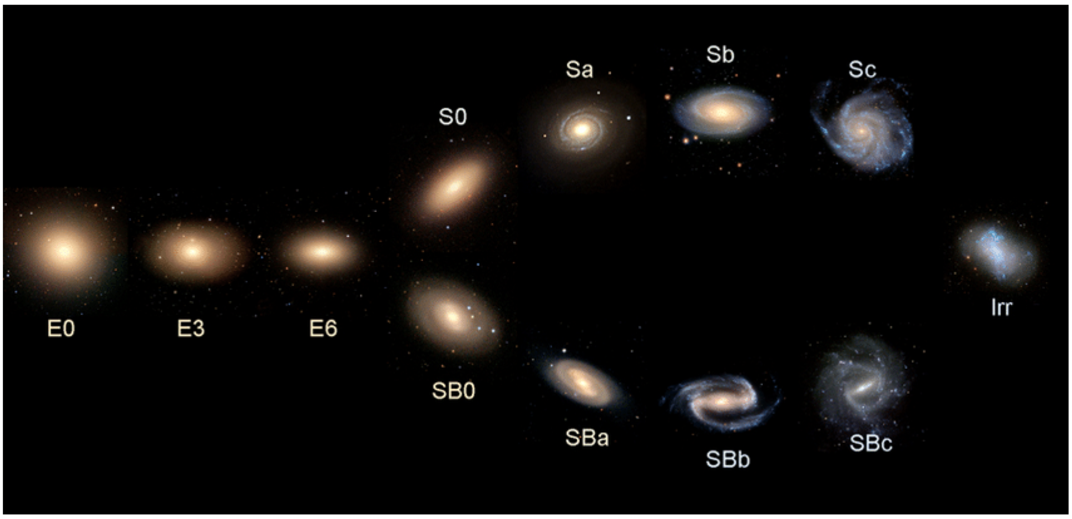

Figure 1.3: The Hubble tuning fork (Hubble 1926) with examples for elliptical, spiral and irregular galaxies. Elliptical galaxies are redder in colour due to the lack of recent star formation and an older stellar population, whereas spiral galaxies are bluer as they are actively star forming. From Cui et al. (2014).

found at $z < 2$) can be categorised according to the Hubble tuning fork (Figure 1.3, Hubble (1926)). Edwin Hubble created this system in the 1900s and it is still broadly consistent with modern observations of local galaxies.

The broad categories of galaxies are ellipticals (‘E’) and spiral galaxies, with spirals further forking into barred (‘SB’) and unbarred spirals (‘S’). Elliptical galaxies have spherical or ellipsoidal profiles and typically contain minimal dust and gas. This lack of gas means that they can no longer form stars, resulting in an older stellar population and a red colour. They are generally featureless, with no disk or spiral arms and they can be subcategorised from E0 to E6, with E0 referring to a more spherical bulge and an E6 being a more stretched and elliptical bulge.

Spiral galaxies contain a central bulge, spiral arms and a flat disk. As they do contain gas they are typically actively star forming and therefore bluer in colour than ellipticals. Further categorisation, as well as whether they have a bar (B) in them, is denoted with a lower case ‘a’, ‘b’ or ‘c’. An SBa galaxy is a barred spiral with a large central bulge and tightly wound arms, and a Sc galaxy is an unbarred spiral with a smaller bulge and less tightly wound arms.

Hubble also classified an irregular group containing galaxies with neither of the above structures. These could have no clear disk or bulge, asymmetric shapes or fragmented areas of star formation.

Current galaxies evolution models suggest that elliptical galaxies represent a later stage in galaxy evolution, having formed via the mergers of spiral galaxies (e.g. De Lucia et al. 2006; Toomre & Toomre 1972). Ellipticals are mostly found in galaxy clusters whereas spirals are more likely to be found in the field or in smaller groups (like the Milky Way and the local group). Elliptical galaxies dominate the higher end of the stellar mass distribution and tend to have stellar masses greater than 10^{11} $\mathrm{M}_{\odot}$, while spirals are more commonly found in less massive galaxies (e.g. Ferrero et al. 2021; Oh et al. 2020; Simard et al. 2011).

1.2.3 The Evolving Universe

A big question in extragalactic astrophysics is how galaxies evolved from small intensely star-forming morphologically irregular systems in the early universe (Section 1.2.1) to the organised spiral and elliptical systems that are locally prevalent (Section 1.2.2). For this we must study galaxies at intermediate redshifts, which is one of the goals of this work (Chapter 3). One of the most fundamental things to measure is the star formation history of the Universe.

The star formation history of the Universe is important for understanding galaxy evolution and its dependencies on galaxy properties and environment. Measuring this key property of the Universe robustly requires uniform selection of well-understood samples of star-forming galaxies across a range of redshifts, from the first galaxies to local galaxies. The star formation rate of a galaxy is a measure of the mass of stars it produces per year, measured in $M_{\odot}\,\mathrm{yr}^{-1}$. The cosmic star formation rate density (SFRD) is the measure of star formation within a comoving volume within a given redshift slice and hence a given slice of cosmic time, which is measured in $M_{\odot}\,\mathrm{yr}^{-1}\,\mathrm{Mpc}^{-3}$.

Figure 1.4 shows the estimate of the evolution of cosmic star formation history of the Universe with redshift from ultraviolet and infrared observations from Madau & Dickinson (2014). Results suggest that over the first $\sim$3 Gyr of the Universe's lifetime, the cosmic star formation rate increased rapidly, appearing to

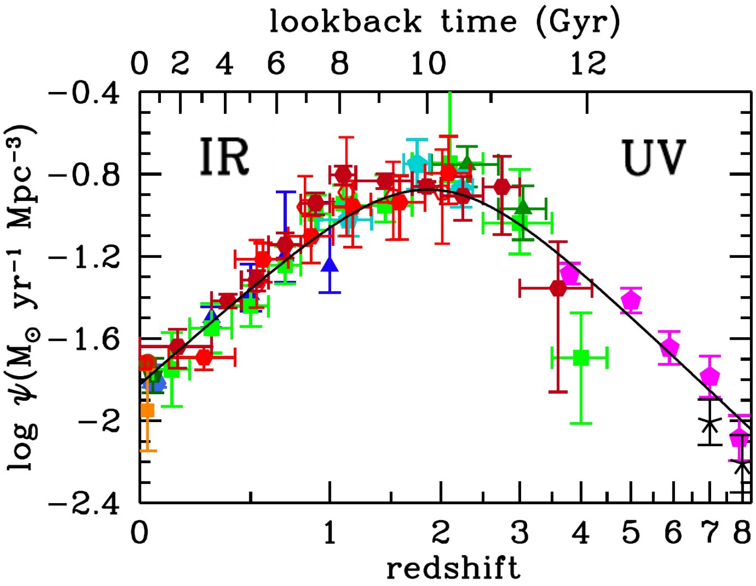

Figure 1.4: Cosmic star formation history of the Universe, estimated via UV (green and pink points) and IR (red points) from Madau & Dickinson (2014). These results tell us that star-formation rapidly increased with time in the early Universe, peaking at $z \sim 2 - 3$ and has been gradually decreasing until the present day.

peak at $z \sim 2$, before gradually decreasing to the present day (e.g. Bouwens et al. 2015; Hopkins & Beacom 2006; Karim et al. 2011; Khostovan et al. 2015, 2020; Lilly et al. 1996; Madau & Dickinson 2014; Sobral et al. 2013; Stroe & Sobral 2015). This epoch of time during the peak of star formation, at $z \sim 2$, is known as 'cosmic noon'. This trend appears consistent for galaxies of all observed masses (e.g. Karim et al. 2011; Sobral et al. 2013) and results suggest that approximately half of the stellar mass that we can observe today was formed before $z \sim 1$ (i.e. over ~8 Gyr ago), when the Universe was roughly a third of its current age (e.g. Ilbert et al. 2013; Madau & Dickinson 2014; Muzzin et al. 2013; Thorne et al. 2021; Weaver et al. 2022; Wright et al. 2018). The trend also holds independent of sample selection, including for Hα, [OIII] and [OII] emitters (Figure 1.6). However, the reasons for this epoch of significant star formation and the decline in more recent times is yet unknown, but pushing to understanding this pattern in the cosmic star formation history is fundamental to extragalactic astrophysics. A helpful way to study the star formation history of the Universe is to study star-forming, line-emitting galaxy samples through different redshifts and measure their star formation rates (Section 1.2.3, Chapter 3).

1.2.4 Identifying Star Forming Galaxies

One way to identify distant star-forming galaxies is via the rest-frame UV continuum, which is especially effective at high redshift (e.g. Bouwens et al. 2014, 2015, 2021; Bowler et al. 2017b; Bunker et al. 2010; Cucciati et al. 2012; Finkelstein et al. 2015; Reddy & Steidel 2009; Robertson et al. 2010; Wilkins et al. 2011). Efficient selection of UV-emitting star-forming galaxies at particular redshifts can be done via the Lyman break technique, which pinpoints the Lyman limit photometrically. For star-forming galaxies in the distant Universe, radiation at rest-frame wavelengths shortward of 912Å (the Lyman-limit) is absorbed by neutral gas along the line-of-sight. This causes galaxies to be undetected (or "drop-out") in filters bluer than rest-frame 912Å, which allows for the efficient selection of high-redshift targets if deep short wavelength data are available (e.g. Steidel et al. 1996). The observed wavelength of the Lyman break shifts with redshift by a factor of $(z + 1)$, meaning that at $z > 7$ the Lyman break is at $\lambda_{\rm obs} > 7296$Å. In Figure 1.5 the Lyman break is beyond the left of the plot. The Lyman break selection process uses broadband surveys which means that the derived photometric redshifts are often uncertain and only wide redshift bins can be studied. Similarly, the inconsistencies in sample selection methods at high redshift and lower redshifts mean that the trends seen between the samples can be interpreted incorrectly as evolutionary effects, whereas they are due to the differences in the selection processes (e.g. Stott et al. 2013). Furthermore, UV selected samples miss the dusty star-forming galaxies, leading to a biased sample.

Alternatively, selecting a galaxy based on its emission lines is a powerful way to identify samples of star-forming galaxies. Emission lines are a bright feature of a galaxy and they trace the instantaneous star formation from the short-lived O and B stars (which have lifetimes of $\sim 10^6$ years). This means that we can harness a significant amount of information about both individual galaxies and the star formation history of the Universe via this selection process. Significant rest-frame UV-optical emission lines that are useful for selecting star-forming galaxies are Lyα, Hα, [OIII] and [OII]. See Figure 1.5 (edited from Narayanan et al. (2021))

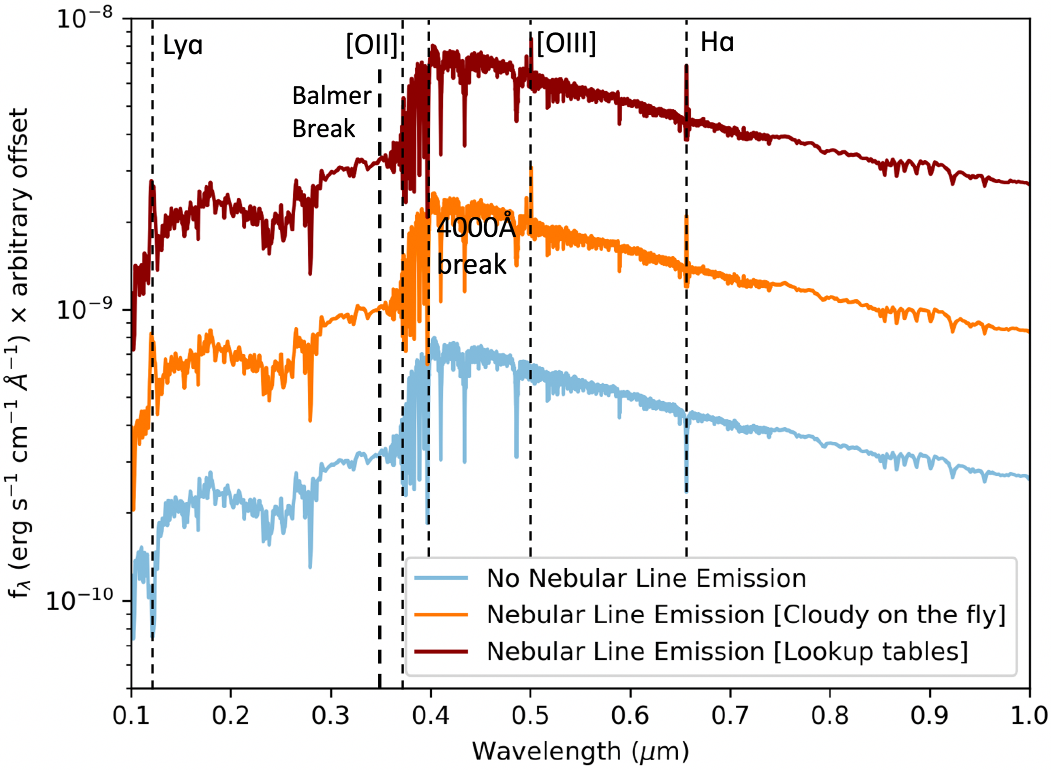

Figure 1.5: Spectrum showing the Lyα (1215.67Å), [OII] (3727Å, 3729Å), [OIII] (5007Å) and Hα (6563Å) emission lines, the Balmer break (3645Å) and the 4000Å break, edited from Narayanan et al. (2021). The Lyman break (912Å) is beyond the left of the range shown. These three spectra show star-forming galaxies, meaning that the break between the Balmer break and 4000Å break labels is more likely to be due to the Balmer break, as the 4000Å break is not observed in star-forming galaxies. “The different coloured lines show the impact of nebular line emission on UV-optical SED of a star-forming galaxy (from the GIZMODISK model). The blue line shows the default model with no nebular line emission; the orange line includes nebular lines for a model in which the spectrum from photoionization regions around young stars are calculated with on the fly CLOUDY models, while the maroon line shows the same, but with the nebular line emission computed via the Byler et al. (2017) lookup tables. The flux densities are offset by an arbitrary multiplicative factor to aid in clarity.” - Narayanan et al. 2021.

for a visualisation of these lines, the Balmer break and the 4000Å break. The maroon line shows a simulated spectrum containing nebular emission lines, which are labelled along with the 4000Å break.

Hydrogen is the most abundant element in the Universe, making up $\sim 75\%$ of the baryonic mass (Planck Collaboration et al. 2020). The Lyα emission line (Lyα; rest-frame 1215.67Å) is a result of electron cascades in the hydrogen atom, from energy level $n = 2$ to $n = 1$. It is the intrinsically brightest emission line in the UV-optical range, making it ideal for studying the high-redshift Universe. In young star-forming galaxies the interstellar medium (ISM) is primarily composed of hydrogen, which surrounds the young stars and reprocesses the emitted photons, making the Lyα line a good tracer of these objects (Partridge & Peebles 1967). The Lyα line is ideal for studying the epoch of reionisation (Section 1.3) as it is scattered by neutral hydrogen. Studies of the Lyα luminosity function show minimal evolution from $z \sim 2-6$ (e.g. Ouchi et al. 2008; Santos et al. 2016; Sobral et al. 2018) but at $z > 6$ the effects of reionisation can be observed in the Lyα luminosity function and it evolves drastically (Section 1.3).

Like Lyα, the Hα emission line is created from the abundant hydrogen in the Universe. Hα is emitted from the transition between energy levels $n = 3$ and $n = 2$, giving a rest-frame wavelength of 6563Å. Samples using Hα line selection are typically highly complete and contain both dusty and dust-free galaxies (e.g. Coughlin et al. 2018; Fujita et al. 2003; Gallego et al. 1995; Hayashi et al. 2018; Hippelein et al. 2003; Ly et al. 2007; Morioka et al. 2008; Shioya et al. 2008; Tadaki et al. 2011; Tresse & Maddox 1998). This is because the Hα line is at a long enough wavelength to be less affected by dust; the Hα wavelength and the size of dust particles are comparable. However, Hα is only observable with ground-based facilities out to $z \sim 2$: at higher redshifts it is shifted into the mid-IR region and blocked by atmospheric water vapour and carbon dioxide. The Hα line is an ideal tracer of star formation and has been well-calibrated for dust attenuation (e.g. Kennicutt 1998). Figure 1.6 (right) shows the SFRD (Section 1.2.3) up to $z \sim 2$ from Sobral et al. (2013), and it shows that Hα follows the pattern of decreasing star formation from $z \sim 2$ to $z \sim 0$. The Hα luminosity function has been well-observed in its observable range (e.g. Gómez-Guijarro et al. 2016; Harish et al. 2020; Khostovan et al. 2020; Ly et al. 2007,

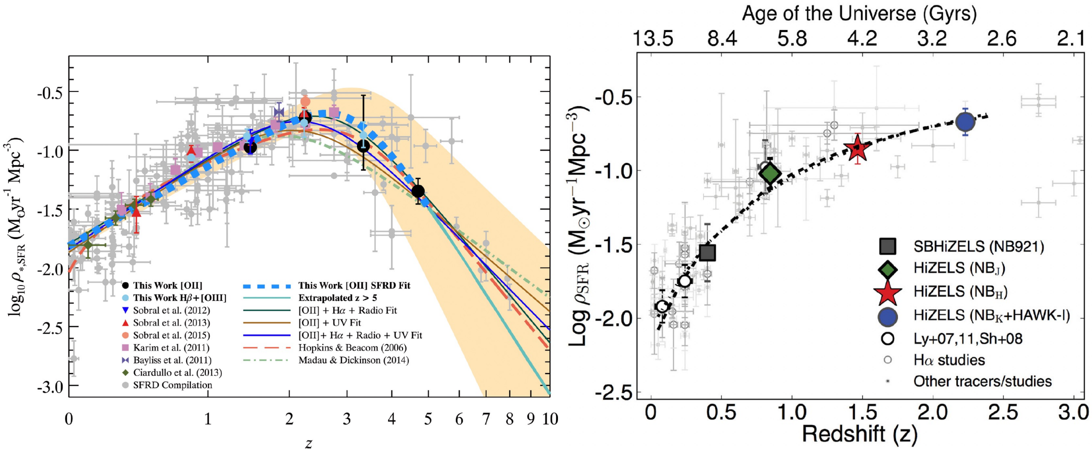

Figure 1.6: Cosmic star formation history of the Universe, estimated via [OIII] and [OII] (left, from Khostovan et al. (2015)) and Hα (right, from Sobral et al. (2013)). The [OIII] and [OII] results (left) show that star-formation rapidly increased with time in the early Universe, peaking at $z \sim 3$ then gradually decreasing until the present day. This is consistent with the measurements presented in Figure 1.4 (the green dash-dotted line on plot on the left is from Madau & Dickinson (2014)). As Hα (right) is only observable up to $z \sim 2$ with ground-based observations, we can only see the decrease in SFRD from $z \sim 2$ to $z \sim 0$ with current observations of this tracer.

2011; Ramón-Pérez et al. 2019; Sobral et al. 2013, 2015a) and studies find that the luminosity function evolves significantly with redshift. This is consistent with the observed rise in SFRD as redshift increases.

The [OIII] line is a doublet line emitted from doubly ionised oxygen, with its primary line at 5007Å and secondary line at 4959Å. It is a forbidden line which means that it is too rare to observe in laboratory conditions on Earth but the large volume of gas around the stars means that it is observed here. Many studies have selected samples via the [OIII] line (e.g. Hayashi et al. 2018; Hippelein et al. 2003; Khostovan et al. 2015, 2020; Ly et al. 2007; Matthee et al. 2017a; Sobral et al. 2015a) however [OIII] samples are easily contaminated with Hβ and by active galactic nuclei (AGN) (e.g. Drake et al. 2013; Ly et al. 2007). Surveys of the [OIII] line (e.g Hayashi et al. 2020; Khostovan et al. 2015, 2020; Nagaraj et al. 2023; Sobral et al. 2015a) are complicated by the line being a doublet and that the Hβ line (rest-frame wavelength = 4862Å) is nearby and can contaminate the sample. This makes the [OIII] line less reliable when studying the star formation rate (e.g. Sobral et al. 2015a) but as Figure 1.6 shows, the [OIII] samples (right) still trace the expected shape of the star formation history of the Universe (e.g. Khostovan et al. 2015).

The [OII] line, (3727Å, 3729Å) is also a forbidden doublet line, emitted by singly ionised oxygen. There have been many successful studies of the [OII] line (e.g. Bayliss et al. 2011, 2012; Cedrés et al. 2021; Comparat et al. 2015; Khostovan et al. 2015, 2020; Ly et al. 2007; Matthee et al. 2017a; Sobral et al. 2012, 2015a; Takahashi et al. 2007) but there remains uncertainty about the ionisation state and metal abundance of [OII] emitters, which impacts the conversion between [OII] luminosity and star-formation rate (see Section 3.4 for more information). Surveys of the [OII] line (e.g. Bayliss et al. 2011; Hayashi et al. 2020; Khostovan et al. 2015, 2020; Sobral et al. 2012, 2015a) find strong evolution of the luminosity function with redshift and find [OII] samples to be ideal star formation rate tracers. Dust attenuation is less well-calibrated for [OII] than for Hα, but work from Hayashi et al. (2013) and Sobral et al. (2015a) confirm a good method to account for dust in [OII] emitters.

Note that these four emission lines (Lyα, Hα, [OIII] and [OII]) can also be energised by the hot, ionising radiation emitted by AGN, rather than by the hot

Figure 1.7: Visualisation of patchy reionisation where bright sources have created ionised bubbles around themselves and they are merging with bubbles of other bright sources. From ESO/L. Calçada.

O and B stars. Thus, AGN contaminants must be removed when measuring the star formation rate density of a sample, as they are not produced by star-forming sources and would therefore lead to an overestimate in the SFRD. Removal of these sources can include matching to catalogues of known AGN to remove any contamination or by removing AGN based on their redder spectral energy distributions.

1.3 The Epoch of Reionisation

The epoch of reionisation is an important era for the formation and evolution of galaxies as it marks the second, and last, major phase transition of hydrogen (the first being recombination, Section 1.1.2). Reionisation is thought to have started with the formation of the first stars and galaxies, which likely occurred between $z \sim 40$ and $z \sim 15$ (e.g. Barkana & Loeb 2001; Bromm & Yoshida 2011). The first galaxies resided in an intergalactic medium (IGM) of neutral hydrogen. Current results support the model of patchy reionisation (Figure 1.7), which suggests that the process of cosmic reionisation was inhomogeneous and started with the most

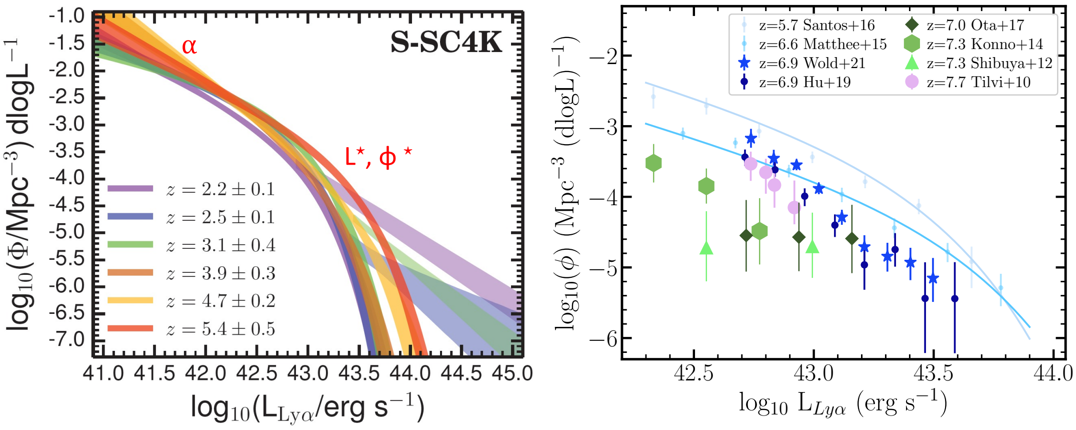

Figure 1.8: *Left:* The Lyα luminosity function, showing number density against luminosity, for samples of Lyα emitters in different redshift bins from $z \sim 2$ to $z \sim 6$. There is minimal evolution in the luminosity function in this redshift range. Labels show the faint-end slope (α) and the knee (L*, $\phi^\star$) of the Schechter function for the red $z = 5.4$ redshift bin. (Adapted from Sobral et al. (2018).) *Right:* The Lyα luminosity function at $z > 6$ from (Hu et al. 2019; Konno et al. 2014; Matthee et al. 2015; Ota et al. 2017; Santos et al. 2016; Shibuya et al. 2012; Tilvi et al. 2010; Wold et al. 2021). Above $z \sim 7$ the luminosity function is poorly constrained because the neutral hydrogen absorbs and scatters the Lyα photons.

massive sources and the most overdense regions (e.g. Dayal & Ferrara 2018; Mason & Gronke 2020; Matthee et al. 2015; Santos et al. 2016). With time, these sources produced enough ionising radiation (high-energy photons) to carve out ionised ‘bubbles’ around themselves, which then continued to grow and overlap until the IGM was fully ionised at $z \sim 6$ (e.g. Barkana & Loeb 2001; Barkana & Loeb 2004; Cen & Haiman 2000; Fan et al. 2006; Matthee et al. 2015; Tilvi et al. 2020; Wold et al. 2021). Alternatively, the Planck Collaboration et al. (2020) assumes an instantaneous reionisation and finds that the epoch of reionisation ends at $z = 7.82 \pm 0.71$. The epoch of reionisation is still a period of the Universe’s history that is not fully understood, but the community’s understanding is developing as technology improves and observations can probe to higher redshifts.

The Lyα emission line (Section 1.2.4) is a powerful tool with which to study the epoch of reionisation (e.g. Konno et al. 2017; Matthee et al. 2014) because its transmission is resonantly scattered by neutral, but not ionised, hydrogen. Lyα is also the strongest rest-frame UV and optical emission line in AGN and quasars, making it useful for pinpointing both star-formation and black-hole powered sources at high redshifts (Partridge & Peebles 1967; Pritchet 1994). At $z \sim 2 - 8$ Lyα emission shifts into the optical/near-IR regime, making it one of the few bright lines accessible for ground-based observations at $z \gtrsim 5$, hence its use for studying the high-redshift Universe. In the search for galaxies inside the epoch of reionisation, narrowband surveys have been successful in detecting the bright Lyα line in surveys for Lyα emitters (LAEs) at $z \sim 2 - 7$ (e.g. Hibon et al. 2010; Hu et al. 2010, 2019; Krug et al. 2012; Malhotra & Rhoads 2004; Ouchi et al. 2010; Santos et al. 2016, 2020; Sobral et al. 2018; Tilvi et al. 2010). Narrowband surveys target emission lines at specific redshifts (Section 1.4.1) and luminosity functions quantify the evolution of samples of galaxies and therefore reionisation (Section 1.4.4).

There is minimal evolution in the Lyα luminosity function from $z \sim 3$ to $z \sim 6$ (e.g. Figure 1.8, Ouchi et al. 2008; Santos et al. 2016; Sobral et al. 2018), but at higher redshifts the luminosity function declines, indicating that reionisation is incomplete and that there is an increasing fraction of neutral hydrogen in the intergalactic medium at $z \gtrsim 6$ (e.g. Konno et al. 2014). This interpretation is consistent with results from follow-up of UV selected sources (e.g. Tilvi et al. 2014).

Between $z \sim 6$ and $z \sim 6.6$ the Lyα luminosity function behaves differently at the bright-end compared with the faint-end. The density of bright LAEs does not evolve over this redshift range, but there is a strong decline in the density of faint LAEs (e.g. Figure 1.8, Matthee et al. 2015). Indeed, at $z = 6.6$ bright LAEs are $\sim 30\times$ more common than expected based on the evolution of the faint sources. The observation of evolution in only the faint-end but not the bright-end of the Lyα luminosity function at $z \sim 6$ – 6.6 suggests that reionisation is patchy and completed around the most luminous sources first, resulting in their Lyα emission being observable when Lyα from fainter sources is not (e.g. Matthee et al. 2015; Tilvi et al. 2020). To further study this, Matthee et al. (2015) used toy models to show that faint sources at $z = 6.6$ can only be observed if they are inside the ionised bubble of a brighter source, suggesting that this is likely due to patchy reionisation.

The LAGER survey (Hu et al. 2010; Wold et al. 2021) observed the widest area to-date at $z = 6.9$ (volume of 6.1×10^6 Mpc^3), and shows further evolution in the Lyα luminosity function (Figure 1.8). The model of patchy reionisation is further supported by the $z = 6.9$ results from (Wold et al. 2021), which found significant cosmic variance between observed fields, with more ionised regions containing more LAEs than less ionised fields. However at $z = 6.9$ the survey depths limit measurements of the faint-end of the luminosity function and the survey area is insufficient to constrain the bright-end well.

At $z > 7$ surveys are more limited, with the bright and faint ends of the Lyα luminosity function being probed separately by surveys that are wide and shallow or deep and small (e.g. Figure 1.8, Konno et al. 2014; Ota et al. 2017; Shibuya et al. 2012; Tilvi et al. 2010). In Tilvi et al. (2010) they find four $z = 7.7$ Lyα emitters using an ultra-narrowband (9Å) on the NEWFIRM camera at the KPNO 4m Mayall telescope, in a comoving volume of 1.4×10^4 Mpc^3. They point out that their survey does not overcome cosmic variance and getting statistics from more fields at these high redshifts is important, especially as the field-to-field variation for brighter sources is more prominent. Therefore, the specifics of the $z > 7$ Lyα luminosity function are poorly understood and wide and deep surveys that simultaneously probe a range of luminosities and overcome cosmic variance are required. Above $z = 7$ there is potential evolution in the faint-end when compared with $z = 5.7$ and $z = 6.6$ results (Figure 1.8). These Lyα results from $z = 5.7$ to $z = 7.7$ are summarised in Table 1.1.

A useful value to constrain in order to understand how the process of reionisation developed is the neutral fraction of hydrogen (χ_{HI}). This is a measure of the average volume filling fraction of neutral gas in a given region at a given redshift (e.g. Madau et al. 1999; Robertson 2022). Since Lyα interacts with neutral hydrogen, surveys that combine observations of LAEs with the UV continuum can be used to probe reionisation and measure the neutral fraction of hydrogen at specific epochs (e.g. Bouwens et al. 2015; Finkelstein et al. 2015; Hu et al. 2019; Jones et al. 2023; Konno et al. 2014; Mason et al. 2018; Ota et al. 2010, 2017). Studies using Lyα emitters to study the neutral fraction of hydrogen find that it decreases from $\chi_{\mathrm{HI}} \geq 0.5$ at $z \sim 7$ (Konno et al. 2014; Pentericci et al. 2014) to $\chi_{\mathrm{HI}} \sim 0.0$ at $z \sim 6$, as reionisation is complete at $z \sim 6$. Measurements

Table 1.1: Summary of the previous Lyα surveys from $z = 5.7 - 7.7$.

Reference	NB Filter (Instrument)	NB Wavelength (Å)	Lyα Redshift	Area deg^2
Santos et al. (2016)	NB816 (Suprime-Cam/Subaru)	8150	5.7	7.0
Matthee et al. (2015)	NB921 (Suprime-Cam/Subaru)	9196	6.6	4.66
Hu et al. (2019)	NB964 (DECam/CTIO)	9642	6.9	2.14
Wold et al. (2021)	NB964 (DECam/CTIO)	9642	6.9	6.15
Ota et al. (2017)	NB973 (Suprime-Cam/Subaru)	9755	7.0	0.47
Konno et al. (2014)	NB101 (DECam/CTIO)	10095	7.3	0.22
Shibuya et al. (2012)	NB1006 (Suprime-Cam/Subaru)	10052	7.3	0.48
Tilvi et al. (2010)	UNB (NEWFIRM/KPNO)	10063	7.7	0.22

at $z \geq 7$, which would probe earlier phases of reionisation, are currently limited, with Konno et al. (2014) determining $\chi_{\mathrm{HI}} = 0.3 - 0.8$ at $z = 7.3$, which Hu et al. (2019) constrained further to obtain $\chi_{\mathrm{HI}} = 0.2 - 0.4$ at this redshift.

In summary, the $z > 7$ Lyα luminosity function is as-yet poorly constrained, but wide and deep narrowband surveys could help to fill the dearth of information by finding sources here, which could then be spectroscopically confirmed, and providing additional measurements of χ_{HI} earlier in the history of the Universe. This would help us to further constrain the process of cosmic reionisation.

1.4 Observational Tools

Observational astrophysicists have access to many different facilities and telescopes by which we can obtain the necessary data for our investigations. Here, we discuss some necessary observational tools to study line-emitting, star-forming galaxies.

1.4.1 Narrowband Surveys

The method used to find star-forming galaxies in this study is narrowband surveys. A narrowband filter is one that only allows a narrow range of wavelengths through it, typically with widths ∼100Å. If a galaxy has a bright emission line at the wavelength of the filter then it will appear brighter in the narrowband than the broadband. Since emission lines are redshifted (Section 1.4.2) then this narrow width constrains the redshift range of the galaxy and the slice of cosmic time that is observed.

In order to be selected as an emission line galaxy from a narrowband image, we need to compare the magnitudes in the narrowband to the magnitudes in a nearby or adjacent broadband image, which covers the continuum. Essentially, if a source is significantly brighter in the narrowband than the nearby broadband, it is likely a line emitter. Figure 1.9 illustrates this; in the circled region there are two bright sources in the narrowband image (top), but in the broadband image (middle) they are not visible. When the broadband is subtracted from the narrowband (bottom) these sources remain, but the other galaxies do not. Thus these are narrowband excess sources, and are likely line emitters.

Narrowband surveys are relatively cheap ways to collect a complete and clean sample of emission line-selected galaxies as full spectroscopy is not required in order to obtain precise redshifts of all star forming galaxies at the target epoch. An added advantage is that it is also not necessary to have accurate photometric redshifts, as there are ways to identify a source as a specific line emitter based on colour-colour selection, (Sections 3.2.3 and 4.2.2, e.g. Daddi et al. 2004; Khostovan et al. 2015, 2020; Matthee et al. 2017a; Sobral et al. 2013, 2015a; Stroe & Sobral 2015) and therefore narrow down the source's redshift to be within the narrowband's coverage. This is because the spectral energy distribution of a source at a specific redshift will have features such as the Lyman break or Balmer break falling between specific broadband filters. The Lyman break, as discussed in Section 1.2.4, is caused by rest-frame wavelengths shorter than 912Å being absorbed by neutral gas surrounding the galaxy, creating no detectable emission below this rest-frame wavelength. The Lyman break is off the left side of Figure 1.5. The Balmer break has a rest-frame wavelength of 3645Å and is caused by hydrogen

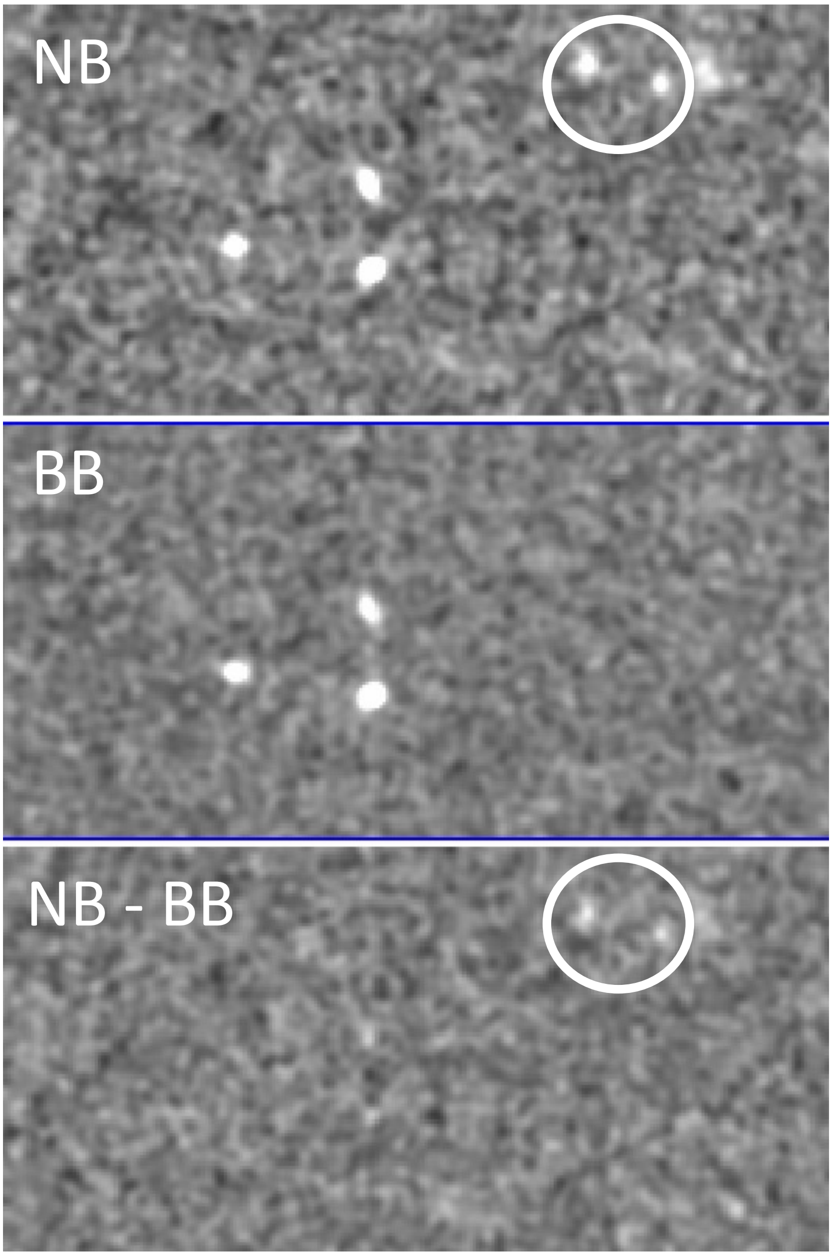

Figure 1.9: Visualisation of the narrowband technique with a narrowband image on top, a broadband image in the centre and the narrowband minus the broadband image at the bottom. The two circled sources are narrowband excess sources (line emitters) as they are visible in the narrowband image but they are not visible in the narrowband minus broadband image. We can see that the three bright sources also in the image are visible in both the narrowband and broadband images so they are not visible in the narrowband minus broadband image, meaning they are not narrowband excess sources.

atoms with electrons in the $n = 2$ energy level being ionised by photons with wavelengths shorter than 3645Å. This results in the blanket absorption of these photons and thus lower continuum emission below 3645Å. The Balmer break is shown on Figure 1.5 to the left of the [OII] line and the 4000Å break. These breaks cause a large difference in magnitude between the broadbands straddling the break. For example, for a Lyα emitter at $z = 7.7$, the Lyman break is in the Y-band, so the z-band has no/minimal detection of the source, but the J-band will cover the rest-frame UV continuum, causing the $z - J$ colour to be particularly red.

A balance of wide and deep surveys are required to fully sample the Universe. Deep surveys enable more faint objects to be observed and wide areas are more likely to find the rare bright objects. These rare, extreme galaxies are often extremely active, with lots of star formation and high equivalent widths. Studying these sources is important to further our understanding of the physics behind how emission lines are produced in galaxies (e.g. Lumbreras-Calle et al. 2022; van der Wel et al. 2011).

Narrowband surveys therefore offer a different glance into the Universe than UV surveys do (Section 1.2.4), selecting galaxies based on a specific emission line and providing clean, complete samples.

1.4.2 Measuring Redshift

Redshift (z) is useful for describing astrophysical distances and is given by:

$$z = \frac{\lambda_o - \lambda_\epsilon}{\lambda_\epsilon} \tag{1.1}$$

where λ_o is the observed-frame wavelength of a spectroscopic feature and λ_ϵ is the rest-frame wavelength of that feature. For sources with a narrowband excess or emission line in the narrowband filter, λ_o corresponds to the wavelength of the narrowband filter and if we know the emission line that has been observed (emitted wavelength) then we can find the redshift of that source. Only certain bright emission lines, such as Lyα, Hα, [OIII] and [OII] (Section 1.2.4) can cause a significant narrowband excess. Selecting a source via its narrowband excess therefore constrains its redshift to a limited range of values.

Redshifts can be found using either spectroscopic data or photometric data. Spectroscopic redshifts are more accurate but costly in terms of telescope time and photometric redshifts are less accurate (especially as redshift increases, unless there is a strong feature, such as a Lyman break) but they are cheaper in terms of telescope time.

To calculate a spectroscopic redshift, one must obtain a spectrum of the source, identify its emission (or absorption) features and match the wavelengths to the expected features to find the redshift. Ideally, the spectrum would include two or more lines, though an asymmetric line (like Lyα) or a doublet line can help to narrow down what lines they could be, and hence improve the estimate of the redshift (e.g. Hasinger et al. 2018). Although spectroscopic redshifts are more accurate and reliable, they are usually biased towards bright sources that are selected for follow-up due to their brighter continua and detectability.

Photometric redshifts are derived by fitting photometric data from broad, medium and narrowbands to synthetic SED templates at different redshifts. There are a number of SED fitting codes including EAZY (Brammer et al. 2008), HYPERZ (Bolzonella et al. 2000) and LePhare (Arnouts et al. 2002; Ilbert et al. 2006). This method works best when there are good quality data in as many bands as possible and when features like an emission line, the Lyman break (912Å), the Balmer break (3645Å) or the 4000Å break are observed.

1.4.3 From Night Sky to Astrophysical Values

This section explores the mathematics needed to derive the emission line luminosities from the observed magnitudes. Throughout this thesis we use the AB magnitude system wherein $1\,\mu\mathrm{Jy} = 23.9\,m_{\mathrm{AB}}$ (Oke & Gunn 1983). In Chapter 2, we measure the magnitudes of the target sources in the narrowband and a nearby broadband and from this we can quantify the key properties of the line emitters.

One of the key quantities for line emitting galaxies is the *line flux*, which is the amount of flux from just the emission line of a source, with no continuum counted. The narrowband filter will include flux from the emission line and the continuum, and the broadband will contain flux just from the continuum, and the goal here is to find the flux just from the emission line. Using the AB magnitude system, we can relate the magnitude ($\mathrm{m_{NB}}$ and $\mathrm{m_{BB}}$ for narrowband and broadband magnitude respectively) to flux density (f_ν) using:

$$f_{\nu_{\mathrm{NB}}} = 10^{-0.4(m_{\mathrm{NB}}-48.60)} \tag{1.2}$$

$$f_{\nu_{\mathrm{BB}}} = 10^{-0.4(m_{\mathrm{BB}}-48.60)} \tag{1.3}$$

with f_ν in $\mathrm{erg\,s^{-1}\,cm^{-2}\,Hz^{-1}}$. We can then calculate f_λ using:

$$f_{\lambda_{\mathrm{NB}}} = \frac{c}{\lambda^2_{\mathrm{NB}}} \times f_\nu = \frac{c}{\lambda^2_{\mathrm{NB}}} \times 10^{-0.4(m_{\mathrm{NB}}+48.60)} \tag{1.4}$$

$$f_{\lambda_{\mathrm{BB}}} = \frac{c}{\lambda^2_{\mathrm{BB}}} \times f_\nu = \frac{c}{\lambda^2_{\mathrm{BB}}} \times 10^{-0.4(m_{\mathrm{BB}}+48.60)} \tag{1.5}$$

where f_λ (for the narrowband and broadband respectively) is in $\mathrm{erg\,s^{-1}\,cm^{-2}\,\mathring{A}^{-1}}$, c is the speed of light in $\mathrm{\mathring{A}\,s^{-1}}$ and λ_{NB} (λ_{BB}) is the central wavelength of the narrowband (broadband) filter in Å. Since $f_{\lambda_{\mathrm{NB}}}$ contains both line and continuum emission and $f_{\lambda_{\mathrm{BB}}}$ contains only continuum emission, to get the flux density of the line only, we subtract the flux density in the broadband from the flux density in the narrowband:

$$f_{\lambda,\mathrm{line}} = f_{\lambda,\mathrm{NB(continuum+line)}} - f_{\lambda,\mathrm{BB(continuum)}} \tag{1.6}$$

In order to obtain the emission line flux (f_{line} from the flux density, we integrate over the full narrowband width ($\Delta\lambda_{\mathrm{NB}}$):

$$f_{\mathrm{line}} = \Delta\lambda_{\mathrm{NB}} \times f_{\lambda,\mathrm{line}} \tag{1.7}$$

From the line flux we can calculate the line luminosity, but for this we first need the redshift of the object (Section 1.4.2). From redshift we can calculate the luminosity distance (d_L), which is the distance that the light has travelled to the observer when accounting for the expansion of the Universe. Here, we use ASTROPY (Astropy Collaboration et al. 2013, 2018, 2022) to calculate the luminosity distance for our given cosmological parameters (Section 1.1.1). Once we have the luminosity distance we can calculate the luminosity of the source:

$$L = 4\pi f_{\mathrm{line}} d_L^2 \tag{1.8}$$

Luminosity is a measure of intrinsic brightness of a galaxy, and since we calculate it using the line flux (f_{line}) of a source, we are calculating the luminosity for a specific emission line. If we collect many sources with the same emission line and calculate their luminosities, we can study their statistical properties with a luminosity function.

1.4.4 Luminosity Functions

Galaxies have a wide range of luminosities, and a good way to visualise this is with a luminosity function which tell us the prevalence of sources of different brightness (which can correlate with stellar mass and star formation rate). Luminosity functions are useful measurements for tracking the evolution with luminosity when comparing galaxy samples at different redshifts.

For example, the slope of the number counts at the faint and bright ends is due to different feedback mechanisms that dominate at different masses. Faint galaxies reside in low-mass dark matter haloes, which have smaller potential wells than more massive haloes. This means that when stars explode in a supernovae, the winds can be strong enough to overcome the potential and drive out the gas from the galaxy, which quenches star formation. At the bright end, the potential is large enough for this effect to be minimal, but instead AGN feedback quenches star formation. This process involves matter falling into the supermassive black hole, causing the release of a lot of radiation, heating the gas that is in close proximity (e.g. Somerville et al. 2008). This quenching is observed as the exponential cut off in the Schechter function (see Section 1.4.4). The sweet spot between these two effects, where neither are very strong, is at the knee of the function (where $L^\star$ and $\phi^\star$ are) and this is where the maximum efficiency of star formation is found (Behroozi et al. 2013; Finkelstein et al. 2015). Simulations have demonstrated the impact of, and requirements for, feedback by comparing mock luminosity functions and stellar mass functions with observations when different types of feedback are turned on or off (e.g. Bower et al. 2006; Springel & Hernquist 2003).

All sources within a luminosity function must be selected in a consistent way, i.e. Hα emitters, Lyα emitters or UV-continuum selected sources. Figure 1.8 shows an example of a Lyα luminosity function, with samples of Lyα emitters (LAEs) from $z \sim 2$ to $z \sim 6$, showing minimal evolution. The shape of a luminosity function is typically parametrised by the Schechter function (Schechter 1976):

$$\phi(L)\mathrm{d}L = \phi^{\star} \ln 10 \left(\frac{L}{L^{\star}}\right)^{1+\alpha} e^{-(L/L^{\star})} \mathrm{d}\log_{10} L \tag{1.9}$$

where ϕ is the number density, L is the luminosity, $\phi^{\star}$ and $L^{\star}$ are the characteristic number density and luminosity respectively and α is the faint-end slope. The characteristic number density and luminosity are the values at the 'knee' of the Schechter function, shown on Figure 1.8, and α is the slope for galaxies below the knee.

Due to the nature of the Schechter function parameters, they are correlated to one another; a shift in $L^{\star}$ will cause a shift in $\phi^{\star}$ and α, and so forth (e.g. Figure 3.9, Khostovan et al. 2015, 2020; Sobral et al. 2013). This means that when measuring luminosity functions, it is vital to simultaneously cover a wide range of luminosities with good number statistics in order to get reliable Schechter parameters.

As discussed in Section 1.4, surveys that are wide *and* deep are ideal. On a luminosity function this translates to us being able to probe both the faint-end (deep) and the bright-end (wide) in order to fully constrain both. There are added benefits of wide area surveys, especially ones that cover multiple fields, in that they help to improve sample variance and to overcome cosmic variance. All observations are affected by large-scale structure of the Universe, and this means that observations of one field could be statistically different to observations of a different field, due to different large-scale densities between the fields, bringing about significant uncertainty (e.g. Moster et al. 2011). Observing wide area and multiple fields helps to gauge the correct number counts of galaxy samples. The study of high-redshift galaxies requires identifying intrinsically-luminous sources, which are rare. Therefore, wide-area surveys are required (e.g. UltraVISTA/COSMOS and UDS) and these have revealed that the number density of luminous sources is likely higher than previously expected (e.g. Bowler et al. 2014; Matthee et al. 2015). Particularly when it comes to understanding the process of reionisation there is a need to study the full luminosity range of galaxies at $z > 7$, in order to understand which sources contribute most to the ionising of hydrogen. As discussed in Section 1.3, it is thought that the rarer but brighter sources dominate reionisation, but it is unclear how the faint sources contribute to reionisation.

An alternative to fitting a Schechter function to a luminosity function is to fit a double power law (DPL). This can be described as a gradient of α at the faint-end (like the Schechter function) and a power-law exponent of β for the brighter sources, as well as $\phi^\star$ and $L^\star$, which define the density scaling and the point where dominance shifts from one power law to the other, respectively. This is used because for some results, especially for UV-selected galaxies at $z > 7$, the bright-end does not fall off as steeply as the Schechter function describes, so this DPL is a more accurate fit (e.g. Bowler et al. 2012, 2014, 2017b). These results suggest that less mass quenching is occurring at higher redshift than at lower redshift (Bouwens et al. 2015).

Constraining the luminosity functions and statistical properties of galaxies is not only important for our understanding of the history of the Universe and the process of galaxy evolution, but also to guide observing strategies and planning for future, wide-field surveys and telescopes, such as *Euclid*, the Legacy Survey of Space and Time (LSST) and *Nancy Grace Roman Space Telescope.* These facilities require accurate number counts of galaxies across all luminosities and redshifts in order to plan their missions and goals and to achieve the best possible science outcomes.

1.5 This Thesis

The ideal survey to study the evolution of star-forming galaxies via line emitters would be both deep enough to accurately measure the faint-end turn off and wide enough to pick up all the of the bright but rare sources and overcome cosmic variance. Observations in many narrowbands and broadbands, with matched astrometry, would allow for the tracking of the luminosity function of line emitters at different redshifts.

This thesis is focused around the Y-NBS survey – an original narrowband survey undertaken with HAWK-I on the VLT, observing the COSMOS field. We use Y-NBS to identify and study the Hα, [OIII], [OII] and Lyα line emitters at $z = 0.62$, $z = 1.12$, $z = 1.85$ and $z = 7.7$, respectively. The key questions addressed in this thesis are as follows:

1. What are the statistical properties of low redshift line emitters? (Chapter 3)
2. What can these sources tell us about the cosmic star formation history of the Universe? (Chapter 3)
3. Can we find Lyα emitters at $z = 7.7$ within our pilot survey? (Chapter 4)
4. What are the implications for reionisation and the high redshift Universe from this study? (Chapter 4)
5. What can we determine about the size of reionisation bubbles and the neutral fraction of hydrogen at $z = 7.7$? (Chapter 4)

Our conclusions are summarised in Chapter 5, which also discusses possible future work and remaining open questions.

Chapter 2

Introducing Y-NBS: Observations, Data Reduction and Catalogue Creation

Abstract

Narrowband surveys provide an efficient way to select a clean and complete sample of line emitting galaxies. This chapter introduces the Y-NBS survey, which was carried out using VLT/HAWK-I with the NB1060 filter. The data are fully reduced with a bespoke pipeline written in PYTHON, which is presented here. We introduce the ancillary data used to complement Y-NBS, give details about how sources were extracted and select line emitting galaxies from these catalogues. The identified line emitters are then analysed in Chapters 3 and 4.

2.1 Introduction

This chapter introduces the crux of this thesis: the Y-NBS survey, which is a narrowband study using the NB1060 filter on the High Acuity Wide field *K*-band Imager (HAWK-I, Casali et al. 2006; Kissler-Patig et al. 2008; Pirard et al. 2004; Siebenmorgen et al. 2011), which is an instrument on the Very Large Telescope (VLT). We have obtained new observations in COSMOS, which we analyse in conjunction with additional archive data for GOODS-S. As a wide and deep narrowband survey, Y-NBS has the primary science goal of searching for $z = 7.7$ Lyman-α emitters in order to probe the epoch of reionisation, which is presented in Chapter 4. Y-NBS is also an excellent survey to study Hα, [O III] and [O II] emitters at lower redshifts, which is undertaken in Chapter 3. The wide area ($\sim$ 0.8 deg^2) of the COSMOS data combined with the significant depth ($3\sigma = 25.7$ mag) of the GOODS-S data means that both the bright and faint ends of the luminosity functions can be studied in a self-similar way.

COSMOS and GOODS-S are chosen for this study because of the wealth of ancillary data available. The COSMOS field is one of the most well-observed fields in the night sky and the Cosmic Evolution Survey (COSMOS) ‘has become a cornerstone of extragalactic astronomy’ (Weaver et al. 2022). COSMOS was initially a *Hubble Space Telescope* (*HST*) survey with the aims of studying galaxy evolution across small and large scales through low and high redshifts [1]. It took *HST* 640 orbits to observe the full COSMOS field, making it the largest ever *HST* survey. COSMOS is an equatorial field covering around 2 deg^2 (which equates to 16 full moons on the sky). The location of COSMOS observations was chosen as there are few bright foreground stars and there is minimal foreground gas and dust from the Milky Way along the line of sight, which could complicate analyses of distant galaxies. Telescopes in every wavelength range from X-ray to radio and both space- and ground-based observatories have since observed COSMOS, providing a plethora of supplementary data that is often publicly available. Y-NBS adds an additional narrowband to the existing data and uses this complementary data to further the science of the survey. See Section 2.4 for details of the ancillary data used in this work.

---

[1] `https://cosmos.astro.caltech.edu/`

Similarly, GOODS-S is a well-observed field. Probing extremely deep with legacy programmes from *HST*, *Spitzer Space Telescope*, *Chandra* X-ray telescope, *XMM-Newton* and the *Herschal Space Observatory*, the Great Observatories Origins Deep Survey (GOODS) aimed to study galaxy formation and evolution in the distant Universe [1]. This survey was split into GOODS-S and GOODS-N (south and north, respectively) and it is GOODS-S that we study. We once again utilise the multi-wavelength data available for GOODS-S, which is discussed more in Section 2.4.

We fully reduce the COSMOS data with a bespoke pipeline (see Section 2.3) and for GOODS-S we used the reduced image from Clément et al. (2012). Once reduced, we calibrate the data and extract sources from the images using SExtractor and from these full catalogues of narrowband-selected sources we select line emitters. The final sample of line emitters is then used in Chapters 3 and 4 to measure the luminosity functions of $z = 0.62 - 7.7$ Hα, [Oiii] [Oii] and Lyα emitters and probe the evolution of the cosmic star formation rate density and the epoch of reionisation.

In Section 2.2, we discuss the Y-NBS observations. Section 2.3 presents the data itself and fully details the data reduction pipeline. Sections 2.4 and 2.5 discuss the complementary archival broadband data, and the creation of catalogues of sources, respectively. In Section 2.6 we select line emitting sources, which includes deriving a colour-correction and cuts in equivalent width and excess significance. Finally, in Section 2.7 we summarise the findings.

2.2 Observations

2.2.1 Observational Overview

Y-NBS was conducted using HAWK-I on the Very Large Telescope (VLT) coincident with the UltraVISTA coverage of the COSMOS field (program: 098.A-0690; PI: David Sobral). For Y-NBS, a total of 69 pointings with the NB1060 filter were obtained in a 9×7 pattern, covering a total area of $0.8\,\mathrm{deg}^2$. The survey is made

---

[1] `https://www.stsci.edu/science/goods/`

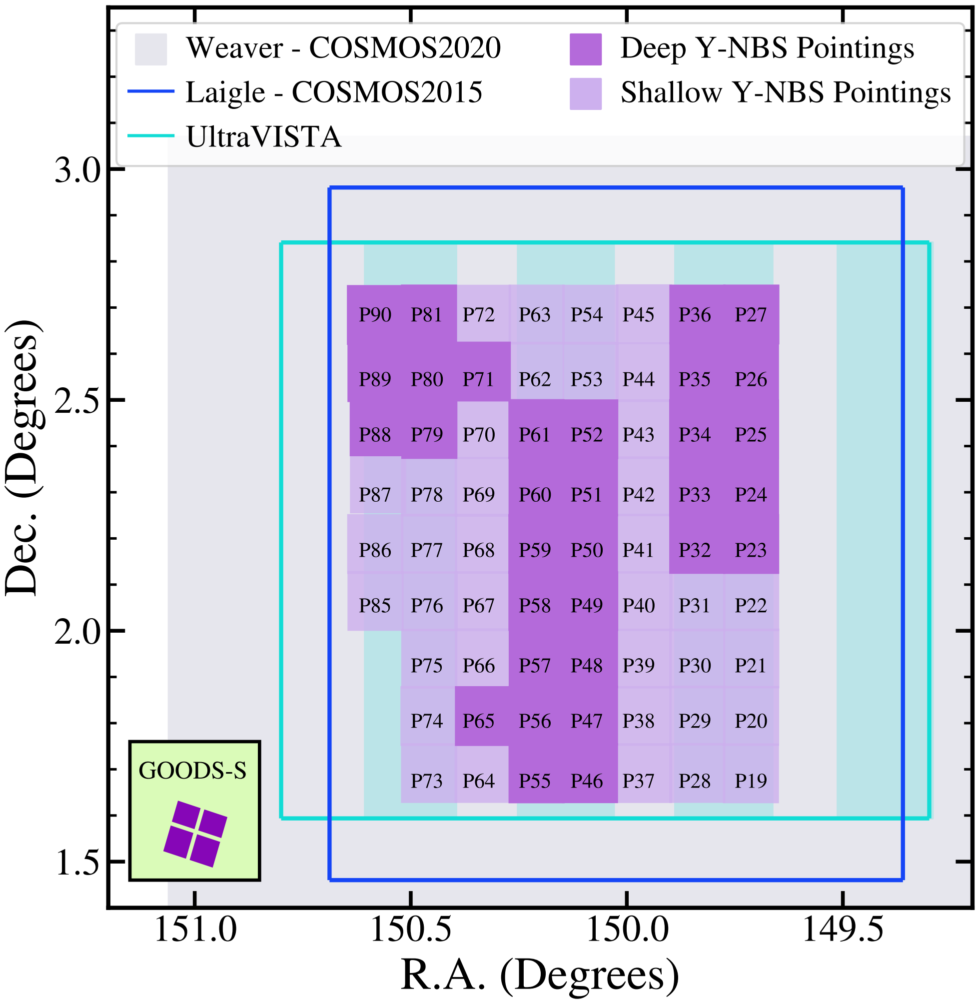

Figure 2.1: The Y-NBS footprint compared to existing COSMOS surveys. The grey shaded region shows the COSMOS2020 coverage (Weaver et al. 2022), which extends beyond the boundaries of this figure. COSMOS2015 covers the region inside the dark blue box (Laigle et al. 2016) and the ultra-deep UltraVISTA DR4 (McCracken et al. 2012) stripes are shown as the shaded cyan regions, with the cyan outline indicating the full extent of UltraVISTA. The purple numbered squares are the pointings in our Y-NBS survey, with the darker regions representing deeper pointings (2600–2800 second exposures), and light purple highlighting shallower pointings (600 second exposures). The Y-NBS survey is designed such that the deepest regions overlap with the deepest UltraVISTA data. The inset shows the single HAWK-I pointing in GOODS-S to scale, which is even deeper than our deepest COSMOS data (31.9 hour on-source; Clément et al. 2012). HAWK-I covers $7.5' \times 7.5'$ area using four chips and there is a $15''$ gap between the detectors as shown in the inset.

Table 2.1: Comparison between our COSMOS and GOODS-S data.

Field	Region	Area (deg^2)	Limiting Depth[a]	# NB1060 Emitters	# NB1060 Emitters after Visual Checks	% Removed with Visual Checks
COSMOS	Deep	0.38	23.5	616	599	2.76
	Shallow	0.42	22.7	454	417	8.15
GOODS-S	-	0.014	25.8	246	232	5.69
			Total	1316	1248	5.17

[a] Limiting depth given as 3σ limiting magnitude in $2''$ diameter apertures. The values for the COSMOS limiting depths correspond to the mean depths of the deep pointings and shallow pointings as indicated. For GOODS-S, there is only one pointing, so one value of depth.

up of two different kinds of pointings, which we refer to as deep and shallow: deep pointings have total exposure times of 2600–2800 seconds and shallow pointings have total exposure times of 600 seconds, with 100 seconds spent at each dither position in all cases. The layout of the individual deep and shallow pointings compared with existing COSMOS data is presented in Figure 2.1. VLT/HAWK-I observations were obtained between January 2017 and March 2018 with a total on-source time of 30.2 hours over all 69 pointings (see Table A.1 for details of the individual observations). The NB1060 filter is centred at 1.061μm at the edge of the Y-band, as shown in Figure 2.4. HAWK-I has a pixel scale of $0.106''$ and an on-sky field of view of $7.5' \times 7.5'$ across four detectors with a $15''$ chip gap between the detectors (Figure 2.1).

The NB1060 GOODS-S data were collected with VLT/HAWK-I as part of the ESO large programme 60.A-9284 between September 2008 and April 2010 (Clément et al. 2012). These data have 31.9 hours on-source in a single pointing, reaching a 3σ limiting magnitude of 25.8 mag with a seeing of $0.58''$. These GOODS-S data and are thus sensitive to fainter sources than Y-NBS in COSMOS, which helps to push our samples of line emitters to fainter galaxies. By combining the COSMOS deep, COSMOS shallow and ultra-deep GOODS-S data using uniform analyses we are able to probe a wide range of areas and luminosities.

2.3 Data Reduction

This section gives details of the data reduction pipeline that we developed for the VLT/HAWK-I NB1060 COSMOS data in Y-NBS. This pipeline is based on PfHiZELS (Sobral et al. 2013) with improvements and updates for dealing with HAWK-I data.

This full data reduction pipeline is necessary to get the best possible results from the data. Since these observations were carried out in 2017 and 2018 (see Table A.1), there is publicly-available ESO-reduced data available, where the raw data is run through ESO's data reduction pipeline for HAWK-I. The ESO-reduced images had noisy backgrounds and edges and inaccurate astrometry, so using these data products as they were was not an option. Our data reduction pipeline catered for the specific challenges for individual frames or quadrants, meaning that reprocessing the data reduction ourselves results in a higher quality data product with reduced noise, smoother backgrounds and high fidelity astrometry, when compared to the ESO-reduced images.

2.3.1 Overview of the Data

The HAWK-I instrument consists of four CCDs, so when referring to the data we refer to the four quadrants within each pointing, called Q1, Q2, Q3 and Q4[1]. The steps of the data reduction pipeline are carried out on images for each quadrant, rather than the pointing as a whole, so that settings can be optimised to account for the differences in the CCDs. Figure 2.2 shows the full, fully-reduced image of the pointing P90 with each of the quadrants labelled.

All science frames for each pointing were collected in the same night, with the requisite calibration frames. There are two types of calibration files: flats and darks. Flat fielding is required to correct for the pixel-to-pixel variation across the CCDs. Flats are two seconds exposures taken with the same filter as the science frame at twilight, when the sky is a constant brightness. The dark frames help to correct the science frames for thermal and electronic noise, caused by fluctuations on the CCD and during the readout. Dark frames are made by exposing the CCD

---

[1] Quadrants are named the same as in Casali et al. (2006)

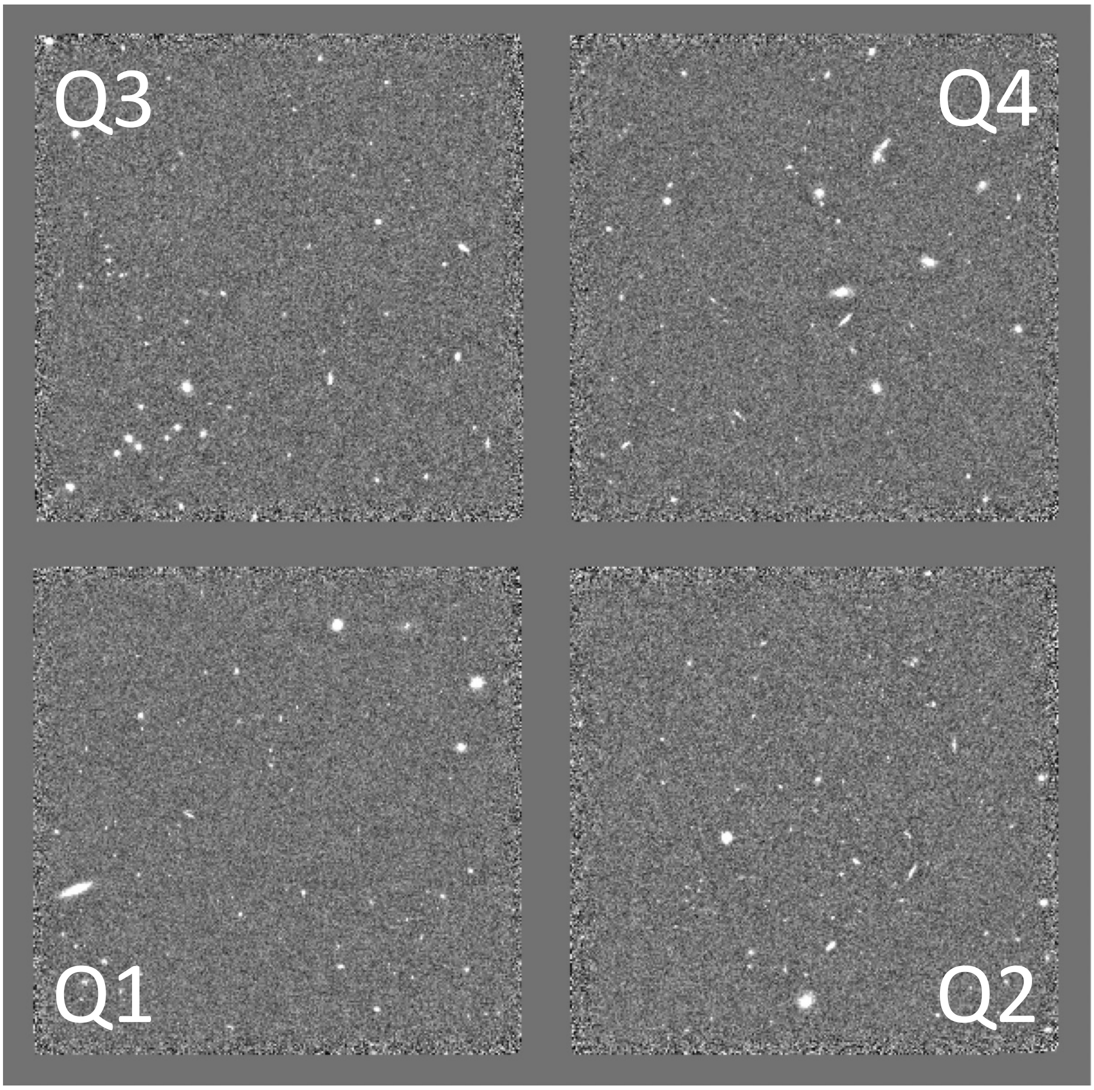

Figure 2.2: An example of the full pointing image of P90, with each quadrant labelled Q1 through Q4. This data has been fully reduced with PfHAWKI.

with the shutter closed (so the filter used does not matter) and the exposure times of the dark frame must match that of the science data. This means from the data package, we need to select the correct calibration frames from each night for each pointing. The correct flat frames are those using NB1060 and the correct dark frames are those with the same exposure time as the science frames (100 seconds) and those with the same exposure time as the flat frames (2 seconds).

The science frames are observed with an auto-jitter (or dither) pattern, where the telescope moves the centre of observation slightly each time. This helps to negate the effect of hot or damaged pixels. In these observations the dither pattern is insufficient to cover the chip gaps (Figure 2.2). When calculating the areas and volumes of the survey, only the regions containing sources are considered and the chip gaps are ignored. After dark correction and flat fielding the individual auto-jittered frames are combined using median stacking (Section 2.3.2) into one final science image.

2.3.2 PfHAWKI

Figure 2.3 visualises steps 1 through 4 of PfHAWKI and we can see improvements between the first image, the raw frame, and the final image, the self-flatted frame. The main steps of the data reduction that are done with PfHAWKI are as follows:

1. **Booking-keeping:**
   (a) Sort paths and directories ready for the data – one folder per pointing.
   (b) Download and decompress the raw data from the ESO Science Archive Facility.
   (c) Split the multi-extension FITS files into individual FITS files for each quadrant, rename file with useful information from the header.
   (d) Create list of filenames, file type and observation dates and sort files into relevant directories.

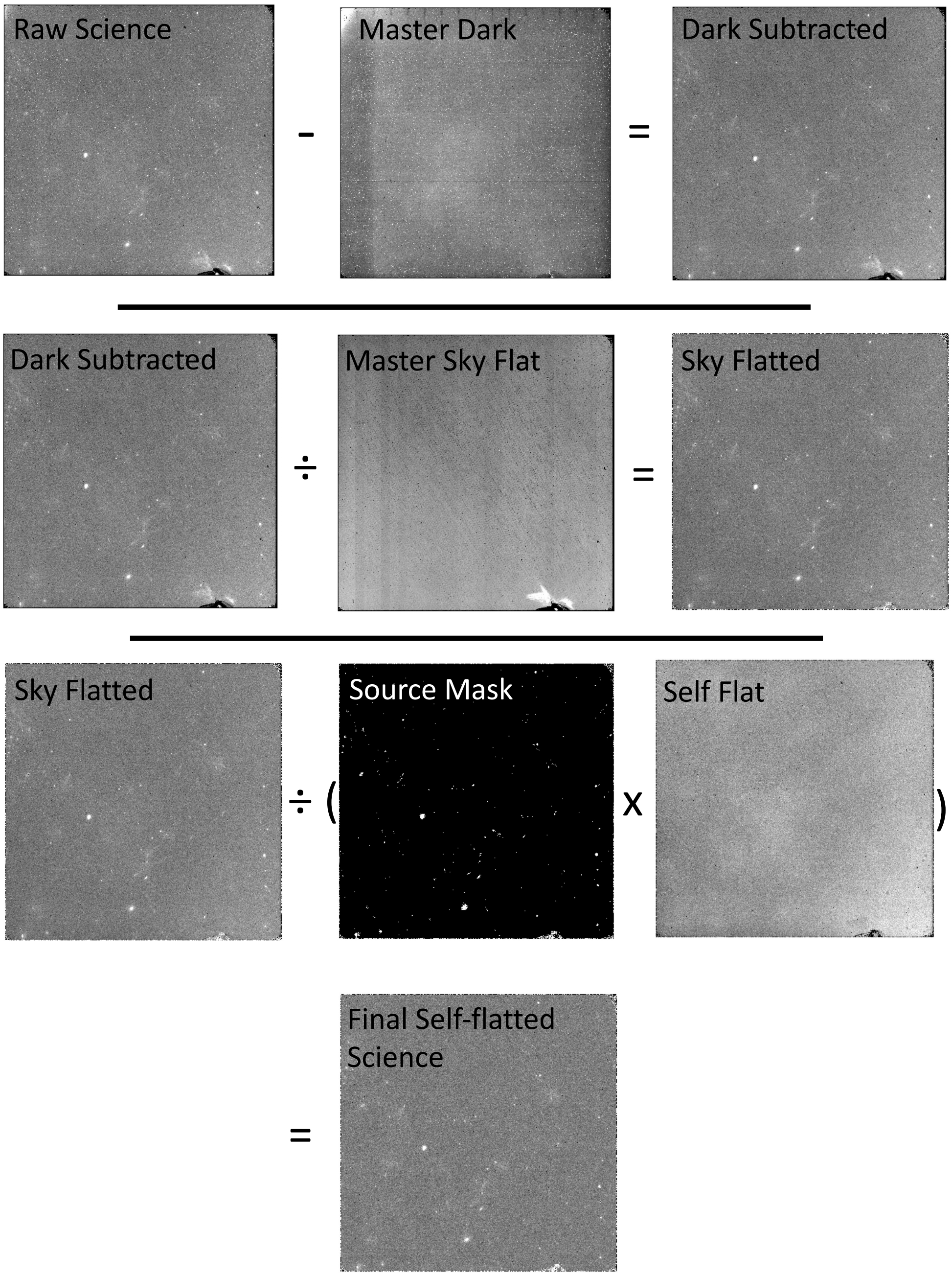

Figure 2.3: Visualisation of the dark subtraction, sky flatting and self-flatting steps of the data reduction pipeline to reach a final single-exposure self-flatted science frame. For all images shown white means a brighter source / region, but for the source mask on the third row it has been inverted so that the background is black and equal to 1 and the sources are white and equal to 0. The dark subtraction (top row) has removed the hot pixels and the sky flatting has removed the diagonal streaks in the background and has improved the artefact in the bottom right. Finally, the self-flatting step has further smoothed the background.

2. **Dark subtraction:**
    (a) Create a master dark frame for the science frames by median combining all of the dark frames with the same exposure time as the science frames.
    (b) Dark subtract the master dark frame from each of the raw science images (see the top row in Figure 2.3).
    (c) Create a master dark frame for the flat frames by median combining all of the dark frames with the same exposure time as the flat frames.
    (d) Dark subtract the master dark frame from each of the flat images.
3. **Sky flatting:**
    (a) Create a master sky flat field by median combining the dark-subtracted sky flats.
    (b) Divide the dark-subtracted science images through by the master flat to make a sky flattened science image (see row 2 of Figure 2.3).
4. **Self-flatting:** This step helps to remove fixed-pattern noise and hot pixels from the science frames and can be done because the individual science frames were auto-jittered, meaning that sources are at different pixels in each exposure.
    (a) For each science frame create a mask of sources using SExtractor (Bertin & Arnouts (1996)) to select all bright objects, and set pixels containing sources to have 0 value and set background pixels to 1.
    (b) Create a self-flat field for each science frame by masking and then median combining all other science frames.
    (c) Divide the dark subtracted and sky flatted science frame by its self-flat frame (see the final rows on Figure 2.3).

5. **Relative astrometry:** This step matches the coordinates of the science frames to the coordinates of the ESO reduced stack for each pointing, so that the science frames are aligned relative to each other and can be stacked (median-combined) correctly.
    (a) Run SExtractor (Bertin & Arnouts (1996)) on each science frame with relatively high settings (i.e. use a high threshold to only select the brightest sources) to select 15 to 30 bright sources, ideally spread across the whole frame.
    (b) Run SExtractor on the ESO reduced stack with relatively high settings (i.e. use a high threshold to only select the brightest sources) to select 15 to 30 bright sources.
    (c) Run SCAMP (Bertin (2006)) to match the selected sources in the science frame to the same sources in the ESO stack – this changes the astrometry information in the header to match the ESO pipeline data and sets the various dither positions to the same alignment. Further astrometry is performed in step 7.
6. **Stacking:** This step median combines the individual science frames to create a final stack per quadrant per pointing.
    (a) Manually check individual science frames and create masks for regions affected by satellite trails, cosmic rays and particularly troublesome or noisy regions from the detector.
    (b) Calculate the native zero-point of each science frame by selecting 17.0 – 21.0 mag sources with SExtractor (around 10 to 20 sources) and comparing them to their total Y–band magnitudes from Laigle et al. (2016).
    (c) Rescale the native zero-point to 30.0 mag for each science frame.
    (d) Median combine all reduced, masked, astrometrically and photometrically calibrated science frames using SWarp Bertin (2010) to create the fully-reduced stacks per pointing per quadrant.

7. **Final steps:**
    (a) Recalibrate the absolute astrometry per stack by following the method described for relative astrometry (steps 6(b) and 6(c), selecting 15 to 30 bright sources), but now by matching to the UltraVISTA $Y-$band image (McCracken et al. (2012)) so that the final images are astrometrically aligned with existing data.
    (b) Create a final mask by manually checking all stacked frames to see if specific regions need masking. In order to mask the noisy edges of each frame, identify and mask all regions with pixel values less than 60% of the median value.
    (c) Rescale the zero-points to 30.0 mag again, using the same method as in step 6(c).

We finish the data reduction with 276 high-quality science frames in COSMOS: one coadded stack per HAWK-I quadrant per pointing and a matching final mask. In GOODS-S the archival data (Clément et al. 2012) have already been processed and stacked, including a mask. We next discuss the broadband data that is used to complement the Y-NBS NB1060 data.

2.4 Ancillary Data

The COSMOS field (Capak et al. 2007; Scoville et al. 2007) has substantial archival multi-wavelength data, which complements our Y-NBS observations. For this study we use the broadband Y, J, H and K_S data from the UltraVISTA (DR4), an ultra-deep survey carried out by the VISTA survey telescope (McCracken et al. 2012) and Subaru Suprime-Cam images for the B, r', i' and z' bands (Capak et al. 2007). These data were used as they were the deepest, publicly-available images in COSMOS at the time of analysis. Filter profiles are shown in Figure 2.4. We extract our own photometry from these eight broadband images at the positions of the NB1060-selected objects (Section 2.6), which maximises the number of line-emitters with consistent measurements as needed for

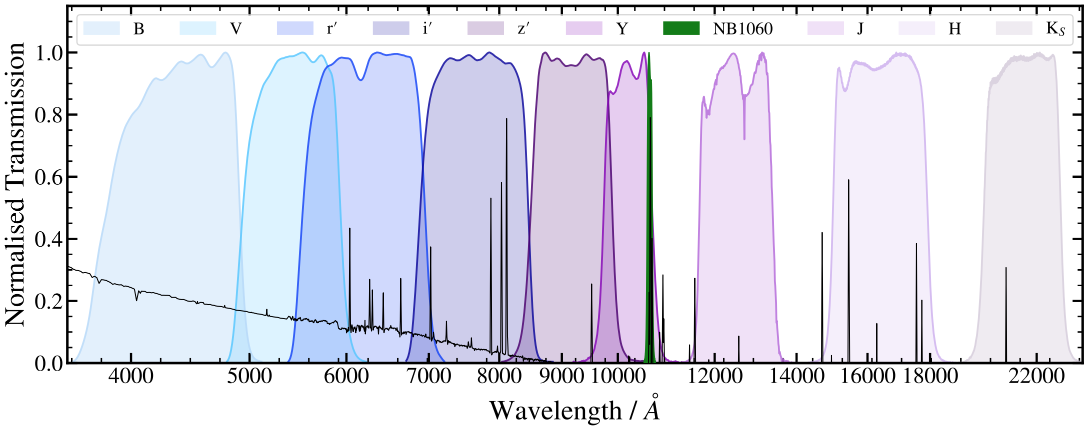

Figure 2.4: Normalised filter profiles for the Subaru Suprime-Cam B, V, r', i' , z', the VISTA Y, J, H, K_S bands used in for the COSMOS field. The VLT/HAWK-I NB1060 filter is shown in green. For GOODS-S the broadbands are from different instruments but the filter profiles are similar. The black line shows an example spectrum of a star-forming galaxy at $z = 0.62$, when the Hα line would cause excess flux to be observed in NB1060.

colour-corrections (Section 2.6.1) and when undertaking colour-based redshift estimates in Chapters 3 and 4. We also use photometric redshift data from Weaver et al. (2022), Laigle et al. (2016) and Ilbert et al. (2009) and the spectroscopic redshift data is from Hasinger et al. (2018).

For GOODS-S ancillary broadband data, we again extract our own photometry to allow for measurements at our exact NB1060-selected positions. We use VLT/HAWK-I images in the Y, J, H and K_S from Castellano et al. (2010), Clément et al. (2012), and Fontana et al. (2014). The B, R, I, z images are from MUSYC (Cardamone et al. 2010; Taylor et al. 2009) and the K_S band is from Fontana et al. (2014). In GOODS-S we use the photometric and spectroscopic redshifts from Hsu et al. (2014).

2.5 Catalogue Creation

To produce a catalogue of NB1060-selected sources we use the final coadded stacks and masks described in Section 2.3. Each HAWK-I quadrant (corresponding to a detector chip) is analysed separately to allow for variations between detectors.

To identify sources and measure their photometry in the NB1060, Y, J, H and K_S-bands, we use dual-image mode in SExtractor (Bertin & Arnouts 1996) with the NB1060 data as the detection image. Thus, the detections are wholly based on the narrowband emission, not continuum strength. Note, dual mode requires detection and measurement images to have the same pixel scale, so we change the Y, J, H and K_S images to have a pixel scale of $0.106''$ to match our HAWK-I NB1060 images. Zero-points for all bands (NB1060, Y, J, H and K_S) are set to 30.0 mag to ensure the correct identification of narrowband excess sources in Section 2.6.

We measure both fixed $2''$ aperture diameter photometery and SExtractor's 'MAG_AUTO', which extracts the total flux of each source. $2''$ corresponds to 13.6kpc at $z = 0.62$ (Hα), 16.4kpc at $z = 1.12$ ([OIII]) and 16.9kpc at $z = 1.85$ ([OII]). The resolution of the data (mean $0.7''$) is sufficient that $2''$ apertures recover the majority of the flux from high-redshift galaxies, although a small aperture correction is still required and applied. This is calculated by finding the average difference in MAG_AUTO and $2''$ diameter aperture magnitudes for bright sources and is determined separately for each quadrant and pointing to account for differences in resolution in the four HAWK-I chips.

To calculate the 3σ limiting magnitudes of each pointing (69 COSMOS pointings and 1 GOODS-S pointing), 3000 $2''$ apertures are randomly placed on the masked image as to only measure the background. The counts in the random apertures are measured and the limiting magnitude is derived by calculating the difference between the median and 99th percentile of these random aperture counts. Table 2.1 presents 3σ depths in the NB1060 data for the three regions that we study (COSMOS deep, COSMOS shallow and GOODS-S).

There are a total of 18,805 sources in the COSMOS deep pointings, 12,367 in the COSMOS shallow pointings and 4,396 sources in GOODS-S.

2.6 Selecting Line Emitters

For both Chapter 3 and Chapter 4 we need to select the line emitting galaxies from the catalogue of all NB1060-selected sources, by identifying sources that have an excess of flux in the narrowband NB1060 filter, compared with their broadband emission. In this section we describe the process of selection and classification of these objects, including further required calibrations.

2.6.1 Colour Correction

As Figure 2.4 shows, the NB1060 filter is at the edge of the Y-band, and therefore calculating the narrowband excess by subtracting the narrowband magnitude from the broadband magnitude would be misleading for sources with steep observed-frame Y-band SEDs. Instead, we calculate a synthetic broadband magnitude that is central to NB1060. By deriving a synthetic broadband magnitude at the centre of our narrowband we can accurately calculate the excess flux that is purely from any emission line.

The synthetic broadband magnitude, hereafter BB1060, is calculated using the J and H-band magnitudes, as follows:

$$\mathrm{BB1060} = J + \frac{\log_{10}(\frac{\lambda_{\mathrm{NB}}}{\lambda_J})}{\log_{10}(\frac{\lambda_J}{\lambda_H})}(J - H) \tag{2.1}$$

where J and H are the magnitudes in the J and H broadbands and λ_{NB}, λ_J and λ_H are the central wavelengths of the NB1060, J and H filters respectively. The full derivation of this equation is below in Appendix A.2.1.

We confirm that the BB1060 colour correction is the most reliable method of recovering the NB excess of line emitters by using simulations of emission lines. This testing involves simulating Hα, [OIII], [OII] and Lyα emission lines with varying widths, strengths, redshifts within the NB1060 filter, and adding these simulated lines to simulated galaxies with a range of brightnesses and UV continuum slopes. Simulated Lyman and 4000Å breaks were included for the Lyα and [OII] simulations, respectively. The simulated lines are convolved through NB1060 and the aforementioned broadbands so that BB1060 can be calculated per source and the NB excess flux (BB1060-NB1060) can be calculated and compared to the real NB flux of the source. The BB1060 colour correction was found to recover the intrinsic NB excess most reliably, with the smallest median offset and scatter when comparing to the other models tested (Figure 2.5 and Appendix A.2.2).

Figure 2.5 shows how the BB1060 colour correction recovers the NB excess compared to the input NB excess of the simulated sources. The black dashed line shows the one to one relationship between the recovered NB excess and the real NB excess. The flattening in the recovered excess in the plots for [OIII] and Lyα comes from the simulated sources being too faint to be recovered so the limiting flux is instead plotted.

Alongside testing how effective BB1060 is at recovering the NB excess for the simulated sources, a variety of other colour corrections were tested, using the Y, J, H and K-band photometry. For more information about the different colour corrections that were tested, including equivalent diagnostic plots, see Figure 2.5 and Appendix A.2.2.

The superiority of the J and H-bands for the calculation of BB1060 is likely because the Y-band contains flux from any emission line that is in NB1060 and the z-band picks up features such as the 4000Å break for [OII] emitters and the Lyman break for Lyα emitters. We note that sources that contain a break between NB1060 and the J-band may have their BB1060 flux overestimated by this method, which could lead to the some of these rare sources being excluded from our sample.

Calculating BB1060 requires the $J - H$ colour of each source (Equation 2.1). However, 10%, 11% and 19% of sources in COSMOS deep, COSMOS shallow and GOODS-S, respectively are not detected in both the J and H-bands. (The higher fraction in GOODS-S is due to the shallower H-band data relative to NB1060 in this field). Using sources with NB1060 = 17–21 mag that are detected in both bands, we calculate an empirical relationship between the average $J - H$ colour and NB1060 magnitude. This is measured for each field separately (COSMOS deep, COSMOS shallow and GOODS-S) and used to estimate $J - H$ when it cannot be directly measured. Equation 2.2 gives the empirical relation for the COSMOS deep data as an example; a different but similar relationship was found and used for the shallower COSMOS data and the GOODS-S data:

$$(J - H)_{\mathrm{av}} = -0.0447 \times \mathrm{NB1060} + 1.1145 \tag{2.2}$$

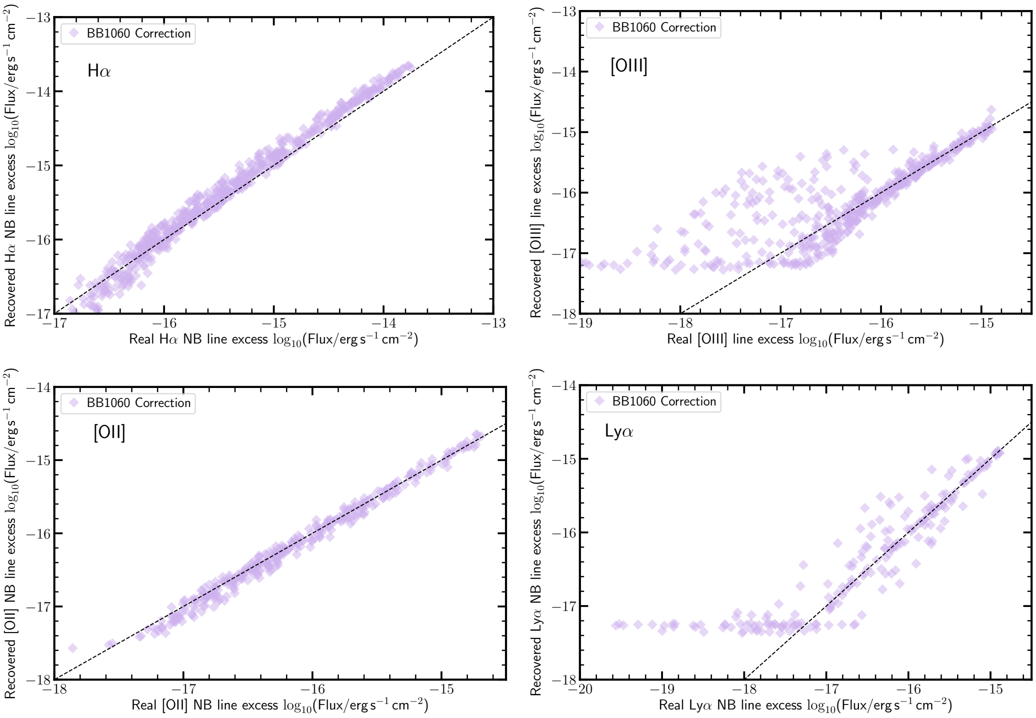

Figure 2.5: Real NB excess verses recovered NB excess for the BB1060 colour correction for the simulated Hα, [OIII], [OII] and Lyα lines. The dashed line shows the one to one relation between real and recovered narrowband excess. There is minimal scatter around this line for this BB1060 colour correction, and it yields the best results compared to other colour corrections (see Appendix A.2.2). Horizontal trends for faint objects are due to simulated line flux being too faint to recover.

Since the sources that are not detected in the *J*- and/or *H*-bands are generally faint there is insufficient information for reliable SED fitting, making this method the most practical way of accounting for such objects. Note that any source that is incorrectly identified at this stage will be removed during visual checks (Section 2.6.3).

To identify sources that have excess emission in NB1060 compared with the continuum, we examine the BB1060 − NB1060 colour. The average BB1060 − NB1060 colour is expected to be 0 (for non-line emitters), but a small offset is observed. We therefore select sources with NB1060 = 17–21 mag and run two iterations of a 3σ clip and calculate the mean colour of these sources. For all three samples the value of this additional correction is $\sim$0.2. The resulting BB1060 − NB1060 vs NB1060 colour-magnitude diagrams for the three fields are presented in Figure 2.6.

2.6.2 Selecting Line Emitter Sources

To select the line emitting galaxies within the sample we apply a number of criteria: a minimum NB1060 magnitude, a maximum colour, an equivalent width cut and an excess significance (Σ, Bunker et al. 1995) cut. A source must pass all of these tests to be considered a line emitter. This process of selecting line emitters follows many narrowband surveys (see also Geach et al. 2008; Khostovan et al. 2015, 2020; Matthee et al. 2017a; Sobral et al. 2015a, 2018; Stroe & Sobral 2015; Stroe et al. 2017). The minimum NB1060 magnitude is 15.0 mag, to avoid saturated sources. The selection method is visualised with colour-magnitude diagrams in Figure 2.6 and each criteria is explained below.

2.6.2.1 Observed Equivalent Width

The observed equivalent width (EW) of NB1060 line emitters is calculated using our synthetic BB1060 magnitude and the measured NB1060 magnitude as follows:

$$\mathrm{EW} = \frac{\Delta\lambda_{\mathrm{NB}} \times (10^{-0.4(\mathrm{NB1060}+48.60)} - 10^{-0.4(\mathrm{BB1060}+48.60)})}{10^{-0.4(\mathrm{BB1060}+48.60)}} \tag{2.3}$$

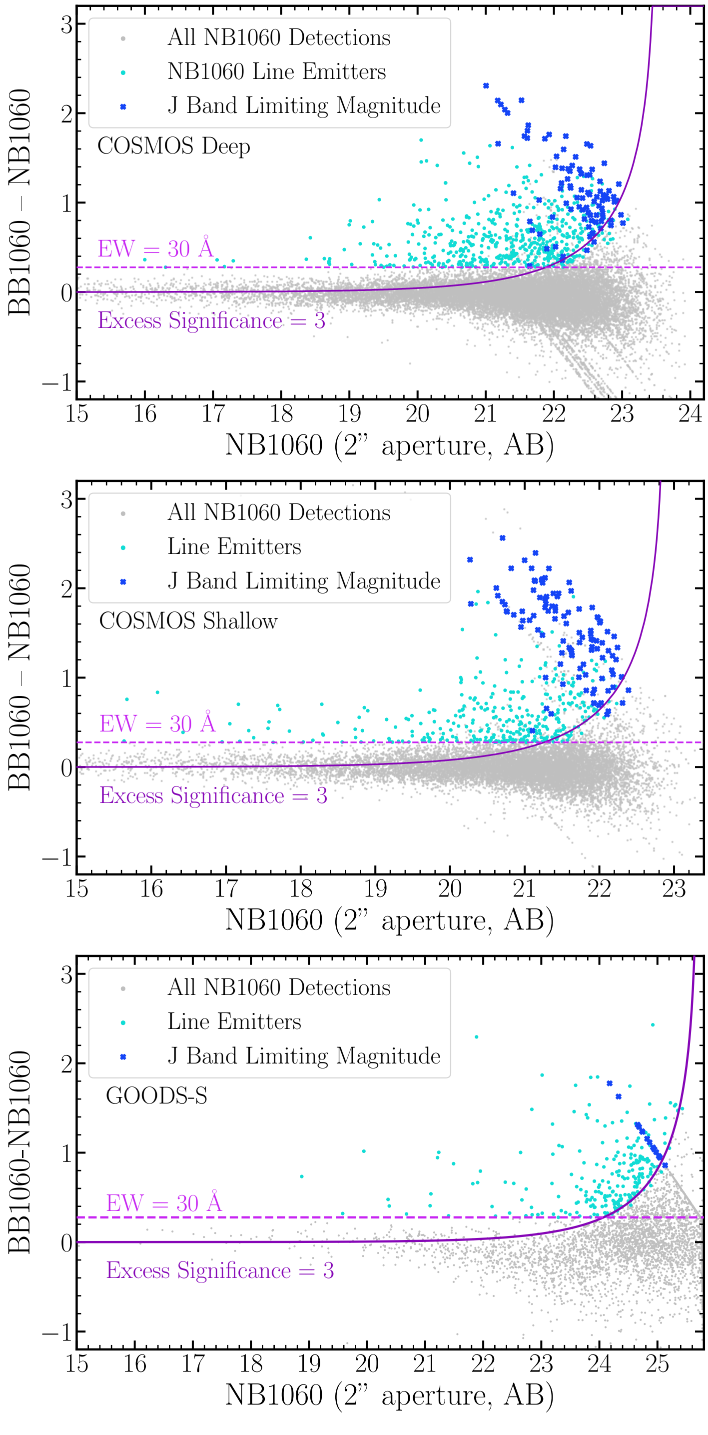

Figure 2.6: Colour-magnitude diagrams (BB1060 − NB1060 against NB1060) for all NB1060 detected sources in the COSMOS Deep, COSMOS Shallow and GOODS-S pointings *(top to bottom)*. Sources that are not detected in the *J*-band instead use the limiting magnitude in that band and are highlighted. The horizontal line shows the 30Å cut in EW and the solid purple line shows the 3Σ (excess significance) selection curve. Line emitters that are selected by these cuts are shown in light blue.

where $\Delta\lambda_{\rm NB}$ is the FWHM of the NB1060 filter and NB1060 and BB1060 are the magnitudes of the source in these bands.

To calculate a suitable EW cut to identify sources with unusually large EWs, caused by the presence of an emission line in NB1060 we consider sources with NB1060 = 17–21 mag, and remove outliers by requiring a BB1060 − NB1060 colour of $< \pm 0.2$ mag (Figure 2.6). The standard deviation (1σ) colour of the remaining sources is used to calculate the 3σ scatter in the BB1060 − NB1060 for calculating the EW cut using Equation 2.3.

For all three samples, GOODS-S, COSMOS deep and COSMOS shallow, the employed EW cut is 30Å.

2.6.2.2 Excess Significance

Excess significance (Σ, see Bunker et al. 1995) describes the significance of any excess lines emission, compared with the noise. It is calculated as:

$$\Sigma = \frac{1 - 10^{-0.4(\text{BB1060-NB1060})}}{1 - 10^{-0.4(\text{ZP-NB1060})}\sqrt{\text{rms}^2_{\text{BB1060}} + \text{rms}^2_{\text{NB1060}}}} \tag{2.4}$$

where ZP is the zero-point of the image (ZP = 30.0 mag for all images, see Section 2.3) and rms is the root-mean-square of the background counts of the BB1060 and NB1060 images.

To calculate the rms of the NB1060 data we measure the flux in randomly placed $2''$ apertures and calculate their standard deviation. However, there is no BB1060 image, and the rms in BB1060 must be extrapolated from the J and H-bands, as these are used to calculate BB1060. A simplified Monte Carlo simulation is used, taking the values of J and H-band counts for all detected sources as the input, because these follow a normal distribution. From 10,000 random values for each value of J and H-band counts, simulated BB1060 magnitudes are calculated using Equation 2.1 and the BB1060 rms is calculated, per quadrant per pointing.

To be considered a line emitter a source must have excess significance $\Sigma > 3$, as in previous studies (e.g. Khostovan et al. 2015, 2018; Sobral et al. 2013, 2018).

2.6.2.3 Maximum Excess

The third condition that a source must comply with to be selected as a line emitter is that it must be have BB1060 − NB1060 lower than a physical maximum. The need for this arises from the idea that a theoretical source could have pure line emission in NB1060, but no detectable emission in J and H and hence no BB1060 magnitude and a lower limit in BB1060 − NB1060. If a source is detected only in NB1060 then it cannot be real if it has a BB1060 − NB1060 $>$ 2.57. This value is full derived in Appendix A.3 This limit is calculated by determining the Y-band magnitude that a source with pure line emission would have if it were at the NB1060 saturation limit of 15 mag i.e. the limit in maximum excess is the most extreme colour that we could detect from a real source that is dominated by line emission, and anything above this limit is unphysical.

2.6.3 Visual Inspection of Potential Line Emitters

We visually check the full sample of potential line emitters identified in Section 2.6.2, in order to obtain the cleanest sample possible. Sources that are removed by visual checks are those that are either obvious artefacts or sources where the NB1060 magnitude would have been boosted by a nearby saturated star or by the noise around the edges of each image. As Table 2.1 shows, prior to visual checks there are 1316 line emitters across the COSMOS and GOODS-S fields; after visual checks, our final sample consists of 1248 good sources: 599, 417 and 232 in COSMOS deep, COSMOS shallow and GOODS-S, respectively.

2.7 Conclusions

In this chapter the Y-NBS survey was introduced. Y-NBS is a narrowband survey conducted in COSMOS using NB1060 on VLT/HAWK-I, supplemented with ultra-deep VLT/HAWK-I data in GOODS-S from Clément et al. (2012). We created a dedicated pipeline, PfHAWKI, for processing the COSMOS data, which included dark subtraction, flat-fielding, self-flatting, astrometric and photometric calibration and stacking. This process created final coadded stacks and matching masks, reaching a mean 3σ limiting magnitude of 25.7 mag.

From these final reduced stacks and the archival GOODS-S data, narrowband-selected sources were extracted to create a catalogue of all sources. Using conditions such as cuts in equivalent width and excess significance, narrowband-selected line emitters catalogues were created. The line emitter sample consists of 1248 total sources: 599, 417 and 232 in COSMOS deep, COSMOS shallow and GOODS-S, respectively. Chapter 3 will use the line emitter catalogues to select $z < 2$ Hα, [OIII] and [OII] emitters and study their luminosity functions and star formation rate densities. Chapter 4 use the line emitter catalogues to search for $z = 7.7$ Lyα emitters and study neutral fraction of hydrogen at this redshift.

Chapter 3

Y-NBS at Low Redshift: the Constrained Faint End Slopes of the Hα, [OIII] and [OII] Luminosity Functions

Abstract

We present the first results of a narrowband survey in the Y-band using HAWK-I on the Very Large Telescope. Our survey, Y-NBS, is in the COSMOS field and reaches a mean 3σ depth of 23.5 mag in the NB1060 filter, and uses 69 HAWK-I pointings to cover ~ 1 deg^2. To complement our new data we also explore archival ultra-deep observations in the GOODS-S field, which reach a 3σ depth of 25.7 mag in one pointing. We find a total of 921 line emitters across the two fields, in three redshift slices: 461 Hα emitters at $z = 0.62$, 281 [OIII] emitters at $z = 1.12$, and 148 [OII] emitters at $z = 1.85$. The survey is both deep and wide, probing comoving volumes of $(0.6 - 1.7) \times 10^5$ Mpc^3 at the different redshifts, enabling the simultaneous measurement of all three parameters ($\phi^\star$, L*, α) of Schechter function fits to the luminosity functions. In particular, we are able to constrain the faint-end slopes (α) finding $\alpha = -1.48^{+0.17}_{-0.17}$ for Hα at $z = 0.62$, $\alpha = -1.95^{+0.18}_{-0.15}$ for [OIII] at $z = 1.12$ and $\alpha = -2.43^{+0.19}_{-0.16}$ for [OII] at $z = 1.85$. The Hα, [OIII] and [OII] emitters trace the cosmic star-formation history of the Universe out to $z = 1.85$. Our results are consistent with previous studies, though there are hints of offsets which point towards the importance of simultaneously constraining α with $\phi^\star$ and $L^\star$ in analyses of luminosity functions and derived measurements. Surveys that probe both wide areas (to overcome cosmic variance at the bright-end) and that have deep regions (to detect faint sources) are thus required, and there is a particular need for surveys with deep regions within a wider area of the same field, to help understand any systematic density variation across the surveyed regions.

3.1 Introduction

As discussed in Section 1.4.4, luminosity functions are key tools for studying the luminosity distribution of galaxies, which is important for quantifying evolution and comparing the relative importance of different populations. Luminosity functions also help us to calculate the star formation rate density of a galaxy sample (by integrating under the function) which traces the evolution of star formation activity over the history of the Universe. In this chapter we take advantage of the wide and deep nature of Y-NBS, to probe both the bright and faint ends of the Hα, [OIII] and [OII] luminosity functions and study the star formation rate densities that these reveal.

Section 3.2 discusses how we select Hα, [OIII] and [OII] emitters from my line emitter catalogues created in Chapter 2: with photometric redshift cuts, spectroscopic redshift cuts and colour-colour cuts and the final sample is presented. From this we can construct luminosity functions per line and analyse them by comparing to literature results (Section 3.3). Using the luminosity functions, in Section 3.4, we calculate the star formation rate densities per line and compare them to literature results from $z \sim 5$ to $z \sim 0$.

3.2 Identifying Hα, [OIII] and [OII] Emitters

Now that line emitting galaxies have been selected (Chapter 2), the next step is to determine which line is causing the excess emission for each object and identify the Hα, [OIII] and [OII] emitters (see Section 1.2.4). Since the different emission lines will only fall into the NB1060 filter at specific (and different) redshifts, this process uses spectroscopic redshifts, photometric redshifts and colour-colour selection, as described below.

3.2.1 Spectroscopic Redshifts

For our line emitter sources, selected in Chapter 2, we try to match them to spectroscopic redshift values as these are the most reliable way to measure the distance

Table 3.1: Hα, [OIII] and [OII] emission line information, including the observed redshift of these lines and the co-moving volumes probed by Y-NBS at these redshifts. Also included are the photometric and spectroscopic redshift criteria for emission line selection and the number of sources observed, after visual checks.

Emission Line	Emitted Wavelength (nm)	Redshift	Comoving Volume ($\times 10^5$ Mpc^3)	Photo-z Criteria	Spec-z Criteria	# Line Emitters
Hα	656.28	0.62	0.6	0.3 – 0.8	0.610 – 0.626	461
[OIII]	500.70	1.12	2.2	0.8 – 1.5	1.110 – 1.131	281
[OII]	372.60	1.85	1.7	1.5 – 3.0	1.836 – 1.864	148

to galaxies. However, they are subject to biases. For example, spectroscopically-confirmed sources tend to be brighter and are often selected due to a bright continuum. There are numerous existing spectroscopic redshifts for many galaxies in COSMOS (Hasinger et al. 2018) and GOODS-S (Hsu et al. 2014). Spectroscopic redshifts have high precision, and therefore the criteria to identify a line emitter as being Hα, [OIII] or [OII] is based on the width of the NB1060 filter. Due to the precision of spectroscopic redshift values, the redshift range for each line is the redshift range covered by NB1060 (10567 – 10670 Å) as the spectroscopic redshift criteria to select a line emitter as a Hα, [OIII] or [OII] galaxy. We spectroscopically select 46 Hα sources across both fields in the range $0.610 < z < 0.626$, 9 [OIII] sources at $1.110 < z < 1.131$. One [OII] emitter ($1.836 < z < 1.864$) is identified spectroscopically, in the COSMOS field. These selections are summarised in Tables 3.1 and 3.2.

3.2.2 Photometric Redshifts

For sources that do not have spectroscopic redshifts we use photometric redshifts. The COSMOS line emitters are astrometrically matched to the $zYJHK_S$-selected COSMOS2020 photometric redshift catalogue (Weaver et al. 2022), which provides photometric redshift values by combining data from 17 broadbands, 12 medium bands and 3 narrowbands. The photometric redshifts in COSMOS have been extensively tested and a large number of filters bracket the 4000Å break.

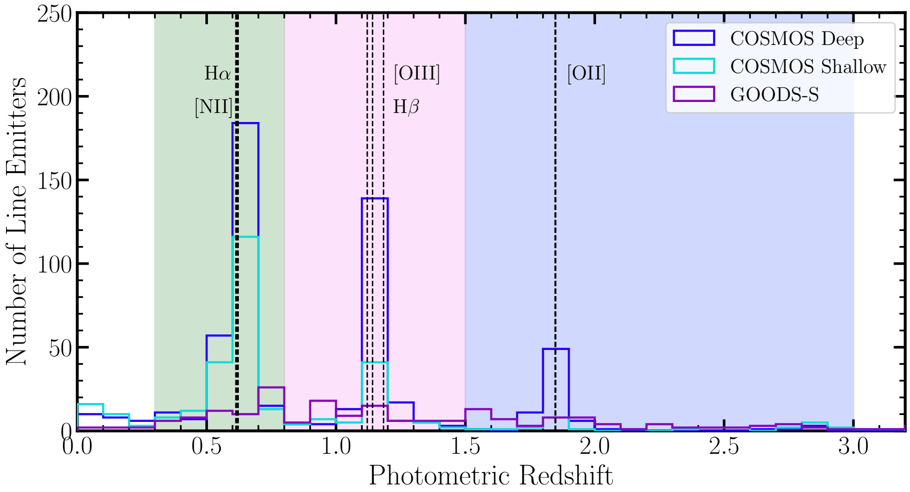

Figure 3.1: Photometric redshift distribution for the line emitters, with sources selected from the different survey regions shown in different colours. Shading highlights the photometric redshift regions used to select Hα, [OIII], and [OII] emitters. The clear peaks at the redshifts of the emission lines show that the narrowband selection has worked to select line emitters. Photometric redshifts are from Weaver et al. (2022), Laigle et al. (2016) and Ilbert et al. (2009) for COSMOS and Hsu et al. (2014) for GOODS-S.

Excluding galaxies with spectroscopic redshifts outside of our range of interest (Section 3.2.1), 537 and 342 (90% and 82%) of sources in COSMOS deep and COSMOS shallow, respectively, have photometric redshifts in Weaver et al. (2022). We also cross-match to COSMOS2015 (Laigle et al. (2016)) and to Ilbert et al. (2009), and if a source does not have a photometric redshift in COSMOS2020 we use the value from these catalogues. In GOODS-S we use the Hsu et al. (2014) photometric redshifts to obtain matches for 207 sources (89%).

Figure 3.1 shows the photometric redshift distribution of the GOODS-S, COSMOS deep and COSMOS shallow samples. There are defined peaks at the redshifts corresponding to Hα, [OIII] and [OII] in NB1060, and we highlight the photometric redshift range used to select for each emission line. These are $0.3 < z < 0.8$ for Hα, $0.8 < z < 1.5$ for [OIII] and $1.5 < z < 3.0$ for [OII]. Table 3.1 includes a summary of the selection criteria and Table 3.2 shows the number of sources selected per field from spectroscopic and photometric redshifts.

These relatively wide photometric redshift selection ranges are are chosen

Table 3.2: Number of sources selected per field, per line, either via their photometric redshift or spectroscopic redshift value or from our colour-colour selection.

		Number of Selected Sources			
Field	Line	Photo-z	Spec-z	Colour-colour	Total
COSMOS	Hα	332	45	35	412
	[OIII]	228	9	16	253
	[OII]	83	1	4	88
GOODS-S	Hα	49	1	9	59
	[OIII]	51	0	4	55
	[OII]	54	0	6	60

for completeness and to account for the uncertainty of photometric redshifts, particularly in GOODS-S, where the redshift uncertainties are higher (Hsu et al. 2014). As there are no other bright emission lines at rest-frame $\sim 2500 - 8000$Å, sources with photometric redshifts of $z = 0.3 - 3$ are unlikely to be interlopers and are most likely to contain one of the targeted emission lines at the targeted redshift.

3.2.3 Colour-Colour Cuts

As described in Sections 3.2.1 and 3.2.2, $\sim 15\%$ of line emitters do not already have measured spectroscopic or photometric redshifts. However, it is important to include these objects in our analyses for completeness and to avoid bias. To identify the redshift and thus measured emission line for these objects we apply colour-colour selections. Galaxies with confirmed photometric redshifts tend to have well-constrained stellar continuum emission across a wide range of wavelengths. However, emission line galaxies may not be detected in many continuum bands and therefore may not have well-measured photometric redshift, so would not make it into the sample without this step (Khostovan et al. 2020). We use three colour-colour cuts to identify these additional Hα, [OIII] and [OII] sources in the sample.

For the colour-colour diagrams and cuts, we require magnitudes in the B, r', i' and z' and K_S bands. To be as self-consistent as possible, we extract our own photometry in these bands. For this task we use the ASTROPY module PHOTUTILS

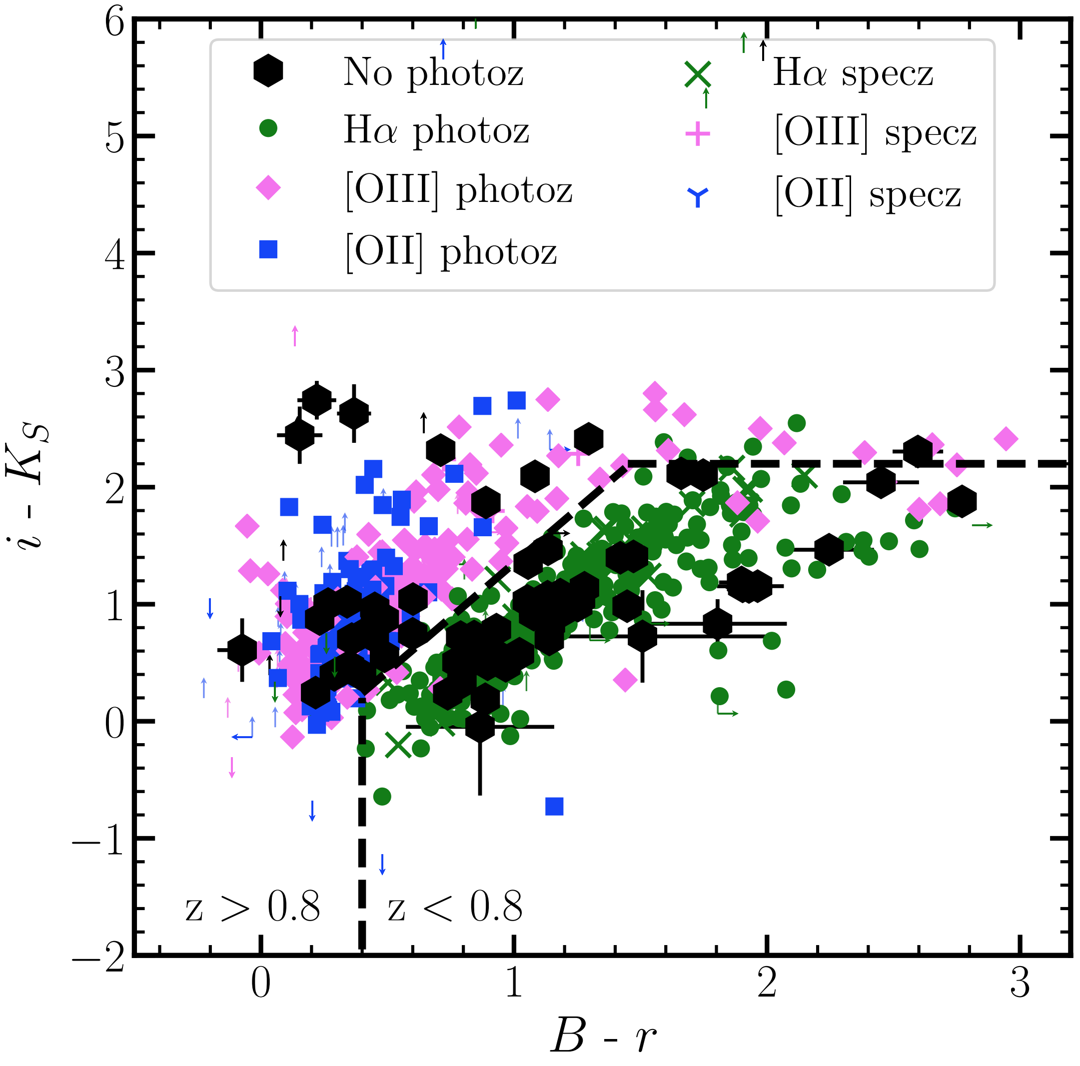

Figure 3.2: Colour-colour diagram in $i - K_S$ vs $B - r$ space for the full sample of line emitters (COSMOS and GOODS-S), with different symbols highlighting sources with different photometric and spectroscopic redshifts (Figure. 3.1). The line separates the colour-colour space with sources towards the top-left expected to be at $z > 0.8$ and sources in the bottom-right expected to be at lower redshifts (Section 3.2.3).

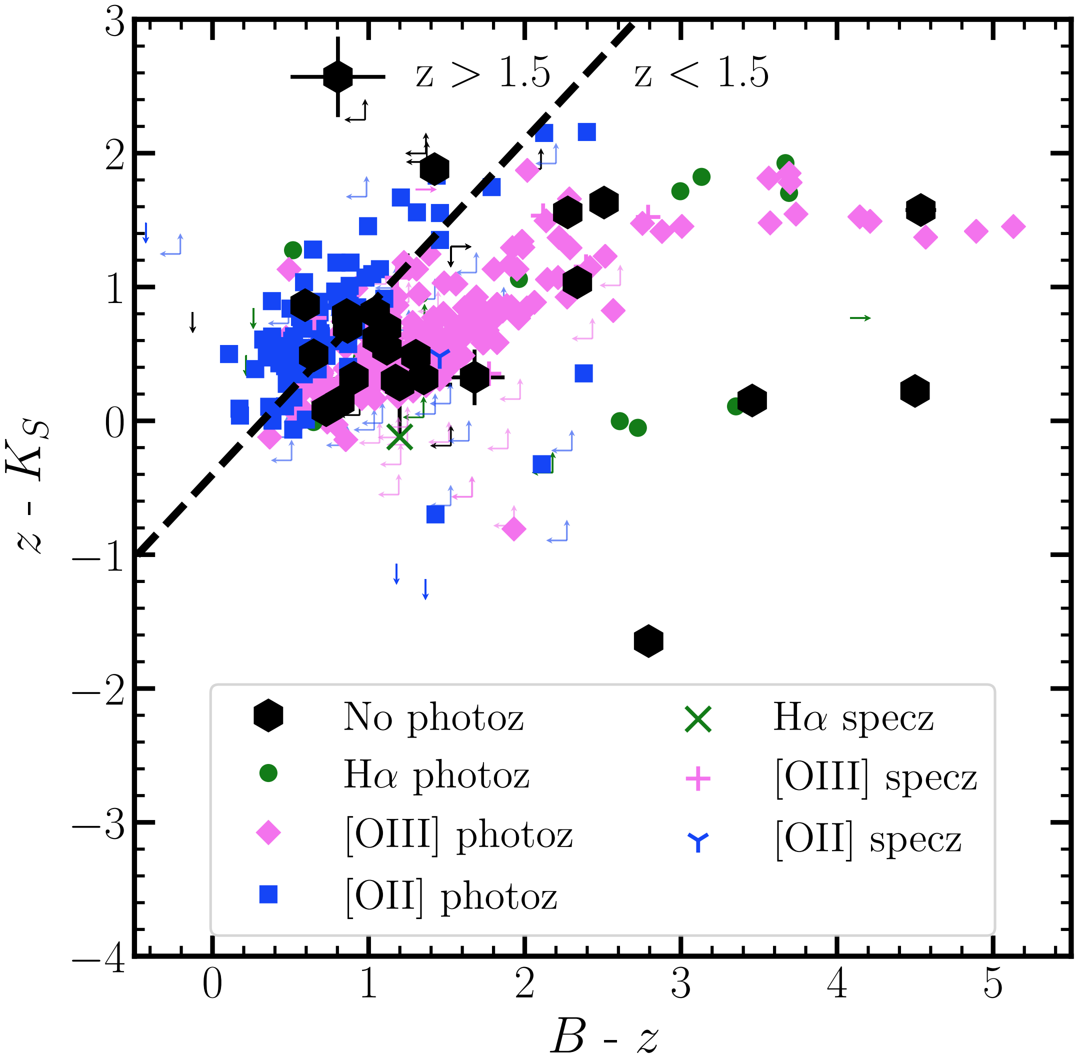

Figure 3.3: BzK_S diagram showing the line emitters from the $z > 0.8$ section of Figure 3.2. The dashed line separates sources to those above and below $z = 1.5$ (Section 3.2.3). In both panels the clear disaggregation between the different types of line emitters shows that classification according to colour is a robust way of identifying which of the line emitters without archival redshifts are caused by each emission line. Sources without existing photometric or spectroscopic redshifts are added to the Hα, [OIII] or [OII] sample on the basis of the their $B - r$, $i - K_S$, $B - z$ and $z - K_S$ colours.

(Astropy Collaboration et al. 2018, 2022; Bradley et al. 2020) to measure fixed aperture photometry at the exact position of the NB1060-detected line emitters. These measurements are aperture corrected, as discussed in Section 2.5. Hence, for the colour-colour plots, all photometry is extracted in a consistent way between bands, producing the most accurate results. Any source fainter than the limiting magnitude of that image, any source with a magnitude error greater than 0.75 mag ($< 3\sigma$) and any non-detection is replaced with the limiting magnitude of its respective image and is shown as a limit in Figures 3.2 and 3.3.

For the colour-based selections, we combine the data for COSMOS and GOODS-S. In Figure 3.2 (left) we use iK_SBr colour-colour space to split the sample at $z \sim 0.8$, following Sobral et al. (2015a). The precise location of the cut is selected to maximise the completeness of the photometric redshift Hα sample whilst minimising contamination from [OIII] and [OII] photometric redshift sources. The completeness of Hα in iK_SBr space (Figure 3.2) is calculated as the number of photometric and spectroscopic Hα sources that are correctly in the Hα region (below the dashed line) divided by all of the sources inside the Hα region. The contamination is the number of [OIII] and [OII] sources incorrectly in the Hα region, divided by the total number of sources in the Hα region (contamination = 1 − completeness).

Sources without spectroscopic or photometric redshift (black symbols in Figure 3.2) that meet the following criteria are identified as Hα emitters:

$$\begin{aligned} 0.4 < (B - r) < 5 \text{ and} \\ -5 < (i - K_S) < 2.2 \text{ and} \\ (i - K_S) < 1.85(B - r) - 0.5 \end{aligned} \tag{3.1}$$

Thus, this separates the $z = 0.62$ Hα sample from the $z = 1.12$ [OIII] and our $z = 1.85$ [OII] samples. The Hα completeness is 96.8% and the contamination is 3.2%.

Next, we take the $z > 0.8$ sample from the iK_SBr selection and examine these objects in BzK_S colour space, as shown in Figure 3.3. Again, this follows Sobral et al. (2015a) (see also Daddi et al. 2004), and splits the sample at $z \sim$

1.5; hence it is ideal for separating our [OIII] emitters at $z = 1.12$ from the [OII] sample at $z = 1.85$. The selection region is again optimised for completeness and contamination, which are calculated similarly to the Hα sample. In addition to not being selected by the criteria in Equation 3.1, both [OIII] and [OII] emitters are required to have $-2 < (B - z) < 5$ and $-4 < (z - K_S) < 5$, and [OIII] emitter must have $(z - K_S) < 1.25(B - z) - 0.4$ and the [OII] selection requires $(z - K_S) > 1.25(B - z) - 0.4$.

To summarise, all line emitters without photometric redshifts (black points in Figures 3.2 and 3.3) above the cut iK_SBr space, and below the cut in BzK_S are added to our [OIII] sample, and all those above the cuts in both iK_SBr and BzK_S are added to the [OII] sample. The [OIII] sample has a completeness of 84.3% and a contamination of 15.7%, and the [OII] sample has a completeness of 85.3% and a contamination of 14.7%.

3.2.4 Remaining Sources

After including spectroscopic and photometric redshift and colour-colour selection, a small proportion of our line emitters (31/921, 3.4%) remain unclassified. These sources are typically faint and are not detected in enough photometric bands to classify them using the methods in Sections 3.2.2. For these sources we take a statistical approach to include them in our analyses, in order to maximise the completeness of our Hα, [OIII] or [OII] luminosity functions.

We begin by separating the whole line emitter sample into flux bins of 0.2 dex and calculate the fraction of Hα, [OIII] and [OII] emitters in each bin. These fractions are then treated as probabilities for a given unknown source to be counted as an emitter of each line. To account for the unclassified sources in the luminosity functions, we first construct 100,000 realisations of each flux bin by taking the completeness corrected counts and perturbing them according to their uncertainties. We then include unclassified sources based on the above probabilities, such that the fraction of realisations that include the unclassified sources is approximately equal to the probability. To calculate the final counts that need to be added to each bin for each emission line, we take the mean of counts across

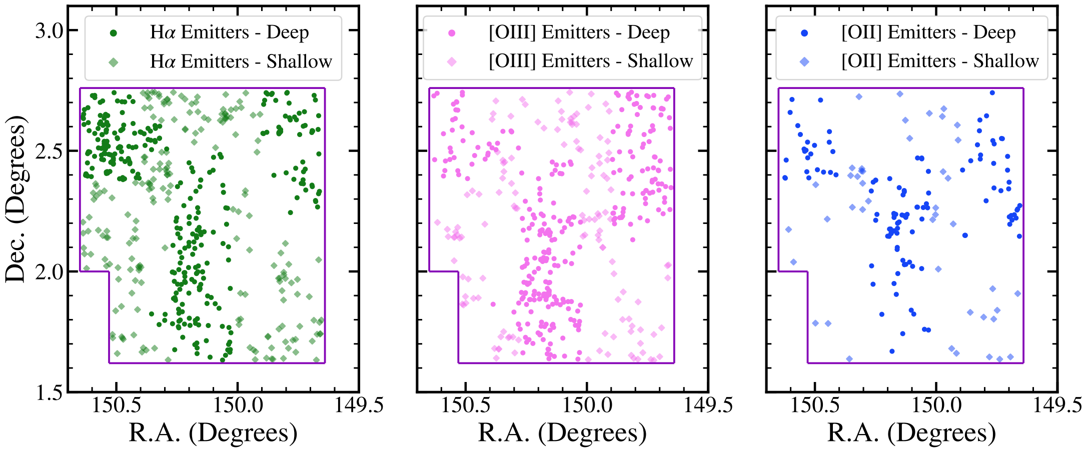

Figure 3.4: The spatial distributions of the (from left to right) Hα ($z = 0.62$), [OIII] ($z = 1.12$) and [OII] ($z = 1.85$) sources in the COSMOS field, with sources from the deep data shown with darker symbols and the Y-NBS survey area is outlined. As expected, the higher redshift slices have fewer sources and the deeper pointings contain more sources than the shallower pointings.

all realisations for each bin. The uncertainty in the final counts is the standard deviation across all realisations.

3.2.5 The Final Sample

The final Y-NBS sample contains: 461 $z = 0.62$ Hα sources, 281 $z = 1.12$ [OIII] sources and 148 $z = 1.80$ [OII] sources. There are 31 sources that remain unclassifiable as discussed in Section 3.2.4. The other 327 sources from the initial sample of 1248 narrowband-selected sources either have a spectroscopic redshift outside the ranges we consider, a photometric redshift greater than 3 or a photometric redshift less than 0.3, so are ignored going forward. See Table 3.1 for more information per emission line and Table 3.2 for the numbers that were selected via photometric redshift, spectroscopic redshift and colour-colour selection. Figure 3.4 shows the spatial distributions of the Hα, [OIII] and [OII] sources in the COSMOS field.

3.3 Luminosity Functions

Now that we have Hα, [Oiii] and [Oii] emitters selected via their narrowband emission and classified by spectroscopic redshift, photometric redshift, and colour-colour selection, we next construct construct luminosity functions for each line at their respective redshifts.

3.3.1 Line Blending and Survey Volumes

Our selection of Hα (6563Å) emitters is likely to also include the adjacent [Nii] lines at 6548Å and 6583Å, which will be picked up in NB1060 as a contaminant and will boost the inferred line flux. To correct for this contamination and estimate the Hα flux (excluding the contribution from [Nii]) we follow the method from Sobral et al. (2015a), which was derived from SDSS data and yields the following relation:

$$f([\mathrm{NII}]/\mathrm{H}\alpha) = -0.296 \times \log_{10}(\mathrm{EW}_{\mathrm{H}\alpha+[\mathrm{NII}]}) + 0.8 \tag{3.2}$$

where f([NII]/Hα) is the flux ratio between [Nii] and Hα and $\mathrm{EW}_{\mathrm{H}\alpha+[\mathrm{NII}]}$ is the rest-frame equivalent width. We use Equation 3.2 to remove the [Nii] contribution to the flux of the Hα sources, leaving the pure Hα contribution. The median decrease from applying this correction is $\sim 10\%$.

The [Oiii] line is a doublet, with emission at 4949Å and 5007Å, with the Hβ line (4862Å) also being close in wavelength. Due to these similar wavelengths, the narrowband filter will likely pick up both [Oiii] lines and the Hβ line in the [Oiii] sample. This contamination cannot be easily removed photometrically, so instead we account for it in the volume used to calculate the number density for the luminosity functions.

To compute the co-moving volume probed by the NB1060 filter for each emission line we first assume a top-hat filter and calculate a FWHM of 103Å (based on filter profile information[1]). This filter's central wavelength and FWHM (as-

---

[1] `https://www.eso.org/sci/facilities/paranal/instruments/hawki/inst/filters/hawki_NB1060.dat`

suming a top-hat filter) are used to calculate the redshift range probed by our study, using the following equations:

$$\lambda_{\text{max/min}} = \lambda_{\text{central}} \pm 0.5(\text{FWHM}) \tag{3.3}$$

$$z_{\text{min/max}} = \frac{\lambda_{\text{min/max}}}{\lambda_{\text{emitted}}} - 1 \tag{3.4}$$

where λ_{min} (λ_{max}) is the wavelength at 50% transmission to the left (right) of the central wavelength (λ_{central}), and z_{min} (z_{max}) is the redshift value corresponding to λ_{min} (λ_{max}), and λ_{emitted} is the rest-frame wavelength of the emission line in question (e.g. 6563Å for the Hα line).

From these z values, the ASTROPY module COSMOLOGY (Astropy Collaboration et al. 2018, 2022) is used to calculate the volume of the Universe up to each of these redshifts, and the difference is found:

$$\Delta V = V_{\text{max}} - V_{\text{min}} \tag{3.5}$$

However, this correlates to the volume of the entire sky in this redshift range so we next calculate the volume probed just within the area of observation, like so:

$$\text{V}_{\text{probed}} = \frac{\Delta \text{V}}{A_{\text{total}}} \times A_{\text{HAWK-I}} \tag{3.6}$$

where A_{total} is the total area of the sky ($\sim$ 41200 deg^2) and $A_{\text{HAWK-I}}$ is the area of one HAWK-I pointing ($\sim$ 0.0156 deg^2).

Thus, Y-NBS probes volumes of 6.59×10^4 Mpc^3, 2.18×10^5 Mpc^3 and 1.70×10^5 Mpc^3 for Hα, [OIII] and [OII], respectively. The difference between the assumed top-hat and true filter profile is accounted for when generating the luminosity functions, as described in Section 3.3.3.3.

For Hα we use the central wavelength of this line only for volume calculations. For [OIII], we follow Sobral et al. (2015a) and assume that [OIII]5007 dominates the sample, so we consider the full volume of this emission line, but we must also consider contribution from the the [OIII]4959 and Hβ emitters. Hence, we include 25% of the [OIII]4959 volume and 16% of the Hβ volume. This is an issue of misidentified lines, rather than direct contamination (such as with Hα and [NII]) so it is solved with a different approach. [OII] is a narrow doublet at 3726Å and 3729Å so the volume is calculated using the central wavelength of the two peaks (3727.5Å).

3.3.2 AGN Contamination

A small fraction of the sources that we have selected as line emitters will be powered by AGN (active galactic nuclei) rather than the star formation. Therefore, to calculate the star-formation rate density of our samples and discuss the star-formation history of the Universe (Section 3.4), we will need to remove the AGN contribution.

Hard X-rays are ideal for selecting pure AGN samples free of non-AGN interlopers. The *Chandra* X-ray observations the GOODS-S field (Luo et al. 2017) are deep enough to facilitate selection of a complete sample of both obscured and unobscured AGN, including those with luminosities below the "knee" of the AGN luminosity function. Thus, in GOODS-S X-ray matching alone is sufficient to remove AGN contamination from our sample (Hasinger et al. 2005). Using the Chandra Deep Field South 7Ms catalogue (Luo et al. 2017) we select AGN within our redshift ranges using a luminosity limit of $L_{X,\,2-10\ \mathrm{keV}} \geq 10^{42}$ erg s^{-1}, above which the X-ray emission requires an AGN contribution (i.e., above the high-mass X-ray binary limit). This identifies a total of 7 AGN in our GOODS-S line emitter samples: 2 in Hα (3%), 1 in [OIII] (2%) and 4 in [OII] (7%). These AGN are all found within the brightest two bins that GOODS-S covers. Given the known number density of X-ray sources within the footprint of GOODS-S (1.49×10^{-3} arcsec^{-2}) and their median positional uncertainty ($0.47''$, Luo et al. (2017)) we could expect there to be 0.14 chance alignments on average. We therefore conclude that at most 1 of these AGN contaminants is the result of chance alignment.

For COSMOS, the combination of X-ray catalogues available includes higher energies, which permits selection of more obscured AGN, but is not as deep as the coverage of GOODS-S. Therefore in COSMOS we supplement the X-ray selection with deep radio catalogues, to increase the completeness of the AGN identification. To identify X-ray AGN in our COSMOS sample, we turn to the COSMOS2015 Laigle et al. (2016) catalogue, which is matched to the *Chandra COSMOS-Legacy* Survey (Civano et al. 2016; Marchesi et al. 2016) and the XMM-COSMOS data (Brusa et al. 2010; Cappelluti et al. 2007; Hasinger et al. 2007). This X-ray data is then used in the COSMOS2015 LePhare SED fits and the catalogue includes a flag for an X-ray source (i.e. an AGN component). In order to search for COSMOS radio sources, we match our sample with the 3 GHz VLA observations, which reached a depth of 2.3μJy beam^{-1} (Smolčić et al. 2017). The 10,000 sources detected by this COSMOS VLA data were matched to COSMOS2015 (Laigle et al. 2016) by Smolčić et al. (2017), making it straightforward for us to identify any radio counterparts to our line emitters. We select AGN based on the `HLAGN` and `MLAGN` flags in this catalogue (see Smolčić et al. 2017 for details of the flags). In total, the AGN contamination rate for our line emitter in COSMOS are 3% (12 sources) for Hα, 4% (10 sources) for [Oiii] and 7% (6 sources) for [Oii]. Only three sources are identified by the radio selection (all in the Hα sample) that are not also selected via the X-ray data. Section 3.4 discusses our treatment of AGN when studying the star-formation history of the Universe. These 28 AGN are all found in the brightest three bins of their respective luminosity functions. COSMOS2015 employs a likelihood ratio technique (e.g. Sutherland & Saunders 1992) which is deemed more statistically accurate than a simple positional match (Laigle et al. 2016). We therefore assume no chance alignments in the X-ray COSMOS data. For the radio sources, Smolčić et al. (2017) use a rigorous matching process when matching to COSMOS2015 which accounts for chance alignments for each match. As we astrometrically match our narrowband images to the Y-band images from COSMOS2015, we can trust the matching process and assume that none of these AGN contaminants in our COSMOS data are due to chance alignment.

3.3.3 Measuring Luminosity Functions

We construct our luminosity functions using:

$$\phi(L) = \frac{1}{\Delta \log_{10} L} \sum_i \frac{1}{C(L_i) V_{max,i}} \tag{3.7}$$

where $\phi(L)$ is the number density, $\Delta \log_{10} L$ is the width of the bin, i is an individual source, $C(L_i)$ is the completeness correction of the individual source (Section 3.3.3.2), and V_{max} is the volume probed for that line at that given flux for the i^{th} galaxy. A quadrant's volume is only considered if it is $> 30\%$ complete at the flux value of the given bin. Poissonian uncertainties are included in addition to the uncertainties from cosmic variance (Section 3.3.3.1), completeness (Section 3.3.3.2) and filter-profile corrections (Section 3.3.3.3), all of which are shown in Figure 3.5. The final luminosity functions are shown in Figures 3.6, 3.7 and 3.8.

To parameterise the luminosity functions we fit Schechter functions (Schechter 1976) in their logarithmic form:

$$\phi(L)\mathrm{d}L = \phi^{\star} \ln 10 \left(\frac{L}{L^{\star}}\right)^{1+\alpha} e^{-(L/L^{\star})} \mathrm{d} \log_{10} L \tag{3.8}$$

where $\phi^{\star}$ and $L^{\star}$ are the characteristic number density and luminosity, respectively, and α is the faint end slope. This is fitted using a Markov chain Monte Carlo simulation of 10,000 iterations and the parameters of each luminosity function are given in Table 3.3 and the correlated uncertainties are presented in Figure 3.9.

3.3.3.1 Cosmic Variance

The faintest bins in our luminosity functions are probed by the GOODS-S data, and some of the COSMOS data (Figure 3.5). Since the GOODS-S data are based on only one HAWK-I pointing of 0.014 deg^2 they therefore probe a small volume and are affected by cosmic variance. In COSMOS a pointing only contributes to a bin of the luminosity function if it is $\geq 30\%$ complete in that bin (Section 3.3.3).

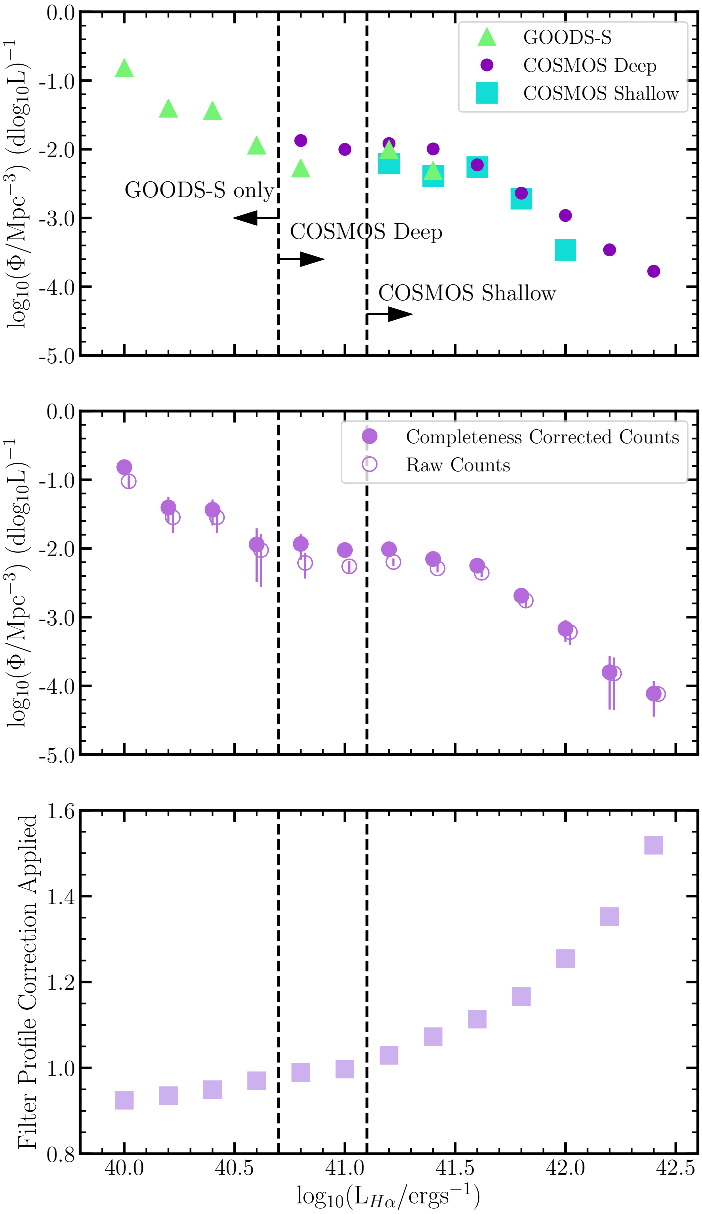

Figure 3.5: *Top:* The Hα luminosity function with the sources split by field. The ultra-deep GOODS-S data provides the only constraints for the four faintest luminosity bins, COSMOS deep contributes at $\log_{10}(\mathrm{L}_{\mathrm{H}\alpha}) > 40.7$, and at $\log_{10}(\mathrm{L}_{\mathrm{H}\alpha}) > 41.1$ COSMOS shallow is available. *Middle:* Comparison of completeness corrected counts and raw counts for the Hα sources, with a small offset in the x-axis for clarity. There is a larger completeness correction for bins with fewer sources, which is expected. The uncertainties are also larger after completeness-correction due to the inclusion of 20% of the completeness correction into the uncertainty (see Section 3.3.3.2 for details). *Bottom:* The value of filter profile correction applied each bin of the Hα luminosity function. The brightest bins are most affected by this correction, which accounts for bright sources being counted as faint sources if they are detected at the edges of the filter (see Section 3.3.3.3 for details).

Therefore, cosmic variance also needs to be considered for some of the bins with contributions from the COSMOS pointing. For bins with volumes $\leq 50\%$ of the total volume of the survey, we begin by identifying a luminosity range that is covered by the COSMOS deep sample but is as close as possible to the range probed by the GOODS-S data. Within this luminosity range, we count sources per pointing and convert to ϕ using the volume of that pointing. We calculate the standard deviation of the distribution of $\log_{10}(\phi)$ per quadrant and combine it in quadrature with the uncertainty in $\log_{10}(\phi)$ from the counts and other corrections.

This method increases the uncertainty on the fainter bins, which is visible in the error bars presented in Figures 3.6, 3.7 and 3.8. However, cosmic variance can act as a more systematic effect, impacting neighbouring bins that are all dominated by GOODS-S sources in a similar way. As explored in Section 3.3.4.3, if the luminosity at which the faint end slope (α) dominates the luminosity function coincides with the luminosity at which GOODS-S begins to contribute most to the measurements, then the systematic nature of cosmic variance could impact the derived α.

3.3.3.2 Completeness Correction

Sources with weak emission lines and low EWs can be missed by our selection, but they do contribute to the overall population of line-emitting galaxies and therefore must be accounted for. At fainter fluxes, a significant number of emitters could be missed by our sample selection, which is accounted for by using a completeness correction.

To evaluate the completeness of sources in each bin we start with a sample of non-line emitting sources (i.e. those shown in grey in Figure 2.6) in each HAWK-I quadrant. Following the empirical method used in similar surveys (e.g. Khostovan et al. 2015, 2020; Sobral et al. 2013, 2015a) we add flux in small increments to the NB1060 measurement for each of the non-emitter sources, and count how many now fall into the emission-line selection criteria (i.e. EW $> 30\,\text{Å}$ and $\Sigma > 3$; Section 2.6.2). For each step of additional flux we calculate the fraction of synthetic sources that are identified as line emitters and hence calculate the completeness, per line, pointing and quadrant. The flux range tested is 10^{-19} to

$10^{-13}\,\mathrm{erg\,s^{-1}\,cm^{-2}}$ in steps of 0.05 dex. This procedure is also used to calculate the flux limit at which each quadrant is 30% complete. Sources whose fluxes are below the 30% completeness limit for their quadrant are not considered hereafter.

Figure 3.5 (middle) shows the effect of the completeness correction on the initial luminosity function for Hα. For lower luminosity sources, the correction is larger, as expected, and at the brightest luminosities there is minimal completeness correction.

To account for the uncertainty in the completeness correction, 20% of the completeness correction value is added in quadrature to the error in the raw counts (the square root of the raw counts) and the error in the filter profile correction (3.3.3.3), following the method presented in Sobral et al. (2012).

3.3.3.3 Filter Profile Correction

The narrowband filter does not have the perfect top-hat profile, which was assumed for the volume calculations (Section 3.3.1), and the difference between the true filter profile and a top-hat function affects the observed luminosity function. Fainter sources will only be able to be detected at wavelengths towards the centre of the filter where transmission is high. Hence, the volume probed for faint sources is smaller than the volume of the top-hat filter assumed in Section 3.3.1. The opposite is true for bright sources: a wider range of wavelengths within the filter can pick up these bright sources and therefore a larger volume than that of a top-hat filter is probed. However, if a bright source is observed at the edges of the filter, it will appear to be fainter than it really is. These effects impact the shape of the luminosity function causing an overestimate of the number density of sources at the faint-end and an underestimate at the bright-end.

To correct for these effects we begin by fitting a Schechter function to an initial luminosity function, which is based on the completeness-corrected counts. We then simulate 10^7 mock sources with random luminosities according to the initial Schechter function fit and redshifts consistent with Hα, [OIII] or [OII] in the NB1060 filter. These simulated sources are convolved through both the real NB1060 filter and the top-hat model filter profile. The ratio between the number of sources recovered by the top-hat and the real NB1060 filter profile provides the required correction for each luminosity bin, and we divide the completeness-corrected counts by this filter profile correction. Figure 3.5 presents the filter-profile correction as a function of luminosity and demonstrates that (as expected) for the true NB1060 filter there is an increase in faint sources and a decrease in bright sources because of their positioning within the filter profile.

3.3.4 Analysing Luminosity Functions

Having now identified all the Hα, [Oiii] and [Oii] emitters in Y-NBS, their luminosity functions are initially constructed on a field-by-field basis, to check for any incomplete bins or biases. The top panel of Figure 3.5 shows this analysis for Hα and demonstrates only GOODS-S can probe the fainter luminosities (as expected due to its depth). At brighter luminosities, the COSMOS data dominates with a decreasing contribution from GOODS-S, which due to the small area of GOODS-S (0.014 deg^2).

Once any incomplete bins are removed, the counts from all three fields are combined, and the filter profile correction is applied (Section 3.3.3.3) to produce the final luminosity function for each line and redshift (Figures 3.6, 3.7 and 3.8). The luminosity functions are all fitted, using MCMC and with all three Schechter function parameters ($\phi^\star$, $L^\star$ and α) unconstrained. Unlike in some previous surveys (e.g. Bayliss et al. 2011; Khostovan et al. 2015, 2020), our GOODS-S data are sufficiently deep to constrain the faint-end slope, α, and our COSMOS data contribute to measuring $\phi^\star$ and $L^\star$. Note that the faint-end is dominated by GOODS-S data from only 0.014 deg^2, so the uncertainties on these bins account for cosmic variance (see Section 3.3.3.1), hence the larger error bars on the fainter bins in Figures 3.6, 3.7 and 3.8.

The Y-NBS $z = 0.62$ Hα, $z = 1.12$ [Oiii] and $z = 1.85$ [Oii] luminosity functions and associated Schechter function fits are presented in Figures 3.6, 3.7 and 3.8, compared with previous surveys at similar redshifts.

We discuss each line and redshift in detail in Sections 3.3.4.1, 3.3.4.2 and 3.3.4.3 for Hα, [Oiii] and [Oii], respectively. The results of the Schechter function fitting are given in Table 3.3, and Figure 3.9 presents corner plots from the MCMC analysis, which shows the correlation between parameters.

Table 3.3: Best-fit Schechter parameters and uncertainties for the three emission line luminosity functions: characteristic number density, $\phi^{\star}$, characteristic luminosity, $L^{\star}$, and the faint-end slope, α, for luminosity functions of all emission line sources in the fields (Section 3.3.4) and for AGN-corrected luminosity functions (Section 3.4). These are calculated from the MCMC fitting of the luminosity functions (Figures 3.6, 3.7 and 3.8) and the uncertainties are the 16th and 84th percentile from the probability distribution function for each parameter (Figure 3.9). The final column shows $\log_{10}\rho_{SFR}$, the SFRD for each line calculated from the AGN-corrected luminosity functions (Section 3.4).

Line	z	$\log_{10}(\phi^{\star})$ (Mpc^{-3})	$\log_{10}(L^{\star})$ ($\mathrm{erg\ s}^{-1}$)	α	$\log_{10}\rho_{SFR}$ ($\mathrm{M}_{\odot}\,\mathrm{yr}^{-1}\,\mathrm{Mpc}^{-3}$)
Total					
Hα	0.62	$-2.51^{+0.15}_{-0.19}$	$41.82^{+0.12}_{-0.09}$	$-1.48^{+0.17}_{-0.17}$	-
[OIII]	1.12	$-3.52^{+0.27}_{-0.27}$	$42.53^{+0.16}_{-0.15}$	$-1.95^{+0.18}_{-0.15}$	-
[OII]	1.85	$-4.08^{+0.53}_{-0.52}$	$43.01^{+0.26}_{-0.25}$	$-2.43^{+0.19}_{-0.16}$	-
AGN-corrected					
Hα	0.62	$-2.29^{+0.15}_{-0.23}$	$41.64^{+0.16}_{-0.11}$	$-1.30^{+0.20}_{-0.21}$	$-1.27^{+0.14}_{-0.12}$
[OIII]	1.12	$-3.36^{+0.25}_{-0.30}$	$42.4^{+0.16}_{-0.13}$	$-1.95^{+0.19}_{-0.17}$	$-0.95^{+0.21}_{-0.20}$
[OII]	1.85	$-2.62^{+0.21}_{-0.31}$	$42.57^{+0.17}_{-0.12}$	$-1.61^{+0.25}_{-0.26}$	$-0.47^{+0.20}_{-0.19}$

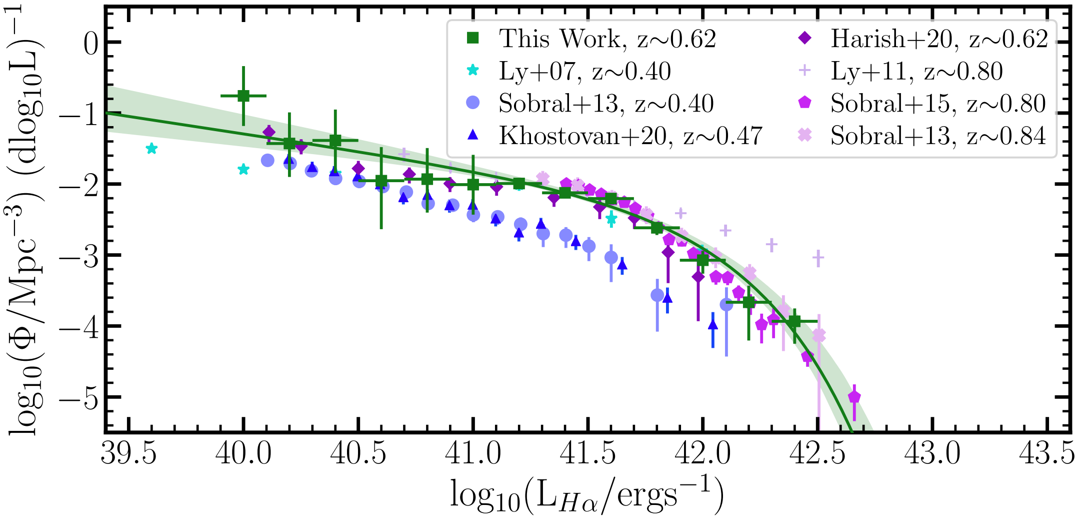

Figure 3.6: The $z = 0.62$ Hα luminosity function, with Y-NBS results shown in green, including the Schechter function fitted with all three parameters free. We compare to previously published results at $0.4 < z < 0.8$ (Harish et al. 2020; Khostovan et al. 2020; Ly et al. 2007, 2011; Sobral et al. 2013, 2015a). We are good agreement with previous results, and we probe a wider range of luminosities in a single, self-consistent survey, enabling simultaneous fitting of all three Schechter parameters. There is evidence of redshift evolution in the Hα luminosity function with points in shades of blue at $z \sim 0.4$ being below our data at $z = 0.62$ and other results in pink at $z \sim 0.8$.

3.3.4.1 Hα Luminosity Function

The Y-NBS derived Hα luminosity function at $z = 0.62$ is compared with the results from Harish et al. (2020); Ly et al. (2007, 2011); Sobral et al. (2013, 2015a), and Khostovan et al. (2020) in Figure 3.6 (top). Using bins of 0.2 dex our Hα luminosity function Schechter parameters are $\phi^\star = 10^{-2.51^{+0.15}_{-0.19}}$ Mpc^{-3}, $L^\star = 10^{41.82^{+0.12}_{-0.09}}$ erg s^{-1} and $\alpha = -1.48^{+0.17}_{-0.17}$. We reach a depth of log(Hα) = 39.9 erg s^{-1}.

The MCMC-derived corner plot in Figure 3.9 shows that all three parameters are well constrained, although there is some degeneracies between them.

We have not applied a dust correction to the Hα luminosity function, so our main comparison is with previous studies that also do not adjust for dust effects. To fairly explore the results from Harish et al. (2020); Ly et al. (2011); Sobral et al. (2013) we remove their constant 1 mag (0.4 erg s^{-1}) dust correction from the luminosity function.

Overall, when comparing to previous studies of varying areas and depths, we find good agreement and no systematic differences. There is potentially some redshift evolution in $L^\star$ and $\phi^\star$, as discussed in Sobral et al. (2013). Figure 3.6 shows that the $z \sim 0.4$ studies (Khostovan et al. 2020; Ly et al. 2007; Sobral et al. 2013) generally lie below our $z \sim 0.62$ Schechter fit, and the remaining higher redshift results (in shades of pink) lie on or above this.

The 1.5 deg^2 DAWN survey (Harish et al. 2020) also studied Hα emitters at $z \sim 0.62$, and Figure 3.6 shows good qualitative agreement with our results. Harish et al. (2020) does not include the parameters of Schechter fit without dust correction, so we apply our MCMC fitting to the Harish et al. (2020) data with the dust correction subtracted, finding $\phi^\star = 10^{-3.04^{+0.43}_{-0.39}}$ Mpc^{-3}, $L^\star = 10^{42.14^{+0.44}_{-0.42}}$ erg s^{-1} and $\alpha = -1.63^{+0.11}_{-0.09}$. Y-NBS provides better constraints on $\phi^\star$ and L* than Harish et al. (2020), with smaller uncertainties. All three of these parameters are in agreement within errors between the two surveys.

Due to the depth of the GOODS-S data, we can also fit α, the slope of the faint-end of the luminosity function. This is an important parameter, because it has a significant impact on the integral of the luminosity function, which is used to infer the cosmic star-formation rate density. The faint-end slope of the Hα luminosity function in our Y-NBS study is $\alpha = -1.48^{+0.17}_{-0.17}$. This is marginally shallower than Harish et al. (2020), which is also at $z \sim 0.62$, and is also shallower than the $z \sim 0.4$ and $z \sim 0.8$ studies that can constrain it (Figure 3.6). The exception is the Ly et al. (2007), which observed $\alpha = -1.28^{+0.07}_{-0.07}$ at $z \sim 0.4$, and probed ~ 0.5 dex deeper than the other Hα studies.

3.3.4.2 [OIII] Luminosity Function

Figure 3.7 shows the $z = 1.12$ [OIII] luminosity function for the full Y-NBS [OIII] sample, including the Schechter function fit and a comparison with Harish et al. (2020); Khostovan et al. (2020); Ly et al. (2007, 2011); Sobral et al. (2013, 2015a) at $z \sim 0.9$ and $z \sim 1.4$. We use bins of 0.3 dex and the best-fit Schechter parameters are $\phi^\star = 10^{-3.52^{+0.27}_{-0.27}}$ Mpc^{-3}, $L^\star = 10^{42.53^{+0.16}_{-0.15}}$ erg s^{-1} and $\alpha = -1.95^{+0.18}_{-0.15}$.

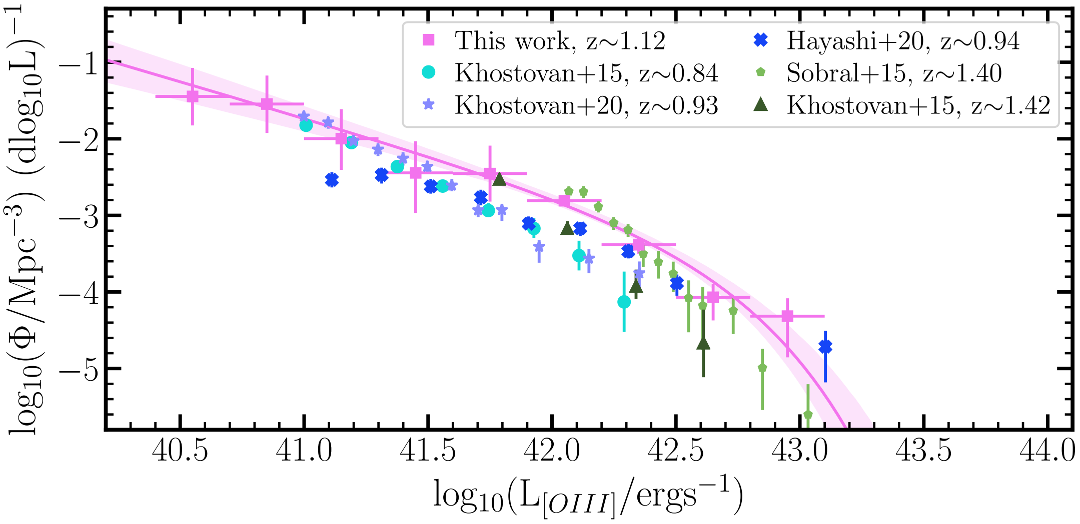

Figure 3.7: Our $z = 1.12$ [OIII] luminosity function and associated Schechter fit in pink compared with previous results at $0.8 < z < 1.4$ (Hayashi et al. (2020); Khostovan et al. (2015, 2020); Sobral et al. (2015a)). Our Y-NBS data are in good agreement with previous results, though we probe to a fainter luminosity in a single, self-consistent survey, enabling simultaneous fitting of all three Schechter parameters. There is no evidence of redshift evolution in this [OIII] luminosity function.

We reach an [OIII] depth of $\log(L) = 40.4$ erg s^{-1}, which ~ 0.5 dex deeper than previous studies.

The [OIII] corner plot in Figure 3.9 shows that both the derived $L^\star$ and α are correlated with $\phi^\star$, though the former two parameters are constrained independently of each other. The probability distribution shows that $\phi^\star$ is only weakly constrained, particularly at the faint end.

The $z = 1.12$ [OIII] luminosity function has not previously been measured, so we compare to studies at $z \sim 0.9$ and $z \sim 1.4$. Whilst there may be some evolution of the luminosity function in this range, our result is broadly consistent with the $z \sim 0.9$ and $z \sim 1.4$ studies, although is measured over a wider luminosity range than those works. Note that different studies of the [OIII] luminosity function treat the [OIII] doublet and Hβ volumes in different ways. Here, we follow Sobral et al. (2015a) and consider the total volume to be the full volume of the [OIII]5007 line, plus 25% of the [OIII]4959 volume and 16% of the Hβ volumes.

Khostovan et al. (2015, 2020); Sobral et al. (2015a) and Hayashi et al. (2020) find varying $L^\star$ with values from $10^{41.1}$ to $10^{42.1}$ erg s^{-1} with typical uncertainties of ~ 0.07 dex (up to 0.16 dex) and no redshift trend. Thus, the Y-NBS [OIII] luminosity function at $z = 1.12$ has marginally higher normalisation than past works ($L^\star = 10^{42.52^{+0.16}_{-0.15}}$ erg s^{-1}). Similarly, previous studies find significantly varying $\phi^\star$ with values from $10^{-3.12}$ to $10^{-2.16}$ Mpc^{-3} without a redshift correlation, and we measure $\phi^\star = 10^{-2.52^{+0.27}_{-0.27}}$, which is in agreement with the previous studies.

However, it is important to note that the faint-end slope, α, has a significant impact on the derived $\phi^\star$ and some effect on $L^\star$, due to the correlation between the different Schechter parameters (Figure 3.9). Neither Khostovan et al. (2015) nor Sobral et al. (2015a) were able to measure α, and fixed it to -1.6. Hayashi et al. (2020) and Khostovan et al. (2020) measured $\alpha = -1.33 \pm 0.19$ and $-1.57^{+0.35}_{-0.30}$, respectively. Thus, our derived value of $\alpha = -1.95^{+0.18}_{-0.15}$ is lower than used in previous work, in some cases, significantly lower. As Figure 3.9 shows, had we fixed $\alpha = -1.6$ (or higher) in Y-NBS, the derived values of $L^\star$ and $\phi^\star$ for the $z = 1.12$ [OIII] luminosity function would both have been closer to those estimated by the previous works. This demonstrates the need for simultaneous fitting of

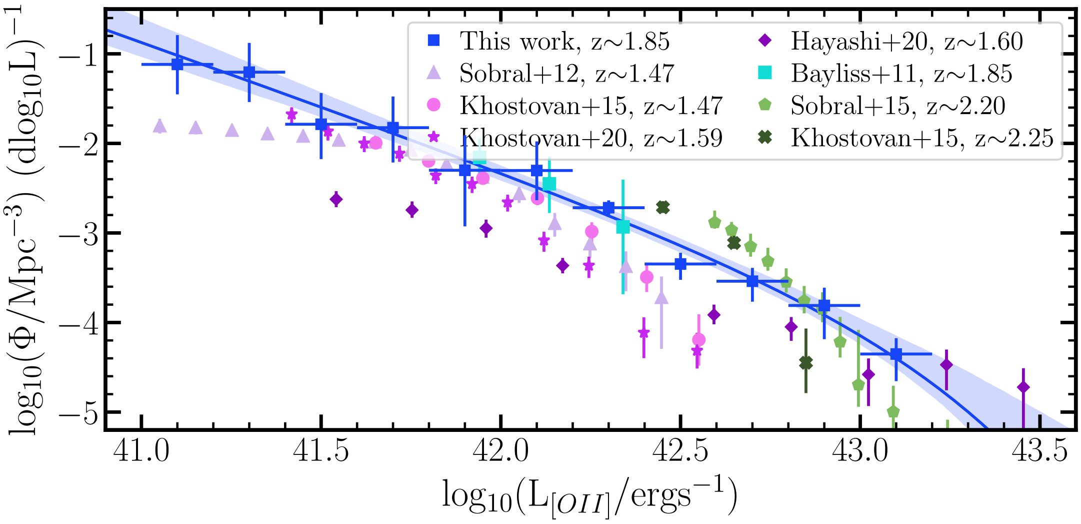

Figure 3.8: The Y-NBS $z = 1.85$ [OII] luminosity function and associated Schechter fit in blue compared with past studies at $1.5 < z < 2.3$ (Bayliss et al. (2011); Hayashi et al. (2020); Khostovan et al. (2015, 2020); Sobral et al. (2012, 2015a)). Shaded regions represent the 1σ uncertainty on the Schechter fits. Our Y-NBS data are in good agreement with previous results and we have probed a wide range of luminosities in a single, self-consistent survey, enabling simultaneous fitting of all three Schechter parameters. Our value of the faint-end slope, is $\alpha = -2.43^{+0.19}_{-0.16}$, which is steeper than other studies observe.

all three Schechter parameters, and deep and wide data that can constrain all parameters simultaneously.

3.3.4.3 [OII] Luminosity Function

The luminosity function for [OII] emitters at $z = 1.85$ is shown in Figure 3.8 and compared with Bayliss et al. (2011); Khostovan et al. (2015, 2020); Sobral et al. (2012, 2015a) and Hayashi et al. (2020) at $z \sim 1.5$–2.2. The best-fit Schechter function for our data has $\phi^\star = 10^{-4.08^{+0.53}_{-0.52}}$ Mpc^{-3}, $L^\star = 10^{43.01^{+0.26}_{-0.25}}$ erg s^{-1} and $\alpha = -2.43^{+0.19}_{-0.16}$. As with the [OIII] results, there is significant correlation between $\phi^\star$ and the two other Schechter parameters (Figure 3.9), and $\phi^\star$ is only loosely bound, particularly at the low end.

We note that the derived faint-end slope, α is less than -2, meaning that it formally diverges and therefore should be treated with caution. It is possible that

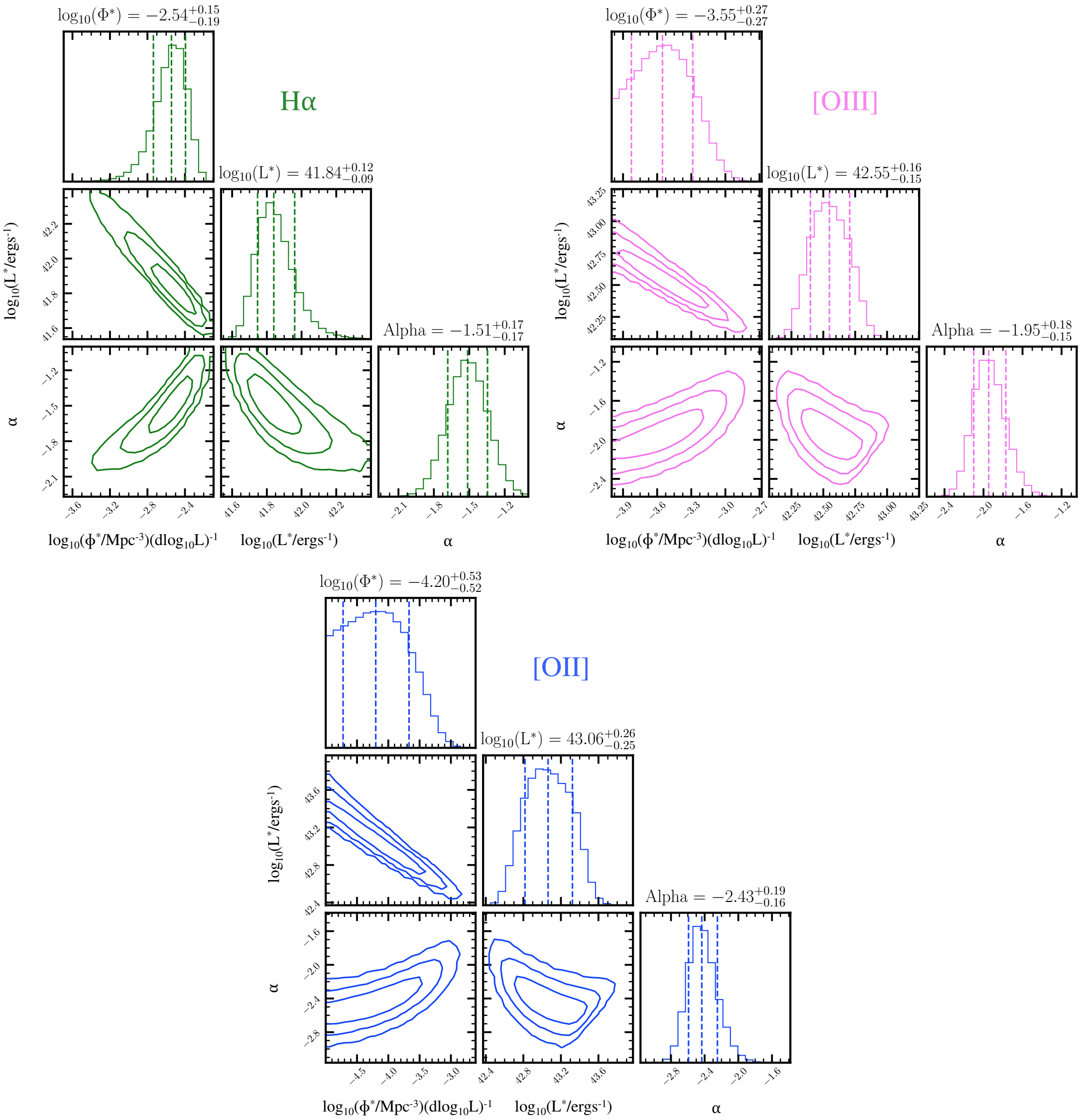

Figure 3.9: Corner plots from the MCMC fitting for the $z = 0.62$ Hα (top left), $z = 1.12$ [OIII] (top right) and $z = 1.85$ [OII] (bottom) luminosity functions. The three parameters, $\log_{10}(\phi^{\star})$, $\log_{10}(L^{\star})$ and α, are all free (not fixed) for the fitting. The contours show the 16th, 50th and 84th percentiles and the histograms are the probability distribution for each values, with the median, and 16th and 84th percentiles marked with dashed lines. The values above each probability distribution are the median and 16th and 84th percentile uncertainties for that parameter respectively. The median and the best fit values of the parameters are not always identical, and there is a strong correlation between some of the parameters.

the cosmic variance could cause a systematic offset between the faint bins (which are mostly sources from GOODS-S) and the brighter bins (which are mostly from COSMOS) and impact the derived α. In ideal future surveys, the regions with deep data would be embedded within wide-field data so as to better understand any systematic offsets between the average density and that in regions with deep coverage.

Only Bayliss et al. (2011) has previously studied the [OII] luminosity function at $z = 1.85$, using the same GOODS-S NB1060 HAWK-I data as examined here. However, where we detect GOODS-S sources as faint as $L \sim 10^{41.0}$ erg s^{-1}, Bayliss et al. (2011) observe them only from $L \sim 10^{42.0}$ erg s^{-1}. The difference is due to the two studies using different final steps of data reduction, different EW cuts when selecting line emitters (we use a 30Å cut compared to a 50Å cut in Bayliss et al. 2011), and different photometric and spectroscopic catalogues and redshift selection criteria. Our results are consistent with Bayliss et al. (2011), but the combination of GOODS-S and COSMOS data means that we probe $\sim 4\times$ the luminosity range and reach down fainter luminosities (Figure 3.5).

Existing measurements of the [OII] luminosity function at $z \sim 1.5$–2.2 show potential evolution, with $L^{\star}$ appearing to increase and $\phi^{\star}$ showing hint of becoming more negative with redshift.

As Figure 3.8 shows, at $z \sim 1.60$ the Hayashi et al. (2020) luminosity function is significantly lower than the other results at the faint-end, but finds more bright sources, with an almost flat bright-end. Our [OII] faint-end slope is steeper than those found by previous studies that were able to measure it, with a value of $\alpha = -2.43^{+0.19}_{-0.16}$, compared with $\alpha = -1.98$–0.90 (Hayashi et al. 2020; Khostovan et al. 2020; Sobral et al. 2012). The only previous study with comparable depth is Sobral et al. (2012) at $z = 1.47$, which measured $\alpha = -0.9 \pm 0.2$; the difference is clearly apparent in Figure 3.8.

3.4 Star Formation History of the Universe

We use the Hα, [OIII] and [OII] luminosity functions (Section 3.3.4) to measure the SFRD at $z = 0.62$, $z = 1.12$, $z = 1.85$. This is done by applying an AGN correction, a dust correction and then integrating the Schechter function fit to each luminosity function, over the full range of observations, to give ρ_L, the luminosity density in erg s^{-1} Mpc^{-3}. ρ_L is then converted to SFRD, $\rho_{\rm SFR}$ (in M$_\odot$ yr^{-1} Mpc^{-3}) using the relationships from Kennicutt (1998) and Osterbrock & Ferland (2006), which all use a Salpeter IMF, as described in Sections 3.4.1, 3.4.2 and 3.4.3.

The AGN correction is performed by identifying the sources that are flagged as AGN (described in detail in Section 3.3.2) and removing them from the number density calculation and refitting the Schechter function. Note that the luminosity functions plotted in Figures 3.6, 3.7 and 3.8 do include the AGN sources we have found, as do the other results that they are compared to. Removing the AGN from the fitting changes the shape, and therefore area under, the Schechter function. The difference in the shape after removing the AGN is not significant, as most of the sources selected as AGN are at the bright end - see Table 3.3 for the parameters with and without the AGN correction. The final SFRD and its uncertainties are derived by calculating the median and 16th and 84th percentiles of the SFRD for 10^4 random iterations of the AGN-corrected Schechter parameters within their uncertainties.

Prior to converting the observed line luminosities into star-formation rates we also corrected for dust extinction. For Hα the dust correction used is $\rm A_{H\alpha}$ = 1 mag, following Sobral et al. (2015a). There is no direct measure of the typical dust extinction of the [O III] line in $z > 1$ galaxies, so for this tracer we follow Sobral et al. (2015a) and convert $\mathrm{A}_{H\alpha} = 1$ mag to the [O III] wavelength of 5007Å, which gives $\rm A_{[OIII]} = 1.5$ mag.

Hayashi et al. (2013) studied [O II] emitters at $z \sim 1.47$ finding $\rm A_{H\alpha} = 0.2$ mag in these systems (i.e. on average they are less dusty than $z \sim 0.6$ Hα emitters). Converting $\rm A_{H\alpha} = 0.2$ mag to $\rm A_{[OII]}$ gives a dust correction of $\rm A_{[OII]} = 0.4$ mag, which has been used for [O II] emitters out to $z \sim 2.2$ (Sobral et al. 2015a) and is what we use for the $z \sim 1.85$ [O II] emitters here.

3.4.1 SFRD from Hα

For the $z \sim 0.62$ Hα emitters, we use the star formation calibration from Kennicutt (1998) (Salpeter IMF) to convert from luminosity density (ρ_L) to star formation rate density ($\rho_{\rm SFR}$, SFRD):

$$\frac{\rho_{\rm SFR}({\rm H}\alpha)}{M_\odot\,{\rm yr}^{-1}\,{\rm Mpc}^{-3}} = 7.9 \times 10^{-42} \frac{\rho_L}{{\rm erg}\,s^{-1}{\rm Mpc}^{-3}} \tag{3.9}$$

The integration limits are from the luminosity range covered by the Hα sample, from $L = 10^{39.9}$ erg s^{-1} to $L = 10^{42.5}$ erg s^{-1}. We find $\log_{10}(\rho_{SFR}) = -1.27^{+0.14}_{-0.12}$ $M_\odot\,{\rm yr}^{-1}\,{\rm Mpc}^{-3}$ at $z \sim 0.62$, which is in good agreement with the trend from previous Hα-based studies (Harish et al. 2020; Khostovan et al. 2020; Ly et al. 2007; Shioya et al. 2008; Sobral et al. 2013, 2015a; Stroe & Sobral 2015; Westra & Jones 2008; Westra et al. 2010) in Figure 3.10.

3.4.2 SFRD from [OIII]

For the [OIII] SFRD calculation, we use Osterbrock & Ferland (2006) (Salpeter IMF) to convert from luminosity to SFR density:

$$\frac{\rho_{\rm SFR}([{\rm OIII}])}{M_\odot\,{\rm yr}^{-1}\,{\rm Mpc}^{-3}} = 7.35 \times 10^{-42} \frac{\rho_L}{{\rm erg}\,s^{-1}{\rm Mpc}^{-3}} \tag{3.10}$$

As described in Sections 3.3.1 and 3.3.4.2, for the the [OIII] volume calculations we use the full volume of the [OIII]5007 line, plus 25% of the [OIII]4959 volume and 16% of the Hβ volumes (from Sobral et al. 2015a). The integration is performed over the full range covered by the observations i.e. from $L = 10^{40.4}\,{\rm erg\,s^{-1}}$ to $L = 10^{43.1}\,{\rm erg\,s^{-1}}$. Our result of $\log_{10}(\rho_{SFR}) = -0.95^{+0.21}_{-0.20}$ $M_\odot\,{\rm yr}^{-1}\,{\rm Mpc}^{-3}$ is compared with Khostovan et al. (2015); Ly et al. (2007); Sobral et al. (2015a) and Khostovan et al. (2020) in Figure 3.10. The uncertainties on this measurement are significant, and our result is consistent with the expectations from previous studies, though it is more in line with the Khostovan et al. (2015, 2020); Sobral et al. (2015a) results than the Ly et al. (2007) results, which trend slightly lower.

This is likely due to the different approaches to fitting the luminosity functions, in particular the use of fixed α in some studies (Section 3.3.4.2).

3.4.3 SFRD from [OII]

To calculate SFRD from the the [OII] emitters at $z \sim 1.85$ we use the calibration from Kennicutt (1998) (Salpeter IMF):

$$\frac{\rho_{\mathrm{SFR}}([\mathrm{OII}])}{M_{\odot}\,\mathrm{yr}^{-1}\,\mathrm{Mpc}^{-3}} = 1.4 \times 10^{-41} \frac{\rho_L}{\mathrm{erg}\, s^{-1}\mathrm{Mpc}^{-3}} \tag{3.11}$$

which gives SFRD $= \log_{10}(\rho_{SFR}) = -0.47^{+0.20}_{-0.19} M_{\odot}\,\mathrm{yr}^{-1}\,\mathrm{Mpc}^{-3}$ for an integration between $L = 10^{41.0}$ $\mathrm{erg\,s^{-1}}$ and $L = 10^{43.2}$ $\mathrm{erg\,s^{-1}}$. This is compared with the measurements from previous studies of [OII] (Bayliss et al. 2011; Ciardullo et al. 2013; Khostovan et al. 2015; Ly et al. 2007; Sobral et al. 2015a; Takahashi et al. 2007) in Figure 3.10. Within the uncertainties, our measurement of SFRD at $z \sim 1.85$ is consistent with expectations from previous work. However, it is higher than Bayliss et al. (2011) at the same redshift, and higher than the expected trend from observations at other redshifts. This is likely due to us finding a steeper faint-end slope as discussed in Section 3.3.4.3.

3.4.4 Evolution of SFRD

Figure 3.10 presents the evolution of the SFRD from $z \sim 5$ to $z \sim 0$ as measured by studies of Hα, [OIII] and [OII] and compared with the empirical fit from UV and far-IR data from Madau & Dickinson (2014). The Hα-based fit from Sobral et al. (2013) and the [OII] fit from Khostovan et al. (2015) are also shown. The Sobral et al. (2013) result is based on data from $z \sim 0.4$–2.23 and is unconstrained at higher redshifts. Similarly, Khostovan et al. (2015) has measurements out to $z = 4.69$ and is therefore not shown beyond $z = 5$ in Figure 3.10.

The evolution of the SFRD measured from Y-NBS in this study is consistent with all three empirical fits (Khostovan et al. 2015; Madau & Dickinson 2014; Sobral et al. 2013), showing the highest star-formation rate density in our $z \sim 1.85$ [OII] sample, with a decrease to our $z \sim 0.62$ Hα sample.

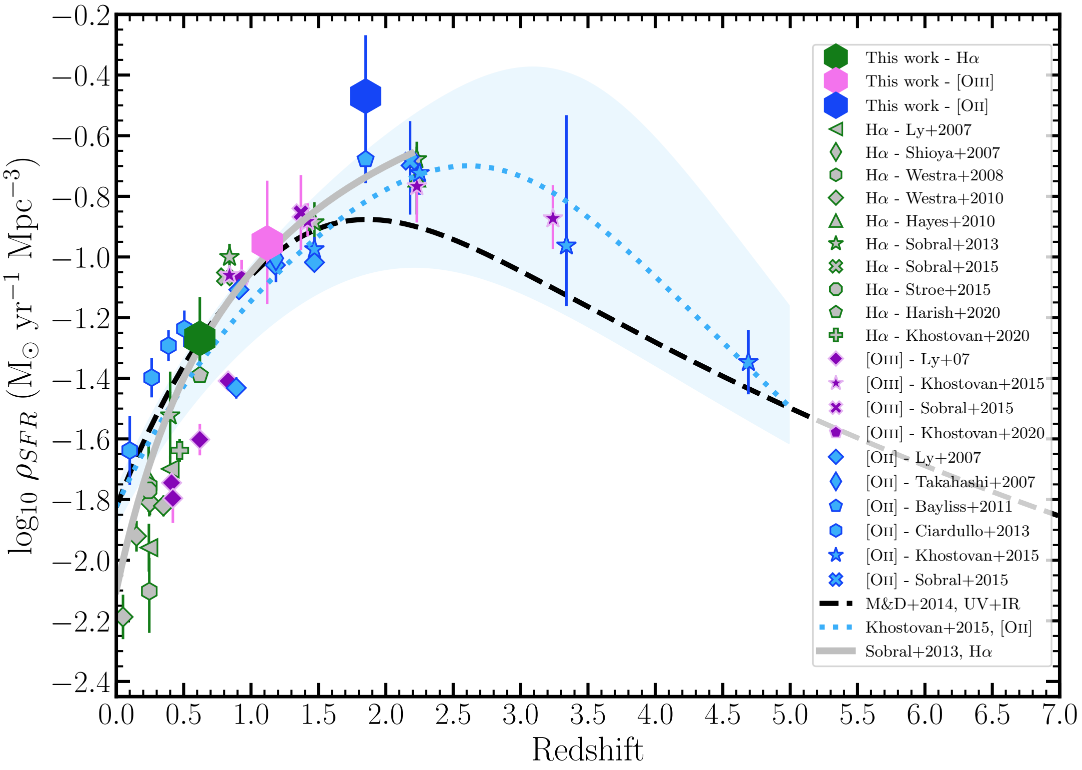

Figure 3.10: The star formation rate density of the Universe, evolving up to $z \sim 5$. The results from our Y-NBS survey are shown as hexagons with 1σ error bars: green for Hα at $z = 0.62$, pink for [OIII] at $z = 1.12$ and blue for [OII] at $z = 1.85$. Results from previous surveys using the same emission lines are shown as similarly coloured smaller symbols. We include the fit to Hα sources from Sobral et al. (2013), which is measured up to $z \sim 2.2$. The Khostovan et al. (2015) fit to [OII] sources up to $z \sim 5$ is shown with its 1σ uncertainty region. The black dashed line is the combined results from many UV and IR galaxy surveys presented by Madau & Dickinson (2014). Y-NBS is in good agreement with previous results, with the highest SFRD of our redshift slices being that at $z = 1.85$ and traced by [OII] in the VLT/HAWK-I NB1060 filter.

At $z \lesssim 1$ there appears to be a systematic offset between results based on [OII] emission (Ciardullo et al. 2013) and those from Hα studies (this work; Harish et al. 2020; Khostovan et al. 2020; Ly et al. 2007; Sobral et al. 2013, 2015a; Stroe & Sobral 2015; Westra & Jones 2008; Westra et al. 2010), which may be due to dust correction, or different measured or assumed faint-end slopes (α) of the luminosity functions. Harish et al. (2020) also measured the faint end slope of the Hα luminosity function at $z = 0.62$ and found $\log \rho_{\mathrm{SFR}} = -1.39$ for a constant dust correction (just below our point in Figure 3.10). Both our result and that from Harish et al. (2020) bridge the gap between previous [OII] and Hα data, which is likely due these studies being deep enough to measure α directly.

Khostovan et al. (2020) found that their Hα sample was in better agreement with previous measurements of SFRD than their [OIII] and [OII] results, and suggested that this implied that [OIII] and [OII] emitters are weaker tracers of star formation activity.

However, in this study we have found that Hα, [OIII] and [OII] emitters all provide good measurements of the cosmic SFRD, which are consistent with previous results from a variety of SFR tracers.

3.5 Discussion

Luminosity functions measure the density of galaxies per luminosity bin for samples of similar galaxies. Our luminosity function results are in agreement with others at similar redshifts (Figures 3.6, 3.7, 3.8, Bayliss et al. 2011; Harish et al. 2020; Hayashi et al. 2020; Khostovan et al. 2015, 2020; Ly et al. 2007, 2011; Sobral et al. 2012, 2013, 2015a), which demonstrates the homogeneity of the Universe within similar epochs.

We observe evolution with redshift for the Hα luminosity function (Figure 3.6), with an increase in luminosity at higher redshifts. This is expected when considering the range of $z \sim 0.4$ to $z \sim 0.8$ in terms of SFRD models (Figure 3.10), as this is the epoch of most rapid SFRD evolution. The cosmic SFRD is flatter at the redshifts of our [OIII] and [OII] lines ($z = 1.12$ and $z = 1.85$), which may be why we do not detect clear evolution in these luminosity functions, compared to those at similar epochs.

Our results for SFRD in Figure 3.10 are consistent with the redshift evolution of SFRD found by many surveys at a range of redshifts, therefore supporting the picture of the Universe where the star formation rate peaks at around $z = 2$ and declines in more recent times. Our results for cosmic SFRD suggest that, at least up to $z \sim 2$, previously-observed differences between studies using [OIII] and [OII] emitters and compared with other SFR tracers may be the result of systematics in luminosity function fitting, rather than from Hβ or AGN contamination, or assumptions about ionisation state or metallicity. The [OIII] emission line is not an ideal indicator for star formation rate as it can be created by AGN as well as by hot, young new stars (Zakamska et al. 2004). Our results show that the Hα, [OIII] and [OII] emission lines are good tracers of star formation and that narrowband surveys are effective at finding emission-line galaxies. Our methods of finding redshifts for the galaxies (cross-matching to catalogues and using colour-colour diagrams) are robust, which is demonstrated by the consistency between our values of SFRD in Figure 3.10 and the results we compare to, which use differing methods to ours.

Many of the differences observed between different studies could be due to different treatment of the faint-end slope of the luminosity function, including different assumptions made during fitting. It is important to note that fitted Schechter function parameters can be highly correlated (as shown in Figure 3.9), making it important to fit to a luminosity function with all three Schechter parameters free rather than fixed at an assumed value. Therefore, assuming fixed values for α can drive the overall fit of the luminosity function and lead to underestimated uncertainties on the other parameters and the resulting SFRD. Having enough deep data to freely fit α is important to accurately measure the SFRD without assumptions of the faint-end slope affecting the result. For example, had we had the deeper data over a wider area (e.g. if our wide COSMOS data had the depth of our deep GOODS-S data), we would have higher counts at the faint-end and therefore been able to better constrain the faint end slope, α.

Although many studies agree on the shape of the cosmic star formation rate density, the driving causes behind it are still unknown. Why does the star formation rate peak at $z \sim 2$? Why has star formation rate decreased until present time? There are no definitive answers, but there are many important factors. The environment of a galaxy affects its star formation rate, and in the later (more recent) Universe there is a higher prevalence of galaxy clusters. As galaxy clusters quench the star formation of their member galaxies (e.g. Gunn & Gott 1972; Stott et al. 2007, 2009) it follows that there is a decrease in cosmic SFRD in later times (e.g. Boselli & Gavazzi 2006). Also, the mass of a galaxy's dark matter halo affects how efficiently it can form stars, where this effect is thought to have some redshift dependence due to the varying densities of infalling gas. At low redshift gas inflows are typically less dense than at high redshift and are thus more susceptible to shock heating by the dark matter halo or from feedback from an AGN (e.g. Behroozi et al. 2013). As discussed in Section 1.2, low mass dark matter haloes form first meaning that the early galaxies had less massive dark matter haloes. In low mass galaxies, supernova feedback inhibits star formation, whereas in more massive galaxies AGN feedback dominate the quenching of star formation (e.g. Fabian 2012; Hopkins et al. 2014). As redshift decreases, the halo masses generally increase and the supernova feedback becomes less efficient and the star formation rate increases. Once the halo masses reach the point where AGN feedback become dominant and star formation decreases once again, with the crossover happening at $z \sim 2$. The cosmic star formation history is merely one observable piece of the Universe which contains complex underlying physics and mechanisms.

3.6 Conclusions

In this chapter we presented the first results from the Y-NBS survey, a ~ 1 deg^2 VLT/HAWK-I NB1060 study of the COSMOS field, with additional archival data in GOODS-S. We created a complete catalogue of sources with emission lines in the NB1060 filter in these fields, and identify Hα, [OIII] and [OII] emitters at $z = 0.62$, 1.12 and 1.85, respectively. We presented the corresponding luminosity functions for these sources and used them to measure the evolution of the cosmic star formation-rate density. Our main results are as follows:

1. Between the two fields, there are 461 Hα emitters (381 photometric-redshift selected, 46 spectroscopic-redshift selected and 44 colour-colour selected), 308 [OIII] emitters (279 photometric-redshift selected, 9 spectroscopic-redshift selected and 20 colour-colour selected) and 148 [OII] (137 photometric-redshift selected and 10 colour-colour selected) at $z = 0.62$, 1.12 and 1.85, respectively.

2. Our $BriK_S$ colour-colour selection, used to separate Hα emitters from [OIII] and [OII] emitters, has an Hα completeness of 97%. The additional BzK_S selection is 84% complete for [OIII] emitter and 85% complete for [OII] emitters.

3. 3% of the Hα emitters in COSMOS (GOODS-S) are AGN, which we found by cross-matching with existing X-ray and radio data (Laigle et al. 2016; Luo et al. 2017; Smolčić et al. 2017). The rate of AGN contamination in the [OIII] emitters is 2% (4%) in COSMOS (GOODS-S), and for the [OII] emitters is 7% in both COSMOS and GOODS-S.

4. We constructed luminosity functions for each emission line sample, including carrying out completeness corrections and filter profile corrections, and accounting for cosmic variance. For the Hα luminosity function at $z = 0.62$ the best-fit Schechter function parameters are $\phi^\star = 10^{-2.51^{+0.15}_{-0.19}}$ Mpc^{-3}, $L^\star = 10^{41.82^{+0.12}_{-0.09}}$ erg s^{-1} and $\alpha = -1.48^{+0.17}_{-0.17}$. The parameters for the $z = 1.12$ [OIII] luminosity function are $\phi^\star = 10^{-3.52^{+0.27}_{-0.27}}$ Mpc^{-3}, $L^\star = 10^{42.53^{+0.16}_{-0.15}}$ erg s^{-1} and $\alpha = -1.95^{+0.18}_{-0.15}$, and our best-fit Schechter function for the [OII] emitters at $z = 1.85$ has $\phi^\star = 10^{-4.08^{+0.53}_{-0.52}}$ Mpc^{-3}, $L^\star = 10^{43.01^{+0.26}_{-0.25}}$ erg s^{-1} and $\alpha = -2.43^{+0.19}_{-0.16}$.

5. The Y-NBS luminosity functions and the resulting Schechter function fits are consistent with previous results at similar redshifts, but our data extends deeper than most studies, enabling the direct measurement of the faint-end slope, α, fit simultaneously with the other parameters. As the Schechter parameters are correlated, surveys that include both wide and deep components to probe the full luminosity range are important for reliably measuring α and consequently $\phi^\star$ and $L^\star$.

6. We derived the dust-corrected star-formation rate density at $z = 0.62$, 1.12 and 1.85 from the luminosity functions of our Hα, [OIII] and [OII] emitters (accounting for AGN), which yields $\log_{10}(\rho_{\rm SFR}({\rm H}\alpha)/M_{\odot}\,{\rm yr}^{-1}\,{\rm Mpc}^{-3})$ $= -1.27^{+0.14}_{-0.12}$, $\log_{10}(\rho_{SFR}([{\rm O\textsc{iii}}])/M_{\odot}\,{\rm yr}^{-1}\,{\rm Mpc}^{-3}) = -0.95^{+0.21}_{-0.20}$ and $\log_{10}(\rho_{SFR}([{\rm O\textsc{ii}}])/M_{\odot}\,{\rm yr}^{-1}\,{\rm Mpc}^{-3}) = -0.47^{+0.20}_{-0.19}$, at $z = 0.62$, $z = 1.12$ and $z = 1.85$ respectively. These measurements are consistent with previous results, though our value for our [OII] measurement ($z = 1.85$) is marginally higher than expected. These effect are likely due our measurement of the faint end slope of the Schechter function compared with different assumptions made by past studies.

These findings from Y-NBS demonstrate the need for future surveys to simultaneously probe faint luminosities within wide areas, in order to accurately measure the faint-end slope and the “knee” of the Schechter function for different emission lines and star-formation traces across cosmic history.

Chapter 4

Y-NBS in the epoch of reionisation: the Lyα luminosity function at $z = 7.7$

Abstract

The observed luminosity function of LAEs appears to rapidly evolve at $z \gtrsim 6$ due to reionisation and the increasingly neutral intergalactic medium at higher redshifts. We present a survey of $z = 7.7$ Lyman-α emitters (LAEs) using Y-NBS, a wide-field narrowband survey in the COSMOS field. Our wide-field survey opens up a new parameter space in the study of the evolving luminosity function of LAEs: large volumes at $z \sim 8$. We use 69 pointings with VLT/HAWK-I NB1060 narrowband to cover ~ 1 deg^2 in COSMOS to a depth of 23.5 mag, which we complement with ultradeep (25.7 mag) archival data taken with the same instrument and filter in a single pointing in GOODS-S field. Both sets of observations are processed in the same way, and sources extracted and classified using the same techniques, to ensure a consistent approach in the two fields. We find no potential $z = 7.7$ LAEs in either dataset, but derive meaningful constraints on the $z = 7.7$ Lyα luminosity function. Using spectroscopically confirmed LAEs at $z = 7.7$ from Vanzella et al. 2011 and Tilvi et al. 2020 we constrain the neutral fraction of hydrogen, $\chi_{\rm HI}$, at this redshift, finding $\chi_{\rm HI} > 0.4$ at $z = 7.7$.

4.1 Introduction

The epoch of reionisation (Section 1.3) is an important era of the early Universe, during which the neutral hydrogen in the Universe was ionised, in a poorly understood process. The model of patchy reionisation suggests that bright sources were the main causes of reionisation, and that the process started around these, producing bubbles of ionised hydrogen which grew until they merged with other bubbles, until eventually the whole Universe was ionised (e.g. Mason & Gronke 2020; Matthee et al. 2015).

The neutral fraction of hydrogen (χ_{HI}) is a measure of how much reionisation has occurred in a region of the Universe at that redshift, so constraining this helps us to constrain the process of reionisation. The Lyα emission line (Section 1.2.4) is an ideal tool with which to probe the epoch of reionisation as it is a bright emission line that is observable from the ground at $z \gtrsim 5$.

This chapter uses the Y-NBS survey to search for bright and faint (due to combination of the wide COSMOS data and the deep GOODS-S data) Lyα emitters at $z = 7.7$, well into the epoch of reionisation. In Section 4.3 we constrain the $z = 7.7$ Lyα luminosity function and in Section 4.4 we use our results and those from spectroscopically confirmed LAEs at $z = 7.7$ to study and constrain the neutral fraction of hydrogen at this redshift. The findings are concluded in Section 4.6.

4.2 Sample Selection

In Chapter 2, line emitting galaxies were selected. This chapter will take that Y-NBS catalogue and identify any Lyα emitters (LAEs) that were observed at $z = 7.7$ in NB1060. This process involves spectroscopic and photometric redshifts (Section 4.2.1) and a colour-colour selection (Section 4.2.2).

4.2.1 Redshift Selection

To identify $z = 7.7$ LAEs from the sample of line emitters, we begin by searching the existing photometric and spectroscopic redshift catalogues. The spectroscopic redshift catalogues do not reach to $z = 7.7$, so no LAEs are identified spectroscopically. Photometric redshifts are less accurate, especially at higher redshifts, (e.g. Sobral et al. 2015a; Stroe & Sobral 2015), so we consider all line emitters with photometric redshifts ≥ 3 as potential $z = 7.7$ LAEs to be further examined photometrically in Section 4.2.2. We also include any line emitters without photometric and spectroscopic redshifts.

In COSMOS there are 38 sources that are detected in the z, J and H bands with $z_{\rm phot} > 3$ and 42 sources with no photometric redshift; for GOODS-S there is 1 source with $z_{\rm phot} > 3$ and 6 sources with no photometric redshift. Additionally, there are 4 sources that are undetected in at least one of these bands in COSMOS and 26 in GOODS-S (shown as black arrows at the limiting colours in Figure 4.1). All sources with photometric limits do not have photometric redshifts. These 30 sources (limits) have the potential to be $z = 7.7$ Lyα emitters and are included in the sample of 117 sources that are studied in detail in Section 4.2.2.

4.2.2 Colour-Colour Cut

We next use a colour selection on all line emitters to identify any galaxies that may be $z = 7.7$. We particularly highlight the 117 (84 from COSMOS, 33 from GOODS-S) galaxies identified in 4.2.1, which have photometric redshift grater than three or an unknown or unconstrained photometric redshift.

At $z \sim 7.7$ the Lyman break lies in the Y-band, and galaxies at this redshift can be isolated using the Lyman break technique as a z-band dropout, which can be seen in zJH colour-colour space (Bouwens et al. 2011). Figure 4.1 shows the Bouwens et al. (2011) colour selection for z-band dropout Lyman break galaxies (this is their $z \sim 7$ selection due to their broadband selection), compared with the tracks for two starburst galaxies (NGC6090 and M82) and a 13 Gyr old elliptical galaxy template from SWIRE (Polletta et al. 2007), and galaxies with varying UV β slopes from Bouwens et al. (2011). Note that no IGM is applied to the SWIRE templates or the tracks from Bouwens et al. (2011).

The tracks show that the zJH colour selection is effective at identifying high-redshift galaxies whilst also excluding lower redshift interlopers.

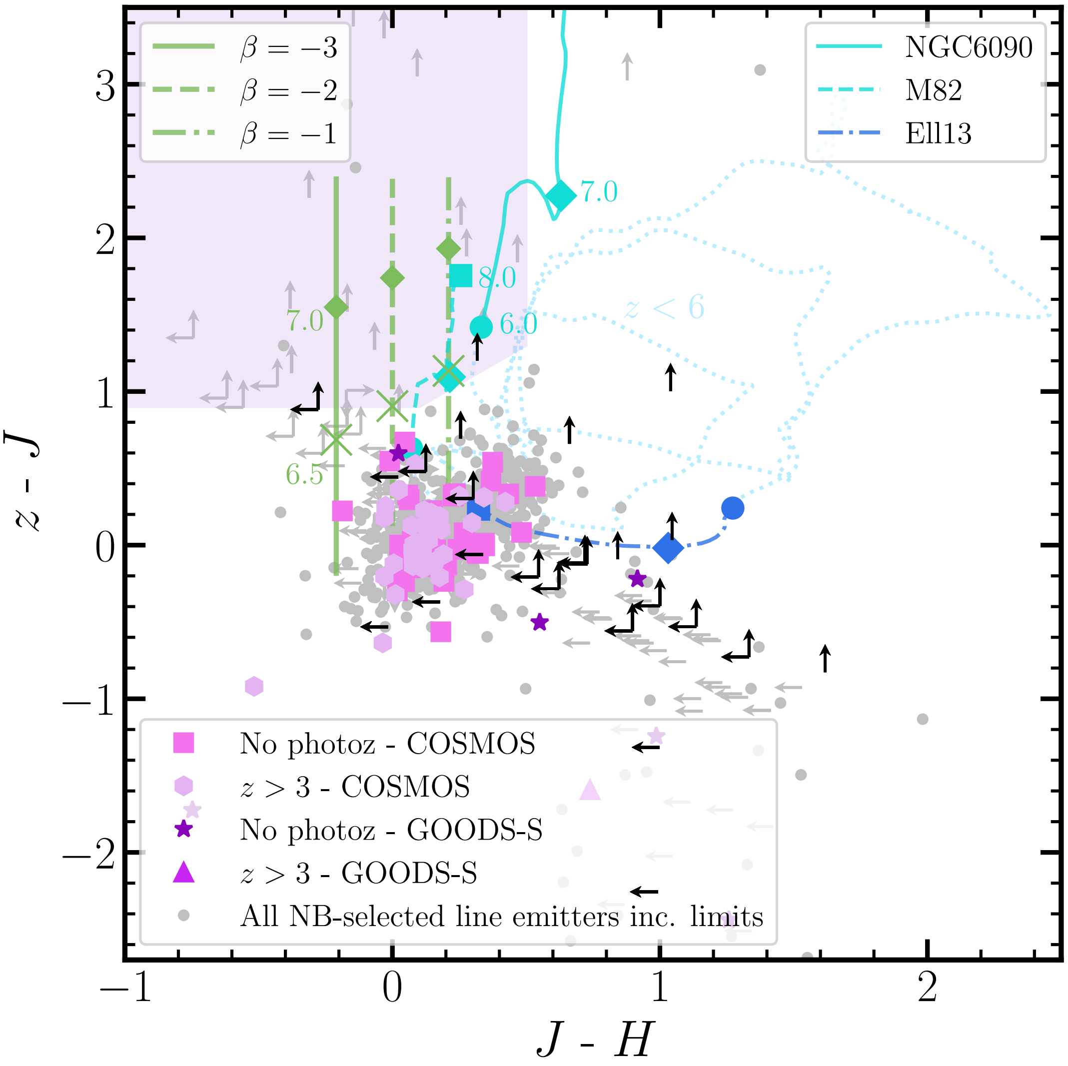

Figure 4.1: zJH colour-colour diagram with the region containing z-band dropouts, including $z = 7.7$ galaxies, highlighted (Bouwens et al. 2011; shaded region). Our COSMOS and GOODS-S samples are shown with different symbols for those with photometric redshifts ≥ 3 and those without measured redshifts (Section 4.2.1). Line emitters, in both fields, that are not detected in the H-band and/or z-bands are shown as black arrows at the limiting magnitudes and do not already have photometric redshifts. All of the candidate $z = 7.7$ sources are detected in the J-band. Grey points and arrows show all all NB-selected line emitters (regardless of any photometric or spectroscopic redshift constraints). The selection region and our Y-NBS sample are compared with the colours that the starburst galaxies, NGC6090 and M82 (cyan) and a 13 Gyr old elliptical galaxy (blue), would have if they were at $z = 6.0$ to $z = 8.0$ (Polletta et al. 2007); these tracks are continued to lower redshifts (grey; dotted) to demonstrate that the selection region excludes lower redshift interlopers. Starburst galaxies with varying UV slopes (β) at $z \sim 6{-}8$ are also shown (Bouwens et al. 2011).

In Figure 4.1 the potential high-redshift line emitters are shown in shades of pink and purple, separated into those from COSMOS and GOODS-S that have photometric redshifts ≥ 3 and those without an existing photometric redshift (usually due to insufficient photometric detection). All of these galaxies are detected in the J-band. In the z and H-bands, 3σ limits are used for galaxies that are fainter than the detection limit or with a measured photometric uncertainty ≥ 0.78 (corresponding to the 3σ limit).

As Figure 4.1 shows, none of the 117 Y-NBS galaxies with photometric redshift greater than three or undetermined are detected in z, J and H in the region of colour-colour space indicative of z-band dropout galaxies. There is one object that is not detected in z and one that is undetected in both the z and H-bands and that are in or near the selection region when the appropriate limiting magnitudes are considered. The source that is undetected in only the z-band (with $J - H \sim 0.3$, $z - J \gtrsim 1.2$) is in GOODS-S and does not have a counterpart in the redshift catalogue (Hsu et al. 2014). The other potential $z \sim 7.7$ galaxy (with $J - H \lesssim -0.2$, $z - J \gtrsim 0.85$) is also in GOODS-S and has a photometric redshift of $z_{\rm phot} = 3.25^{+0.09}_{-0.10}$ (Hsu et al. 2014). To further assess whether these NB1060 line emitters could be $z = 7.7$ LAEs, we examine the VIMOS U-band observations of GOODS-S (Nonino et al. 2009).

Both objects are detected in the U-band, meaning that they cannot be at $z \gtrsim 3$ due to the redshifting of the Lyman limit (rest frame 912 Å). Whilst there are other sources that are not detected in z and/or H and that have colour limits that are consistent with them being in the z-band dropout selection region, the colours of these galaxies are poorly constrained and we therefore conservatively exclude from further analyses.

We carry out additional checks for $z = 7.7$ LAEs by including all of the NB1060-selected line emitters in Figure 4.1, again applying the conditions for limits described above. These are shown in grey and include 21 sources within the lilac selection region. To check whether these could be viable $z = 7.7$ LAEs, we check the imaging and photometry of these sources in broadbands that cover restframe wavelengths below the observed Lyman limit at $z = 7.7$ (i.e. U-, V- and B-bands). If any of these sources are detected in the U-, B- or V-bands then they cannot be $z = 7.7$ LAEs as these bands would cover wavelengths shortward of the Lyman break for $z = 7.7$ LAEs. Of the 21 sources in the selection region, all but two have detections in the B-band and therefore must be at $z \lesssim 4$ as suggested by their photometric redshifts. These two remaining sources are both in the GOODS-S field and one source has a detection in VIMOS U-band imaging (Nonino et al. 2009) and the other has a detection in the MUSYC V-band data (Cardamone et al. 2010; Taylor et al. 2009). Therefore, these line emitters are also precluded from being $z \sim 7.7$ LAEs. Thus, we do not identify any $z = 7.7$ LAEs in Y-NBS in COSMOS or GOODS-S. The remainder of our analyses are based on non-detections and limits to the volume density of $z = 7.7$ LAEs in our wide area survey.

4.3 Lyα Luminosity Function

As shown in Section 4.2.2 we do not find any $z = 7.7$ Lyα emitters in Y-NBS. We next convert this non-detection into upper limits on the $z = 7.7$ Lyα luminosity function, using the luminosity range probed by the data and the observed volume. The upper limit on the number density (ϕ) is calculated as $\phi = \text{counts}/(\text{volume} \times \text{bin width})$, where counts ≤ 1 for the upper limit.

The volume observed with the NB1060 filter at $z = 7.7$ is calculated by converting the wavelength coverage of NB1060 (Kissler-Patig et al. 2008) to the redshift to which we are sensitive to Lyα in the narrowband filter. The AstroPy cosmology package (Astropy Collaboration et al. 2013, 2018, 2022) is used to determine the volume of the Universe covered by this redshift range, which is 8,612 Mpc^3 for the GOODS-S pointing, and 492,131 Mpc^3 in COSMOS. In Section 3.3.3.3, we discussed the filter profile correction and how NB1060 does not have the perfect top-hat profile that is assumed for this volume calculation, but there are instead different volumes for faint luminosities and bright luminosities. Faint sources can only be detected toward the centre of the narrowband filter as transmission is high, making a smaller volume available for faint sources. Alternatively, a bright source can be observed across a wider range of wavelengths within the narrowband filter, even when transmission is lower, meaning a larger volume is probed for bright sources. This can be corrected for usually (Section

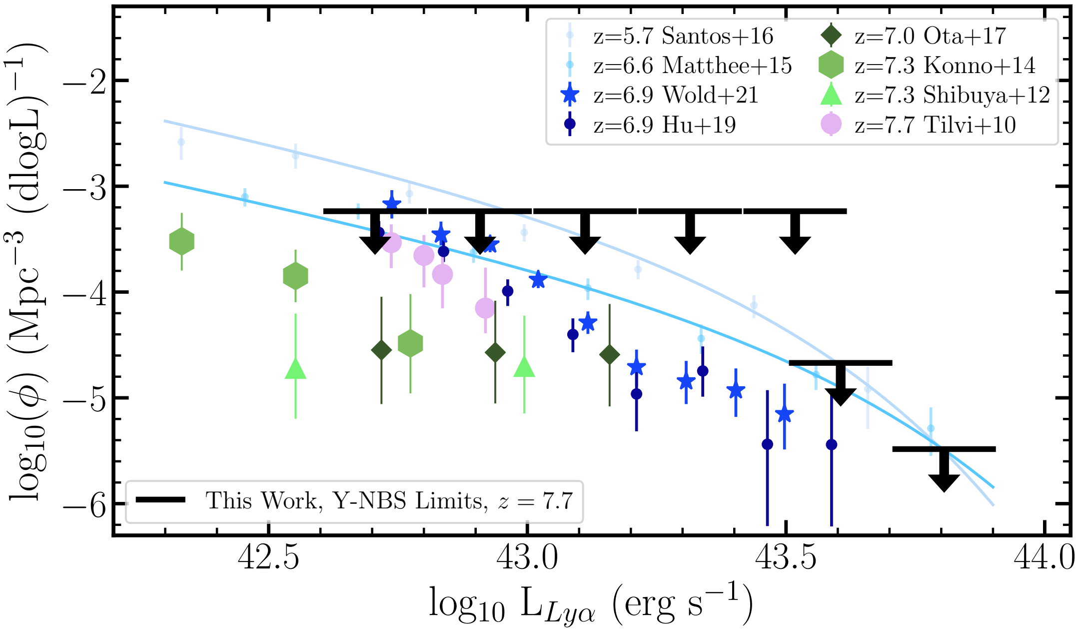

Figure 4.2: The high-redshift Lyα luminosity function showing the upper limits from our Y-NBS analyses at $z = 7.7$, compared with previous studies at $z = 5.7 - 7.7$ (Hu et al. 2019; Konno et al. 2014; Matthee et al. 2015; Ota et al. 2017; Santos et al. 2016; Shibuya et al. 2012; Tilvi et al. 2010; Wold et al. 2021). The deepest Y-NBS limit is derived from the GOODS-S data and bins of 0.2dex are used to show the luminosity range that GOODS-S could have found a $z = 7.7$ LAE. The final two limits (with the brightest luminosities) are from the regions in COSMOS with deep and shallow NB1060 observations (Section 4.2); the Y-NBS results are consistent with other studies at $z = 7.7$ (Tilvi et al. 2010) and highlight the need for wide and deep surveys to identify these rare sources.

3.3.3.3) but as we have not observed any LAEs in these data we cannot complete this corrected.

In determining the luminosity limits, we consider GOODS-S and COSMOS separately as they probe to significantly different depths. The limiting luminosity for each field is calculated as $L = 4\pi d_L f_{\rm line}$ where L is the limiting luminosity, d_L is the luminosity distance to $z = 7.7$ and $f_{\rm line}$ is the Lyα line flux to which we are sensitive. The limiting line flux is calculated separately for each field by binning the fluxes of all the line emitters in bins of 0.05 dex. The faintest complete bin is that at which the raw counts peak and turn over and lower limit of this bin is deemed to be the limiting flux for that field. The limiting luminosity for GOODS-S is log(Lyα) = 42.6 erg s^{-1}. The upper limit for number density for GOODS-S is calculated using the GOODS-S volume, the GOODS-S limiting magnitude and a bin width of 0.2dex, giving up the leftmost black line and arrow. The bins are repeated until they reach the limiting luminosity of the COSMOS data is reached, which is log(Lyα) = 43.5 erg s^{-1} for the deep pointings. The row of five upper limits represents the upper limit for where a LAE could be observed in GOODS-S. The second to last arrow on the right is calculated using the volumes of both COSMOS deep and GOODS-S and has a bin width of 0.2dex. The limiting magnitude of COSMOS Shallow is log(Lyα) = 43.7 erg s^{-1}, and this rightmost limit is calculated with a bin width of 0.2dex and the volume of GOODS-S and COSMOS (deep and shallow pointings) combined.

In each region, the lower end of the luminosity limit is calculated as $L = 4\pi d_L f_{\rm line}$ where L is the limiting luminosity, d_L is the luminosity distance to $z = 7.7$ and $f_{\rm line}$ is the Lyα line flux to which we are sensitive.

Figure 4.2 shows the limits on the $z = 7.7$ Lyα luminosity function from our Y-NBS observations, compared to previous studies at $z = 5.7 - 7.7$ (Hu et al. 2019; Konno et al. 2014; Matthee et al. 2015; Ota et al. 2017; Santos et al. 2016; Shibuya et al. 2012; Tilvi et al. 2010, 2020; Vanzella et al. 2011; Wold et al. 2021). As shown by Figure 4.2 at $z = 7.0 - 7.7$ intermediate luminosities ($\log(L_{\rm Ly\alpha}/{\rm erg\,s^{-1}}) = 43.0 - 43.5$) are poorly probed by existing studies, which tend to be either deep and narrow or wide and shallow. The approach from Y-NBS aimed to scrutinise this intermediate luminosity regime by using the combination of GOODS-S and COSMOS data, though the absence of $z = 7.7$ LAEs in our survey restricts our ability to draw conclusions about the $z = 7.7$ LAE population at these intermediate luminosities. Our limits on the $z = 7.7$ Lyα luminosity function from Y-NBS are consistent with expectations from existing $z = 7.7$ observations (Tilvi et al. 2010, 2020; Vanzella et al. 2011), though Y-NBS covers wider areas than these works.

It has previously been established that there is minimal evolution in the Lyα luminosity function from $z \sim 2 - 6$ (e.g. Sobral et al. 2018) and, as Figure 4.2 shows, there is a drop in the luminosity function beyond $z \sim 6$. Since the Lyα luminosity function does not evolve at lower redshifts, this is interpreted as being due to the higher fraction of neutral hydrogen during the epoch of reionisation, which renders fainter LAEs no longer visible at high redshift.

4.4 Constraining the Neutral Fraction of Hydrogen at $z = 7.7$

Constraining the neutral fraction of hydrogen during the epoch of reionisation is key for understanding how reionisation developed. In order for Lyα photons to redshift sufficiently to escape through the neutral hydrogen without being absorbed, a galaxy needs to be inside a sufficiently large ionised bubble (Mason & Gronke 2020; Matthee et al. 2015), which enables LAEs to be used to trace the neutral fraction of hydrogen and hence the reionisation of the IGM. The first step in measuring the neutral fraction of hydrogen from the $z = 7.7$ Lyα luminosity function is to measure the transmission of the IGM at $z = 7.7$, denoted as $T^{\mathrm{IGM}}_{7.7}$.

4.4.1 Evolving IGM Transmission

We follow the method presented in Hu et al. (2019) to calculate the ratio of transmission of the intergalactic medium (IGM) at $z = 7.7$ and $z = 5.7$, which is given by

$$\frac{T^{\mathrm{IGM}}_{7.7}}{T^{\mathrm{IGM}}_{5.7}} = \frac{\rho^{\mathrm{Ly}\alpha}_{7.7} / \rho^{\mathrm{Ly}\alpha}_{5.7}}{\rho^{\mathrm{UV}}_{7.7} / \rho^{\mathrm{UV}}_{5.7}} \tag{4.1}$$

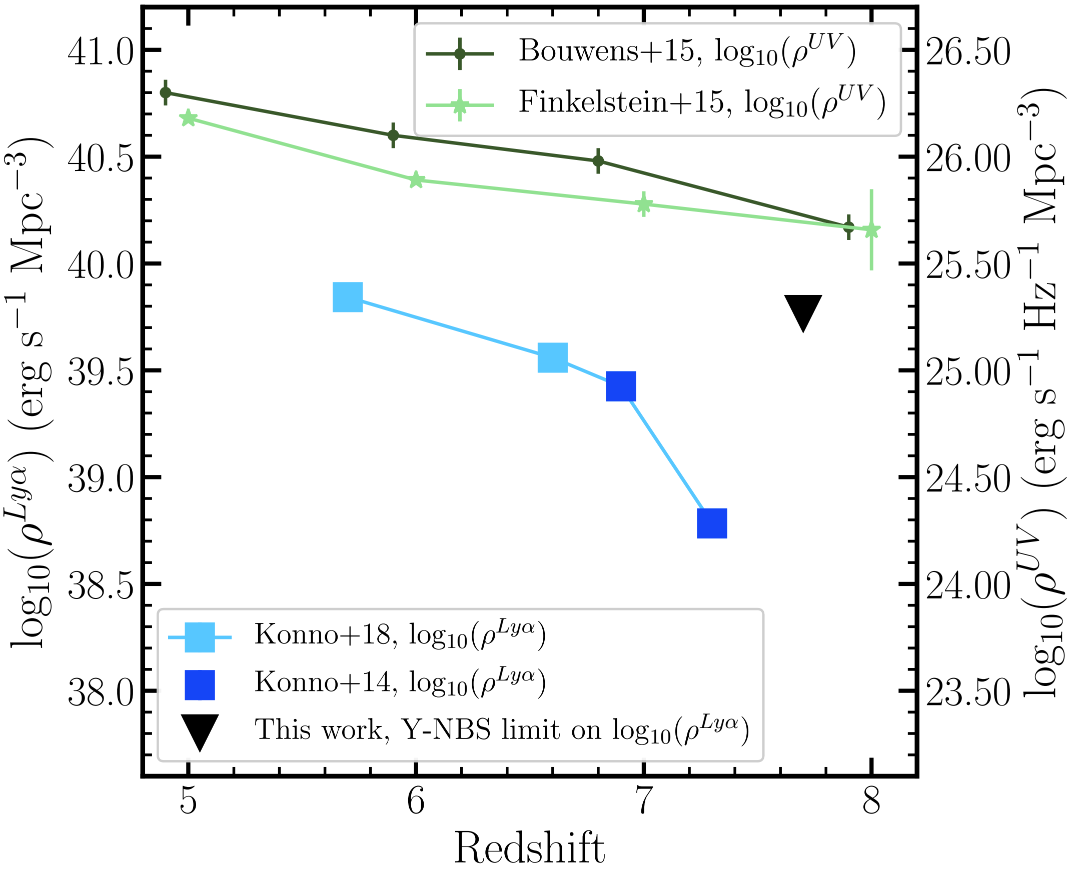

Figure 4.3: The evolution of Lyα luminosity density (left axis, bottom legend) and UV photon density (right axis, top legend) with redshift. We follow the methods from Hu et al. (2019) to determine the upper limit on the Lyα luminosity density at $z = 7.7$ from Y-NBS and the limits it has placed on the $z = 7.7$ Lyα luminosity function. Our measurements at $z = 7.7$ are compared with the $z = 5.7$ to 7.3 results from Konno et al. (2014) and Konno et al. (2018) (uncertainties are not available for these data points). The upper limit on the $z = 7.7$ Lyα luminosity density from Y-NBS (black) is consistent but higher than would be expected if extrapolating from the lower redshift measurements (Konno et al. 2014, 2018).

where $\rho_{7.7}^{\mathrm{Ly}\alpha}$ $\left(\rho_{7.7}^{\mathrm{Ly}\alpha}\right)$ is the Lyα luminosity density at $z = 7.7$ ($z = 5.7$) measured in $\mathrm{erg\,s^{-1}\,Mpc^{-3}}$, and $\rho_{7.7}^{\mathrm{UV}}$ $\left(\rho_{5.7}^{\mathrm{UV}}\right)$ is the UV photon luminosity density at $z = 7.7$ ($z = 5.7$) measured in erg $\mathrm{s^{-1}\,Hz^{-1}\,Mpc^{-3}}$. Equation 4.1 thus compares that evolution of the observed UV and Lyα luminosity density at two redshifts and implicitly assumes that the relative properties of the interstellar medium and stellar populations at $z = 5.7$ and $z = 7.7$ do not evolve. We choose $z = 5.7$ as the comparison redshift because it is the highest redshift for which Lyα and UV luminosity functions are well measured but without showing evidence for ongoing reionisation.

At $z = 7.7$ the Lyα luminosity density is calculated from integrating a Schechter function fit to the measured Lyα luminosity functions. We consider our Y-NBS limit on the $z = 7.7$ Lyα luminosity function for this calculation. As this is a limit we cannot fit a Schechter function to it so instead we assume that there is no evolution in the shape from the $z = 6.6$ luminosity function and scale for the luminosity density. For the $z = 6.6$ luminosity function we use the Schechter function parametrisation from Matthee et al. (2015) ($\log(\phi^\star/\mathrm{Mpc^{-3}}) = -4.40^{+0.10}_{-0.13}$, $\log(L^*/\mathrm{erg\,s^{-1}}) = 43.42^{+0.10}_{-0.07}$ with α fixed to -2.0) and scale to the $z = 7.7$ limits using Markov Chain Monte Carlo (MCMC) fitting and changing only $\phi^\star$. For the deepest Y-NBS limit we determine that $\phi^\star < 10^{-4.27}$ $\mathrm{Mpc^{-3}}$.

To measure $\rho_{7.7}^{\mathrm{Ly}\alpha}$ we next integrate the Schechter function in the range $\log(L_{\mathrm{Ly}\alpha}/\mathrm{erg\,s^{-1}}) = 42.4 - 44$, following the integration limits from Hu et al. (2019). This gives $\log(\rho_{7.7}^{\mathrm{Ly}\alpha}/\mathrm{erg\,s^{-1}\,Mpc^{-3}}) < 39.77$ for the Y-NBS limit. For the $z = 5.7$ Lyα luminosity density we use $\rho_{5.7}^{\mathrm{Ly}\alpha} = 39.54$ $\mathrm{erg\,s^{-1}\,Mpc^{-3}}$ from Hu et al. (2019) (originally from Konno et al. 2014; uncertainties are not given). Figure 4.3 shows this Lyα luminosity density compared with measurements at lower redshift (Bouwens et al. 2015; Finkelstein et al. 2015; Hu et al. 2019; Konno et al. 2014, 2018). Our limit for the Lyα luminosity density is consistent with the lower redshift results, although it is less constraining than the $z \sim 7$ results.

For the UV photon luminosity densities we use the results from Bouwens et al. (2015) and Finkelstein et al. (2015) for galaxies at $z \sim$ 4–8 selected with *Hubble Space Telescope* photometry. These studies do not provide measurements at precisely $z = 5.7$ and $z = 7.7$ (Figure 4.3), so we linearly interpolate between the nearest data points to obtain estimates at the required redshifts. This yields

$\rho^{\rm UV}_{7.7}/\rho^{\rm UV}_{5.7} = 0.39 \pm 0.08$ using Bouwens et al. (2015) and $\rho^{\rm UV}_{7.7}/\rho^{\rm UV}_{5.7} = 0.52 \pm 0.18$ for Finkelstein et al. (2015).

Combining the limit on the Lyα luminosity density from Y-NBS with the UV luminosity density measurements gives an upper limit on the IGM transmission of $T^{\rm IGM}_{7.7}/T^{\rm IGM}_{5.7} < 1.61$ and $T^{\rm IGM}_{7.7}/T^{\rm IGM}_{5.7} < 2.17$ using Bouwens et al. (2015) and Finkelstein et al. (2015), respectively. The IGM transmission is unlikely to be higher at $z = 7.7$ than at $z = 5.7$ and therefore these limits effectively imply $T^{\rm IGM}_{7.7}/T^{\rm IGM}_{5.7} < 1$.

4.4.2 Neutral Fraction of Hydrogen at $z = 7.7$

The constraints on IGM transmission derived in Section 4.4.1 are necessarily imprecise, due to both the uncertainties on the integration of the $z = 7.7$ Lyα luminosity functions and the uncertainties on the UV photon luminosity densities. This method of constraining the neutral fraction of hydrogen in the IGM also assumes that the properties of the interstellar medium and the stellar population do not evolve between $z = 7.7$ and $z = 5.7$. To account for these factors, in all cases we consider the measured transmission ratio to be the upper limit on the true transmission of the $z = 7.7$ IGM, which leads to lower limits on the fraction of neutral hydrogen in the IGM, $\chi_{\rm HI}$.

To convert the measured limit on IGM transmission into a limit on the neutral fraction of hydrogen we use the analytic relationship derived by Santos (2004). We primarily consider the model in which the Lyα line velocity is offset from the systemic redshift by 360 $\rm km\,s^{-1}$, as observed in some high-redshift galaxies (e.g. Shapley et al. 2003). We note that lower Lyα line offsets would lead to a lower inferred neutral hydrogen fraction but that a 0 $\rm km\,s^{-1}$ velocity offset is inconsistent with our measurements of the IGM transmission (see Santos 2004 Figure 25).

Since the Y-NBS data cannot constrain the IGM transmission at $z = 7.7$ to be any different to that at $z = 5.7$ then these measurements only provides a hydrogen neutral fraction limit of $\chi_{\rm HI} > 0$, i.e. reionisation is effectively unconstrained by the Y-NBS limits on the $z = 7.7$ luminosity function.

We note that observational estimates of the neutral fraction of hydrogen from galaxies are rarely well-constrained and have not previously been explored at $z = 7.7$. Studies of the Lyα luminosity function at $z = 7.0$ and 7.3 find $\chi_{\text{HI}} < 0.63$ and $\chi_{\text{HI}} = 0.3 - 0.8$ (Konno et al. 2014; Ota et al. 2010), which are consistent with our measurements. Hu et al. (2019) used the same method at $z = 7.0$ to obtain $\chi_{\text{HI}} = 0.25 - 0.5$, which is consistent with our results, although the lower end of this range may point towards redshift evolution when compared with our data. Recently, Jones et al. (2023) compared the observed rest-frame Lyα equivalent width of $z \sim 7$ sources to the model by Pentericci et al. (2014) and obtained $\chi_{\text{HI}} \sim 0.5 - 0.9$, which is in line with existing measurements. Thus, our constraints of $\chi_{\text{HI}} > 0.40$ and $\chi_{\text{HI}} > 0.56$ at $z = 7.7$ (depending on assumptions about the UV luminosity density) are consistent with previous measurements of the hydrogen neutral fraction at lower redshifts, and they may hint of some evolution at $z > 7$, which is consistent with the process of reionisation. Future, unbiased, wide narrowband surveys that do find LAEs at $z = 7.7$ will be able to better constrain the neutral fraction of hydrogen with this method.

4.5 Discussion

At $z = 7.7$, existing studies present a mix of spectroscopically-confirmed LAEs (e.g. (Tilvi et al. 2020)) and photometric candidates (e.g. (Tilvi et al. 2010)). In Tilvi et al. (2010), they find four candidate LAEs within at volume of $1.4 \times 10^4 \text{Mpc}^3$ using a narrowband survey at $z = 7.7$. They say that these results would require spectroscopic follow-up to draw conclusions about reionisation, but if they were confirmed they would show that the Lyα luminosity functions does not evolve at $z > 6$ but any observed evolution is due to LAEs being obscured by the neutral hydrogen.

The results of Tilvi et al. (2020) are based on spectroscopic follow-up of a deep and wide narrowband survey (0.72 deg^2, 5σ detection limit $= 6\times10^{-18}$ erg cm^{-2} s^{-1}). The three LAEs confirmed by Tilvi et al. (2020) are physically close to each other (< 0.7 Mpc separation), with the brightest source having created a ~ 1.02 Mpc ionised bubble, which significantly overlaps with the bubbles created by the other sources. Thus, Tilvi et al. (2020) provides evidence of patchy reionisation at $z = 7.7$.

We were not able to observe any $z = 7.7$ LAEs in Y-NBS because our area (0.8 deg^2) was not wide enough to observe a rarer, bright LAE and our data was not deep enough to find any fainter LAEs. However, our non-detection results are consistent with the hypothesis of patchy reionisation and it not yet being complete at $z = 7.7$, agreeing with results from other LAE surveys, but also with results studying the CMB (e.g. Planck Collaboration et al. 2020). To be able to follow in the footsteps of Tilvi et al. (2020) and confirm narrowband-selected $z = 7.7$ with spectroscopic follow-up, we would need deeper narrowband data as well as deep auxiliary broadband data. This would allow us to observe faint LAEs. Increasing the area of the survey would give us a higher chance of observing one of these rare $z = 7.7$ sources. Once such sources are observed, analysis similar to that of Tilvi et al. (2020) would uncover the properties of the ionised bubbles carved out by these sources, such as radius, and give us a greater insight into LAEs as sources of reionisation. Similar to the findings of Matthee et al. (2015) (see Section 1.3), it would be interesting to see whether finding bright LAEs within a large ionisation bubble would also allow us to observe fainter LAEs within the same bubble. This would support the idea of patchy reionisation; the brightest sources dominate reionisation.

With a large enough sample of $z = 7.7$ LAEs, one could plot a luminosity function, especially if the LAEs were of a range of luminosities. This would be useful when considering the evolution of the Lyα luminosity function and the impact that reionisation has on the observability of sources.

Recent claims from Maiolino et al. (2023) say that JWST has observed evidence for Population III stars (see Section 1.2.1). They observed the bright galaxy GN-z11 ($z = 10.6$) with JWST/NIRSpec and found a $> 5\sigma$ detection of the [HeII] emission and no metal lines in a clump near to GN-z11, suggesting that this could be a detection of Population III stars. Alternatively, this could be a foreground detection of a different emission line. If this is evidence for Population III stars then further study into them with JWST could shed light on how they contribute to reionisation. It would also mean that it is possible to spectroscopically follow-up LAEs at $z = 7.7$ with JWST and potentially study their stellar populations in detail. Being able to compare the properties of galaxies at $z = 10.6$ and $z = 7.7$ would help to uncover what is happening in a rapidly evolving epoch of the Universe.

4.6 Conclusions

This chapter presents an analysis of the high-redshift Universe using the Y-NBS survey, which observed ~ 1 deg^2 of the COSMOS field with the NB1060 narrowband filter on VLT/HAWK-I. Combining these wide-field data with deep archival VLT/HAWK-I NB1060 observations in GOODS-S (Clément et al. 2012) we searched for Lyα emitters at $z = 7.7$. Our main results are as follows:

- To search for $z = 7.7$ Lyα emitters we followed Bouwens et al. (2011) and constructed a zJH colour-colour diagram for the line emitters selected in Chapter 2 that have photometric redshifts $z_{\rm phot} > 3.0$ or no measured redshift. Two sources have photometric limits that place them in or near the z-band dropout region, but these are ruled out as $z = 7.7$ LAEs on the basis of the detection of U-band counterparts.
- Using the absence of $z = 7.7$ LAEs in our survey, we place upper limits on the $z = 7.7$ Lyα luminosity function, which are in agreement with the previous results at similar redshifts
- The Y-NBS data place upper limits on the evolution of the IGM transmission of $T^{\rm IGM}_{7.7}/T^{\rm IGM}_{5.7} < 2.17$ and $T^{\rm IGM}_{7.7}/T^{\rm IGM}_{5.7} < 1.61$ using Bouwens et al. (2015) and Finkelstein et al. (2015) measurements of the evolution of the UV photon density at $z \sim 7.7$, respectively.
- We place a limit on the neutral fraction of hydrogen at $z = 7.7$ to be greater than 0, but we highlight that future wide, deep, narrowband surveys will be able to constrain this important value in the future.

This study demonstrates the need for wide and deep Lyα surveys at $z > 7$ to constrain the evolution of the observed Lyα luminosity function in the epoch of reionisation.

Chapter 5

Conclusions and Future Work

This thesis aims to probe the nature of line-emitting galaxies through a range of redshifts, from the epoch of reionisation, with Lyα emitters at $z = 7.7$, to more local line emitting galaxies at $z = 0.6 - 1.8$, using the survey, Y-NBS. This section summarises the results and discusses possible future work.

Y-NBS is a survey conducted with VLT/HAWK-I using the near-infrared narrowband NB1060 filter, which covers ~ 0.8 deg^2 of the COSMOS field and is supplemented with archive VLT/HAWK-I data of the GOODS-S field (0.014 deg^2). We fully reduced the data with a dedicated pipeline and generated catalogues of line emitting sources (Chapter 2) to study the evolution of the cosmic star formation rate density at $z < 1.85$ (Chapter 3) and to probe reionisation at $z = 7.7$ (Chapter 4).

From the catalogue of line emitters we selected samples of Hα, [OIII] and [OII] emitters, at $z = 0.62$, $z = 1.12$ and $z = 1.85$ respectively, using spectroscopic redshift, photometric redshifts and colour-colour selection methods. This yields a sample of 461 Hα emitters, 308 [OIII] emitters and 148 [OII] emitters across both the COSMOS and GOODS-S data. With these samples, we constructed luminosity functions for each line and fitted a Schechter function with all three parameters free. Our results are consistent with previous results at similar redshifts (e.g. Bayliss et al. 2011; Harish et al. 2020; Hayashi et al. 2020; Khostovan et al. 2015, 2020; Ly et al. 2007, 2011; Sobral et al. 2012, 2013, 2015a), but we probe deeper or cover a wider range of luminosities than many other studies. As the Schechter parameters are correlated, covering both the faint and bright ends simultaneously is necessary to get an accurate picture of the luminosity function, and the parameters – especially the faint-end slope, α. Our values for the faint-end slope are $\alpha = -1.48^{+0.17}_{-0.17}$, $-1.95^{+0.18}_{-0.15}$ and $-2.43^{+0.19}_{-0.16}$ respectively for Hα, [OIII] and [OII] emitters, at $z = 0.62$, $z = 1.12$ and $z = 1.85$ respectively. The robustness of the fits also affects the derived star formation rate density.

The star formation rate density per line was calculated, providing values of $\log_{10}(\rho_{\rm SFR}({\rm H}\alpha)/M_\odot\,{\rm yr}^{-1}\,{\rm Mpc}^{-3}) = -1.27^{+0.14}_{-0.12}$, $\log_{10}(\rho_{SFR}([{\rm O\,III}])/M_\odot\,{\rm yr}^{-1}\,{\rm Mpc}^{-3})$ $= -0.95^{+0.21}_{-0.20}$ and $\log_{10}(\rho_{SFR}([{\rm O\,II}])/M_\odot\,{\rm yr}^{-1}\,{\rm Mpc}^{-3}) = -0.47^{+0.20}_{-0.19}$, at $z = 0.62$, $z = 1.12$ and $z = 1.85$ respectively. These values are consistent with literature results, although our [OII] measurement at $z = 1.85$ is slightly higher than expected (by ~ 0.3 dex), which is likely due to our measurement of a steeper faint-end slope compared to other studies.

These results highlight the need for future surveys to probe deep *and* wide within the same regions of the sky to help overcome cosmic variance and to accurately measure both the faint- and bright-ends of the luminosity functions. This would also minimise the uncertainties on the luminosity functions and derived evolution of the cosmic star formation rate density.

Using the sample of narrowband-selected line emitters, we also used a colour-colour selection in zJH space to search for $z = 7.7$ LAEs which will be z-band dropouts, though none are found. However, we placed limits on the $z = 7.7$ Lyα luminosity function, which are consistent with previous photometric studies at $z = 7.7$ (Tilvi et al. 2010) and extrapolation from lower redshift surveys (e.g. Hu et al. 2019; Konno et al. 2014; Matthee et al. 2015; Ota et al. 2017; Santos et al. 2016; Shibuya et al. 2012; Wold et al. 2021). These limits will be useful for planning future, wide, deep narrowband surveys.

Following methods from Hu et al. (2019), we put a limit on the neutral fraction of hydrogen at $z = 7.7$. First, we calculated the ratio of transmission through the intergalactic medium at $z = 7.7$ compared with $z = 5.7$, which requires UV luminosity density at both redshifts, for which we used values from Bouwens et al. (2015) and Finkelstein et al. (2015). We also required the Lyα luminosity density, which we calculated by integrating the $z = 7.7$ luminosity function for our Y-NBS limits. Using the ratio of transmission for the four cases, we used the analytic relationship from Santos (2004) to convert transmission to the neutral fraction of hydrogen at $z = 7.7$. We constrained the neutral fraction of hydrogen at $z = 7.7$ to be $\chi_{\rm HI} > 0$, but we highlight that future wide, deep, narrowband surveys could constrain this value further. Looking at results at slightly lower redshifts hint that evolution in the neutral fraction continues to at least $z = 7.7$, which is expected as reionisation is ongoing at these redshifts. However we are not able to constrain the neutral fraction at $z = 7.7$ enough to confirm any evolution. Therefore, further studies are needed to more precisely measure the $z = 7.7$ neutral fraction.

This work highlights the need for further wide and deep Lyα surveys at $z = 7.7$ to constrain and understand the evolution in the luminosity function and to help our understanding of how the process of reionisation develops.

5.1 Future Work

Although this work with Y-NBS has helped our understanding of the $z = 7.7$ Universe and the evolution of star-forming galaxies at lower redshifts, there are still open questions surrounding these topics. Possible future research is presented in this section.

5.1.1 Hα up to $z \sim 6$

With ground-based telescopes, the Hα line can only be observed up to $z \sim 2$ (Geach et al. 2008; Sobral et al. 2013), which has limited its use as a probe of the evolution of star formation rate density (SFRD). *JWST* unlocks the ability to observe Hα up to $z \sim 6$, meaning that it can be used as a self-consistent probe of SFRD up to the end of epoch of reionisation, which would improve our estimates of SFRD and help us to understand the star-formation history of the Universe. Also, a wider redshift range of observations of the Hα samples would help us to understand how the Hα luminosity function evolves. For example, the *JWST* program JELS (*JWST* Emission Line Survey, PI: Philip Best) is a narrowband survey conducted with NIRCam with specific goals to find $z \sim 6$ Hα emitters.

5.1.2 Follow-up of Low Redshift Sources

This work, especially Chapter 3, predominantly considered the statistical properties of samples of sources at lower redshifts. However, studying these on an individual level would also prove interesting: What morphology do they have? Do they have AGN? Answering questions such as these would help us to understand the role of AGN and environment on shaping galaxy evolution, as well as understanding the mechanisms driving star formation and their contributions to the cosmic star formation rate density. Potential instruments include the upcoming spectrograph on the VLT, MOONS.

5.1.3 The Faint-end Turn-off Point of Luminosity Functions

The deepest data used in this work (covering GOODS-S) has a 3σ depth of 25.7 mag in NB1060, which was a result of 31 hours of exposure time with HAWK-I. Despite this depth, we do not find any evidence for the faint-end turn-off in any of the luminosity functions we studied. The faint-end turn-off is the point when the number density of increasingly faint galaxies no longer increases but instead drops off. Surveys have not yet found this point for high redshift galaxies due to sensitivity limits, but upcoming facilities will probe further towards this goal. The Extremely Large Telescope could potentially do this, likely with the MICADO imager as it will have broadband filters from I to K, as well as narrowbands. Just 2 hours of exposure time in the J-band on MICADO would provide a 3σ limiting magnitude of 26.0 mag[1]. Observing to great depths to specifically find faint sources requires a field of view in which there are no sources bright enough to become over exposed and saturated, as well as observing to sufficient depth to detect statistically-meaningful numbers of faint sources.

5.1.4 Further Searches for Lyα Emitters at $z = 7.7$ and Beyond

In Chapter 4, Figure 4.2 we explored the $z > 6$ Lyα luminosity function including data points from $z = 7.7$ studies. There is a dearth of data in the

---

[1] Calculated using the ELT Imaging Exposure Time Calculator: `https://www.eso.org/observing/etc/bin/gen/form?INS.NAME=ELT+INS.MODE=swimaging`.

$\log_{10}(\mathrm{L_{Ly\alpha}}/\ \mathrm{erg\,s^{-1}}) = 43.0 - 43.5$ range, which is possible to cover with current telescopes; though it would require more exposure time. Surveying this mid-luminosity region and finding sources here would help to link the bright and faint ends to fully understand the number densities of Lyα emitters at $z = 7.7$ and the development of reionisation at this point in the history of the Universe.

A wider and deeper survey with HAWK-I would likely find these $z = 7.7$ LAEs that we did not find. Y-NBS covers ~ 0.8 deg^2 of the 2.2 deg^2 COSMOS field and we combined this with the small area GOODS-S field (0.014 deg^2), so extending Y-NBS with more data across multiple fields would be beneficial. Also, as discussed in Chapter 3, it would be favourable to have the deepest data within the same region as the wider data, in order to understand density fluctuations within the region. Covering multiple fields would help to overcome cosmic variance, and choosing fields with deep broadband coverage is also key. Some examples of suitable fields include: ECDFS, UDS and the rest of the COSMOS field.

Many studies (e.g. Hu et al. 2019; Konno et al. 2014; Ota et al. 2017; Shibuya et al. 2012; Tilvi et al. 2010, 2020; Vanzella et al. 2011; Wold et al. 2021) have searched for LAEs at $z \gtrsim 7$ and the results are still inconclusive, but at $z > 8$ there are far fewer known sources. Reionisation will be less complete at this redshift, reionised bubbles will be smaller and the neutral fraction of hydrogen will be higher – but these exact values are unknown and unconstrained, so investigating them would prove fruitful.

5.1.5 Multi-wavelength Follow-up of High Redshift Sources

Although understanding the population of $z = 7.7$ Lyα sources in terms of the luminosity function is important, understanding the individual sources and their internal properties is important as well.

For example, as discussed in Section 1.2 with the example of multi-wavelength analysis of CR7 at $z = 6.6$, *HST* can determine the mass of the galaxy or its constituent clumps, ALMA can observe lines such as [CII] to confirm the redshift of the galaxy and VLT/X-SHOOTER can observe other interesting emission like HeII and NV. Similar analysis for $z = 7.7$ and higher sources would help us to understand the nature of galaxies in the early Universe – are they often clumpy?

What sort of emission do they have? Such complex systems in the early Universe require analysis in many wavelengths from multiple instruments in order to begin to understand them. A deeper understanding of the dynamics of these high redshift galaxies in the early Universe would help us to study the epoch of reionisation and to see how they contribute to reionisation.

Appendix A

Appendices

A.1 Table of Observations

NB1060 VLT/HAWK-I observations conducted for the Y-NBS survey in the COSMOS field. A total of 69 pointings, numbered from P19 to P90 (Field ID, see Figure 2.1), to cover a total area of $0.8\,\mathrm{deg}^2$. The single VLT/HAWK-I pointing for GOODS-S has an integration time of 31.9 hours. For more details regarding the GOODS-S data, see Clément et al. (2012).

Table A.1: Table of observations using VLT/HAWK-I NB1060 in the COSMOS field.

Field ID	R.A. (J2000)	Dec. (J2000)	Integration time (s/pixel)	Observation Date	Seeing (arcsec)
P19	09 58 51.1	01 41 28.6	600	12 January 2018	0.63
P20	09 58 51.0	01 48 56.5	600	17 January 2018	0.73
P21	09 58 50.9	01 56 24.1	600	17 January 2018	0.71
P22	09 58 50.9	02 03 49.6	600	7 March 2017	0.60
P23	09 58 51.0	02 11 16.6	2700	20 January 2018	0.61
P24	09 58 51.0	02 18 44.9	2800	22 February 2018	0.71
P25	09 58 51.0	02 26 10.1	2700	4 January 2017	0.67
P26	09 58 51.1	02 33 44.6	2900	5 January 2017	0.65
P27	09 58 50.9	02 41 05.9	2800	21 January 2018	0.76
P28	09 59 20.8	01 41 31.3	600	28 November 2017	0.83
P29	09 59 20.8	01 48 59.0	600	13 December 2017	0.59
P30	09 59 20.9	01 56 24.0	600	26 January 2017	0.69
P31	09 59 20.8	02 03 48.9	600	26 January 2017	0.75
P32	09 59 20.9	02 11 17.2	2700	6 January 2017	0.61
P33	09 59 20.9	02 18 43.3	2700	6 January 2017	0.73
P34	09 59 20.9	02 26 12.8	2800	26 January 2017	0.80
P35	09 59 20.7	02 33 38.1	2400	18 March 2017	0.96
P36	09 59 20.8	02 41 05.4	2800	3 April 2017	0.62
P37	09 59 50.4	01 41 30.4	600	28 November 2017	0.63
P38	09 59 50.7	01 48 55.9	600	21 June 2017	0.89
P39	09 59 50.6	01 56 23.1	600	7 March 2017	0.72
P40	09 59 50.2	02 03 51.3	600	21 December 2017	0.62
P41	09 59 50.5	02 11 19.5	600	21 December 2017	0.56
P42	09 59 50.5	02 18 46.3	600	18 December 2017	0.67
P43	09 59 50.4	02 26 12.1	600	18 December 2017	0.67
P44	09 59 50.7	02 33 36.8	600	27 December 2017	0.68
P45	09 59 50.5	02 41 08.3	600	28 December 2017	0.71
P46	10 00 20.5	01 41 29.4	2800	7 March 2017	0.58
P47	10 00 20.5	01 48 59.4	3000	28 April 2017	0.52
P48	10 00 20.5	01 56 25.7	2800	24 January 2018	0.68
P49	10 00 20.3	02 03 50.3	2800	29 November 2017	0.72
P50	10 00 20.5	02 11 18.7	2800	15 December 2017	0.78
P51	10 00 20.5	02 18 44.0	2800	28 April 2017	0.77

Table A.2: Above, continued

Field ID	R.A. (J2000)	Dec. (J2000)	Integration time (s/pixel)	Observation Date	Seeing (arcsec)
P52	10 00 20.3	02 26 11.0	2800	15 December 2017	0.80
P53	10 00 20.1	02 33 39.6	600	7 January 2017	0.77
P54	10 00 20.2	02 41 04.5	600	4 January 2017	0.80
P55	10 00 50.1	01 41 28.5	2800	18 December 2017	0.75
P56	10 00 50.1	01 48 57.6	2900	24 December 2017	0.66
P57	10 00 50.0	01 56 24.9	3500	22 February 2018	0.70
P58	10 00 50.2	02 03 52.1	2800	9 January 2018	0.64
P59	10 00 50.2	02 11 15.9	2700	9 January 2018	0.59
P60	10 00 50.1	02 18 43.7	2700	11 January 2018	0.64
P61	10 00 50.2	02 26 13.0	2700	6 January 2017	0.74
P62	10 00 50.4	02 33 39.3	600	28 December 2017	0.74
P63	10 00 50.1	02 41 6.0	600	29 December 2017	0.59
P64	10 01 20.1	01 41 31.2	600	29 December 2017	0.52
P65	10 01 19.9	01 48 55.0	2800	12 January 2018	0.89
P66	10 01 19.9	01 56 25.4	600	7 March 2017	0.69
P67	10 01 20.2	02 03 50.6	600	7 March 2017	0.73
P68	10 01 19.9	02 11 18.4	600	7 March 2017	0.79
P69	10 01 20.1	02 18 41.7	600	29 December 2017	0.61
P70	10 01 19.8	02 26 12.9	600	9 January 2018	0.79
P71	10 01 20.0	02 33 41.0	1200	26 January 2017	0.64
P72	10 01 19.9	02 41 4.7	600	17 December 2017	0.80
P73	10 01 49.8	01 41 30.8	600	7 March 2017	0.61
P74	10 01 50.2	01 48 56.0	600	28 November 2017	0.67
P75	10 01 49.7	01 56 22.6	600	13 December 2017	0.66
P76	10 01 49.5	02 03 50.2	600	19 January 2018	0.88
P77	10 01 49.9	02 11 18.8	600	19 January 2018	0.69
P78	10 01 49.9	02 18 43.9	600	19 January 2018	0.78
P79	10 01 49.7	02 26 13.3	2700	17 January 2018	0.77
P80	10 01 49.8	02 33 40.4	2700	20 January 2018	0.71
P81	10 01 49.9	02 41 06.1	2800	24 January 2018	0.66
P85	10 02 19.6	02 03 52.9	600	19 January 2018	0.83
P86	10 02 19.7	02 11 16.5	600	20 January 2018	0.66
P87	10 02 18.2	02 19 08.4	600	8 March 2018	0.75
P88	10 02 18.3	02 26 34.0	2700	22 January 2018	0.70
P89	10 02 19.6	02 33 36.8	2800	23 January 2018	0.70
P90	10 02 19.9	02 41 2.1	2800	23 January 2018	0.61

A.2 BB1060 Colour Correction

A.2.1 Full BB1060 Derivation

This section presents the full derivation of the equation for the synthetic broadband magnitude centred at the centre of NB1060, named BB1060 (i.e. Equation 2.1). This magnitude is derived such that it only contains the flux due to the continuum of a source, and not any line emission contribution. This step is a necessary colour correction because NB1060 is not centred in the Y-band and otherwise sources with a steep continuum could be mistakenly selected as line emitters. The narrowband filter, NB1060, lies within the Y-band and the next broadbands with increasing wavelength are J and H (see Figure 2.4). If there is an emission line in NB1060, then we assume the J and H bands contain only the continuum and that the continuum follows a power law in this limited wavelength range.

There are three key equations for this derivation. The first relates AB magnitude (m_{AB}, mag) to the flux density in frequency (f_ν, $\mathrm{erg\,s^{-1}\,cm^{-2}\,Hz^{-1}}$):

$$f_\nu = 10^{-0.4(m_{\rm AB}+48.8)} \tag{A.1}$$

The second key equation relates flux density in wavelength (f_λ, $\mathrm{erg\,s^{-1}\,cm^{-2}\,\AA^{-1}}$) to flux density in frequency, using c, the speed of light in $\mathrm{\AA\,s^{-1}}$, and λ_{cen}, the central wavelength of the filter in Å:

$$f_\lambda = \frac{f_\nu c}{\lambda_{cen}^2} \tag{A.2}$$

The final key equation relates the flux density in two adjacent filters for a source with continuum emission that follows a power-law with $f_\lambda \propto \lambda^\beta$. In this case:

$$f_{\lambda_1} = f_{\lambda_2}\left(\frac{\lambda_1}{\lambda_2}\right)^\beta \tag{A.3}$$

The first step is to derive β, the power law exponent, in terms of magnitude.

Rearranging Eq. A.3 gives:

$$\beta = \frac{\log_{10}\left(f_{\lambda_1}\right) - \log_{10}\left(f_{\lambda_2}\right)}{\log_{10}\left(\frac{\lambda_1}{\lambda_2}\right)} \tag{A.4}$$

The numerator of this question can simplified using Eqs. A.1 and A.2 to give:

$$\log_{10}\left(f_{\lambda_1}\right) - \log_{10}\left(f_{\lambda_2}\right) = -0.4\left(m_1 - m_2\right) - 2\log_{10}\left(\frac{\lambda_1}{\lambda_2}\right) \tag{A.5}$$

Substituting this back into Eq. A.4 for β and replacing m_1 and m_2 with J and H, respectively, gives:

$$\beta = \frac{-0.4\left(J - H\right)}{\log_{10}\left(\frac{\lambda_J}{\lambda_H}\right)} - 2 \tag{A.6}$$

We next define a synthetic broadband magnitude, BB1060, which is centred at the centre of NB1060, but composed purely of continuum:

$$\mathrm{BB1060} = -2.5\log_{10}\left(f_{\nu_{\mathrm{NB}}}\right) - 48.6 \tag{A.7}$$

Substituting Eq. A.2 into the definition for BB1060, and simplifying gives:

$$\mathrm{BB1060} = -2.5\log_{10}\left(\frac{\lambda_{\mathrm{NB}}^2}{c}\right) - 2.5\log_{10}\left(f_{\lambda_{\mathrm{NB}}}\right) - 48.6 \tag{A.8}$$

Using Eq. A.3 with filter 1 as NB1060 and filter 2 as J, and substituting into Eq. A.8 gives:

$$\begin{aligned}\mathrm{BB1060} = &-2.5\log_{10}\left(\frac{\lambda_{\mathrm{NB}}^2}{c}\right) - 2.5\beta\log_{10}\left(\frac{\lambda_{\mathrm{NB}}}{\lambda_J}\right) \\ &-2.5\log_{10}\left(f_{\lambda_J}\right) - 48.6\end{aligned} \tag{A.9}$$

Next, we substitute in Eq. A.6 into the second term above to get:

$$\begin{aligned} \mathrm{BB1060} = &- 2.5\log_{10}\left(\frac{\lambda_{\mathrm{NB}}^2}{c}\right) - 2.5\log_{10}\left(f_{\lambda_J}\right) - 48.6 \\ &+ (J-H)\left(\frac{\log_{10}\frac{\lambda_{\mathrm{NB}}}{\lambda_J}}{\log_{10}\frac{\lambda_J}{\lambda_H}}\right) + 5\log_{10}\left(\frac{\lambda_{\mathrm{NB}}}{\lambda_J}\right) \end{aligned} \tag{A.10}$$

and using Eq. A.2 in the second term to get:

$$\begin{aligned} \mathrm{BB1060} = &- 2.5\log_{10}\left(\frac{\lambda_{\mathrm{NB}}^2}{c}\right) - 2.5\log_{10}\left(f_{\nu_J}\right) \\ &- 2.5\log_{10}\left(\frac{c}{\lambda_J^2}\right) - 48.6 \\ &+ (J-H)\left(\frac{\log_{10}\frac{\lambda_{\mathrm{NB}}}{\lambda_J}}{\log_{10}\frac{\lambda_J}{\lambda_H}}\right) + 5\log_{10}\left(\frac{\lambda_{\mathrm{NB}}}{\lambda_J}\right) \end{aligned} \tag{A.11}$$

Noticing that the terms with c can cancel and using $J = -2.5\log_{10}\left(f_{\nu_J}\right) - 48.6$ this simplifies to:

$$\begin{aligned} \mathrm{BB1060} = -2.5\log_{10}\left(\frac{\lambda_{\mathrm{NB}}^2}{\lambda_J^2}\right) + J + (J-H)\left(\frac{\log_{10}\frac{\lambda_{\mathrm{NB}}}{\lambda_J}}{\log_{10}\frac{\lambda_J}{\lambda_H}}\right) \\ + 5\log_{10}\left(\frac{\lambda_{\mathrm{NB}}}{\lambda_J}\right) \end{aligned} \tag{A.12}$$

where the first and final terms cancel each other, leaving the final form of the equation, as used in Section 2.6.1, which is the same equation as Equation 2.1:

$$\mathrm{BB1060} = J + (J-H)\left(\frac{\log_{10}\frac{\lambda_{\mathrm{NB}}}{\lambda_J}}{\log_{10}\frac{\lambda_J}{\lambda_H}}\right) \tag{A.13}$$

A.2.2 Colour Correction Testing

We carried out tests on various colour corrections to find the best way to extract the most accurate narrowband excess from our data. We found that calculating a synthetic broadband magnitude, BB1060, centred at the centre of NB1060, and

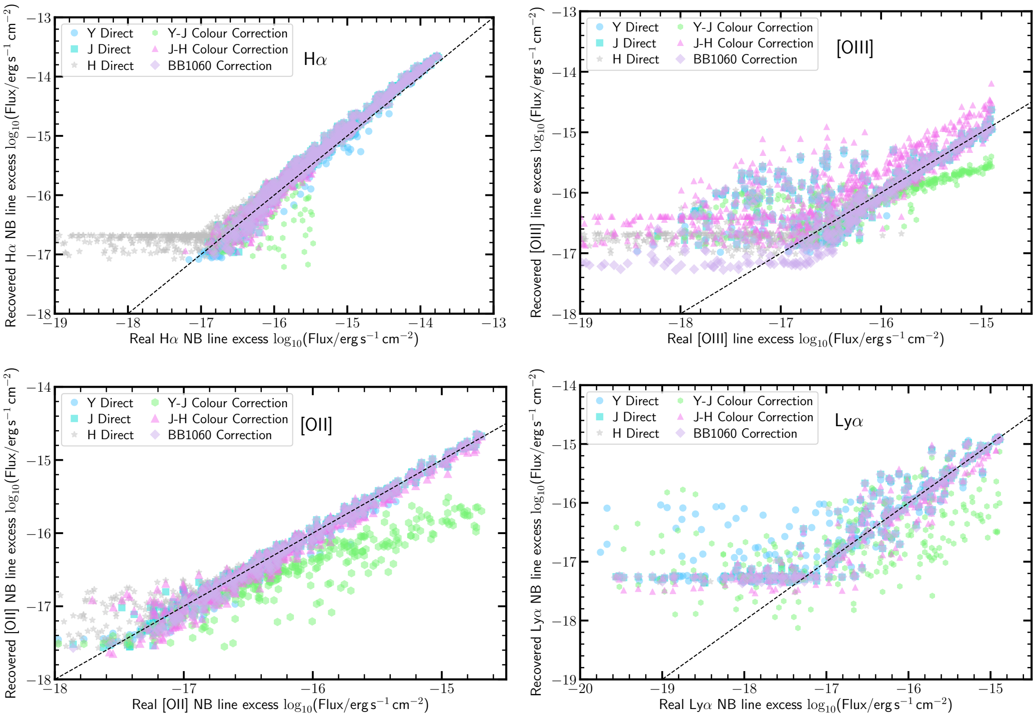

Figure A.1: Real NB excess flux verses recovered NB excess flux for the colour corrections for simulated Hα, [OIII], [OII] and Lyα lines. The colour corrections we tested were: directly using the Y, J and H-bands, a $Y-J$ colour correction, a $J-H$ colour correction and our BB1060 synthetic broadband magnitude, which are plotted in different symbols as shown in the legend. The dashed line shows the one to one relation between real and recovered narrowband excess. We can see minimal scatter around this line for the BB1060 colour correction, and it yields the lowest median offset and scatter when compared to other colour corrections. Horizontal trends for faint objects are due to the simulated line flux being too faint to recover.

derived using the J and H bands (BB1060 $= J + (J - H)\left(\frac{\log_{10}\frac{\lambda_{\rm NB}}{\lambda_J}}{\log_{10}\frac{\lambda_J}{\lambda_H}}\right)$) performed the best in testing. To test the colour corrections we simulated Hα, [OIII], [OII] and Lyα lines, convolved them through the filters (NB1060, Y, J and H), calculated the colour correction and calculated the NB excess flux that would be observed for each.

The tested colour corrections were: Y direct, J direct, H direct, $Y-J$ colour correction, $J-H$ colour correction and the BB1060 colour correction. For Y, J, and H direct the NB excess was calculated as the NB1060 magnitude minus the appropriate broadband, with no corrections made. The $Y-J$ and $J-H$ colour correction essentially ensures that sources without an emission line have zero NB excess, and it follows the methods used in Sobral et al. (2018). For these corrections we have recalibrated the narrowband magnitude (NB) to mean that on average sources that are not line emitters have zero narrowband excess (e.g. BB - NB$\sim$ 0, where BB is Y or J and NB is the corrected NB1060 magnitude) no matter their continuum colour ($Y-J$ or $J-H$). To do this we find the colour dependence of NB$_0$ - Y (NB$_0$ - J) on $Y-J$ ($J-H$), where NB$_0$ is the initial, uncorrected narrowband magnitude. This gives the parameters m_1 (m_2) and b_1 (b_2) that define the straight line:

$$\mathrm{BB} - \mathrm{NB} = m_1 \times (Y - J) + b_1 \tag{A.14}$$

$$\mathrm{BB} - \mathrm{NB} = m_2 \times (J - H) + b_2 \tag{A.15}$$

We can now calculate the corrected narrowband magnitude, NB:

$$\mathrm{NB} = \mathrm{NB}_0 + (m_1 \times (Y - J) + b_1) \tag{A.16}$$

$$\mathrm{NB} = \mathrm{NB}_0 + (m_2 \times (J - H) + b_2) \tag{A.17}$$

NB is the corrected NB1060 magnitude, NB$_0$ is the initial NB1060 magnitude, Y, J and H and the Y, J and H-band magnitudes and m_1, m_2, b_1 and b_2 are the parameters that link the dependence of colour excess on continuum colour.

The calculation for BB1060 is given in Section 2.6.1 and Appendix A.2.1.

Figure A.1 shows the recovered NB excess flux verses the real NB excess flux per line for all six tested colour corrections. For each colour correction, the median offset was calculated by finding the difference for each simulated source between the real NB excess flux and the recovered NB excess flux (both in log form) and calculating the median of these values. The standard deviation of these values gives the scatter of the colour correction. The Hα panel shows that $Y - J$ does not recover the NB excess well, with a green cloud of sources appearing significantly below the one-to-one line. This $Y - J$ correction performs poorly for all four emission lines in all four plots with the green points being significantly offset from the one to one line. For the Hα plot, the H direct colour correction yields the highest median offset and scatter from the all combinations tested, with a median offset of -0.157 and a scatter of 0.492, compared to BB1060 having a smaller median offset (-0.090) and scatter (0.107).

The top-right panel of Figure A.1, shows the results for the [OIII] colour corrections. We can see that the $J - H$ colour correction is offset above from the one-to-one line (pink triangle) and has a scatter of 0.686. For the [OII] plot, all but the $Y - J$ colour correction perform well, with the green hexagons lying below the one-to-one line, but the H direct method yields the highest scatter with 0.337 and BB1060 has the lowest scatter of 0.073. The plot for Lyα demonstrates that the Y direct method performs the worst, with a scatter of 0.789. BB1060 has the lowest median offset of 0.0002 and the lowest scatter of 0.404.

The two best overall methods for recovering the real NB excess flux are this BB1060 and J direct, with BB1060 having the lowest scatter for [OII] and Lyα, and J direct having the lowest scatter for Hα and [OIII]. BB1060 performs the best overall at recovering the real NB excess flux as it yields the smallest median offset Hα, [OIII], and Lyα, whereas J direct only has the smallest median offset for [OII]. Therefore, BB1060 is used for the colour correction in Section 2.6.1.

A.3 Maximum Excess Calculation

To calculate a maximum physical colour, or excess, that a line emitting galaxy could have, we calculate the maximum Y- band magnitude that a NB1060 mag

= 15 source would have, as this is our bright limit for NB1060 magnitudes before sources become saturated.

Usually, our excess is calculated from BB1060, which uses J- and H-band magnitudes, see Eq. 2.1. However, in theory, we could have a source where there is no flux in the J and H bands, and there is pure emission line flux in with no continuum contribution in NB1060 – hence we use the Y-band. From our cuts, the brightest possible line emitter has a NB1060 magnitude of 15, so we convert this into a line flux as follows:

$$f_{\mathrm{line}} = \Delta\lambda_{\mathrm{NB}} \times \frac{c}{\lambda^2_{\mathrm{cen,NB}}} \times 10^{-0.4(\mathrm{NB1060}+48.60)} \tag{A.18}$$

where f_{line} is the line flux, $\Delta\lambda_{\mathrm{NB}}$ is the width of the NB1060 filter, c is the speed of light, $\lambda_{\mathrm{cen,NB}}$ is the central wavelength of the NB1060 filter. We can then convert this back into a Y band magnitude:

$$Y = -2.5\log\left(\frac{f_{\mathrm{line}} \times \lambda^2_{\mathrm{cen,Y}}}{\Delta}\lambda_{\mathrm{Y}} \times c\right) - 48.6 \tag{A.19}$$

For a NB1060 magnitude of 15 that is purely from the emission line, we calculate a Y band magnitude of 17.57, making our maximum excess 2.57. We apply this cut to our colour magnitude diagrams in Section 2.6.2 and Figure 2.6.

References

Abel T., Bryan G. L., Norman M. L., 2002, Science, 295, 93

Arnouts S., et al., 2002, MNRAS, 329, 355

Astropy Collaboration et al., 2013, A&A, 558, A33

Astropy Collaboration et al., 2018, AJ, 156, 123

Astropy Collaboration et al., 2022, apj, 935, 167

Barkana R., Loeb A., 2001, , 349, 125

Barkana R., Loeb A., 2004, The Astrophysical Journal, 609, 474

Bayliss K. D., McMahon R. G., Venemans B. P., Ryan-Weber E. V., Lewis J. R., 2011, MNRAS, 413, 2883

Bayliss K. D., McMahon R. G., Venemans B. P., Banerji M., Lewis J. R., 2012, MNRAS, 426, 2178

Behroozi P. S., Marchesini D., Wechsler R. H., Muzzin A., Papovich C., Stefanon M., 2013, ApJL, 777, L10

Bertin E., 2006, in Gabriel C., Arviset C., Ponz D., Enrique S., eds, Astronomical Society of the Pacific Conference Series Vol. 351, Astronomical Data Analysis Software and Systems XV. p. 112

Bertin E., 2010, SWarp: Resampling and Co-adding FITS Images Together (ascl:1010.068)

Bertin E., Arnouts S., 1996, AAPS, 117, 393

Bolzonella M., Miralles J. M., Pelló R., 2000, A&A, 363, 476

Boselli A., Gavazzi G., 2006, , 118, 517

Bouwens R. J., et al., 2011, ApJ, 737, 90

Bouwens R. J., et al., 2014, ApJ, 793, 115

Bouwens R. J., et al., 2015, ApJ, 803, 34

Bouwens R. J., et al., 2021, AJ, 162, 47

Bower R. G., Benson A. J., Malbon R., Helly J. C., Frenk C. S., Baugh C. M., Cole S., Lacey C. G., 2006, MNRAS, 370, 645

Bowler R. A. A., et al., 2012, MNRAS, 426, 2772

Bowler R. A. A., et al., 2014, MNRAS, 440, 2810

Bowler R. A. A., Dunlop J. S., McLure R. J., McLeod D. J., 2017a, MNRAS, 466, 3612

Bowler R. A. A., Dunlop J. S., McLure R. J., McLeod D. J., 2017b, MNRAS, 466, 3612

Bradley L., et al., 2020, astropy/photutils: 1.0.0, doi:10.5281/zenodo.4044744, `https://doi.org/10.5281/zenodo.4044744`

Brammer G. B., van Dokkum P. G., Coppi P., 2008, ApJ, 686, 1503

Bromm V., Larson R. B., 2004, Annual Review of Astron and Astrophys, 42, 79

Bromm V., Yoshida N., 2011, Annual Review of Astronomy and Astrophysics, 49, 373

Brusa M., et al., 2010, ApJ, 716, 348

Bunker A. J., Warren S. J., Hewett P. C., Clements D. L., 1995, MNRAS, 273, 513

Bunker A. J., et al., 2010, MNRAS, 409, 855

Bunker A. J., et al., 2023, A&A, 677, A88

Byler N., Dalcanton J. J., Conroy C., Johnson B. D., 2017, ApJ, 840, 44

Capak P., et al., 2007, ApJS, 172, 99

Cappelluti N., et al., 2007, ApJS, 172, 341

Cardamone C. N., et al., 2010, The Astrophysical Journal Supplement Series, 189, 270–285

Carniani S., et al., 2018, MNRAS, 478, 1170

Casali M., et al., 2006, in McLean I. S., Iye M., eds, Society of Photo-Optical Instrumentation Engineers (SPIE) Conference Series Vol. 6269, Society of Photo-Optical Instrumentation Engineers (SPIE) Conference Series. p. 62690W, doi:10.1117/12.670150

Castellano M., et al., 2010, A&A, 511, A20

Cedrés B., et al., 2021, A&A, 649, A73

Cen R., Haiman Z., 2000, ApJL, 542, L75

Ciardullo R., et al., 2013, ApJ, 769, 83

Civano F., et al., 2016, ApJ, 819, 62

Clément B., et al., 2012, A&A, 538, A66

Comparat J., et al., 2015, A&A, 575, A40

Couchman H. M. P., Rees M. J., 1986, MNRAS, 221, 53

Coughlin A., et al., 2018, ApJ, 858, 96

Cucciati O., et al., 2012, A&A, 539, A31

Cui Y., Xiang Y., Rong K., Feris R., Cao L., 2014, in IEEE Winter Conference on Applications of Computer Vision. pp 213–219, doi:10.1109/WACV.2014.6836098

Daddi E., Cimatti A., Renzini A., Fontana A., Mignoli M., Pozzetti L., Tozzi P., Zamorani G., 2004, ApJ, 617, 746

Davis M., Efstathiou G., Frenk C. S., White S. D. M., 1985, ApJ, 292, 371

Dayal P., Ferrara A., 2018, , 780, 1

De Lucia G., Springel V., White S. D. M., Croton D., Kauffmann G., 2006, MNRAS, 366, 499

Drake A. B., et al., 2013, MNRAS, 433, 796

Dunlop J. S., McLure R. J., Robertson B. E., Ellis R. S., Stark D. P., Cirasuolo M., de Ravel L., 2012, MNRAS, 420, 901

Fabian A. C., 2012, Annual Review of Astron and Astrophys, 50, 455

Fan X., et al., 2006, ApJ, 132, 117

Ferrero I., Navarro J. F., Abadi M. G., Benavides J. A., Mast D., 2021, A&A, 648, A124

Finkelstein S. L., et al., 2015, ApJ, 810, 71

Finkelstein S. L., et al., 2023, arXiv e-prints, p. arXiv:2311.04279

Fontana A., et al., 2014, A&A, 570, A11

Fujita S. S., et al., 2003, ApJL, 586, L115

Fukugita M., Kawasaki M., 1994, MNRAS, 269, 563

Gallego J., Zamorano J., Aragon-Salamanca A., Rego M., 1995, ApJL, 455, L1

Geach J. E., Smail I., Best P. N., Kurk J., Casali M., Ivison R. J., Coppin K., 2008, MNRAS, 388, 1473

Gómez-Guijarro C., Gallego J., Villar V., Rodríguez-Muñoz L., Clément B., Cuby J.-G., 2016, A&A, 591, A151

Gunn J. E., Gott J. Richard I., 1972, ApJ, 176, 1

Guth A. H., 1981, Phys. Rev. D, 23, 347

Harish S., et al., 2020, ApJ, 892, 30

Hasinger G., Miyaji T., Schmidt M., 2005, A&A, 441, 417

Hasinger G., et al., 2007, ApJS, 172, 29

Hasinger G., et al., 2018, ApJ, 858, 77

Hayashi M., Sobral D., Best P. N., Smail I., Kodama T., 2013, MNRAS, 430, 1042

Hayashi M., et al., 2018, , 70, S17

Hayashi M., et al., 2020, , 72, 86

Hibon P., et al., 2010, A&A, 515, A97

Hippelein H., et al., 2003, A&A, 402, 65

Hopkins A. M., Beacom J. F., 2006, ApJ, 651, 142

Hopkins P. F., Kereš D., Oñorbe J., Faucher-Giguère C.-A., Quataert E., Murray N., Bullock J. S., 2014, MNRAS, 445, 581

Hsu L.-T., et al., 2014, ApJ, 796, 60

Hu E. M., Cowie L. L., Barger A. J., Capak P., Kakazu Y., Trouille L., 2010, ApJ, 725, 394

Hu E. M., Cowie L. L., Songaila A., Barger A. J., Rosenwasser B., Wold I., 2016, preprint, (`arXiv:1606.03526`)

Hu W., et al., 2019, ApJ, 886, 90

Hubble E. P., 1926, ApJ, 64, 321

Ilbert O., et al., 2006, A&A, 457, 841

Ilbert O., Capak P., et al., 2009, ApJ, 690, 1236

Ilbert O., et al., 2013, A&A, 556, A55

Jiang L., et al., 2017, The Astrophysical Journal, 846, 134

Jones G. C., et al., 2017, The Astrophysical Journal, 850, 180

Jones G. C., et al., 2023, arXiv e-prints, p. arXiv:2306.02471

Karim A., et al., 2011, ApJ, 730, 61

Kennicutt Jr. R. C., 1998, ARAA, 36, 189

Khostovan A. A., Sobral D., Mobasher B., Best P. N., Smail I., Stott J. P., Hemmati S., Nayyeri H., 2015, MNRAS, 452, 3948

Khostovan A., et al., 2018, MNRAS, submitted,

Khostovan A. A., et al., 2020, MNRAS, 493, 3966

Kissler-Patig M., et al., 2008, A&A, 491, 941

Konno A., et al., 2014, ApJ, 797, 16

Konno A., et al., 2017, preprint, (`arXiv:1705.01222`)

Konno A., et al., 2018, , 70, S16

Krug H. B., et al., 2012, ApJ, 745, 122

Laigle C., et al., 2016, ApJS, 224, 24

Lilly S. J., Le Fevre O., Hammer F., Crampton D., 1996, ApJL, 460, L1

Lumbreras-Calle A., et al., 2022, A&A, 668, A60

Luo B., et al., 2017, ApJS, 228, 2

Ly C., et al., 2007, ApJ, 657, 738

Ly C., Lee J. C., Dale D. A., Momcheva I., Salim S., Staudaher S., Moore C. A., Finn R., 2011, ApJ, 726, 109

Madau P., Dickinson M., 2014, ARAA, 52, 415

Madau P., Haardt F., Rees M. J., 1999, ApJ, 514, 648

Maiolino R., et al., 2015, MNRAS, 452, 54

Maiolino R., et al., 2023, arXiv e-prints, p. arXiv:2306.00953

Malhotra S., Rhoads J. E., 2004, ApJL, 617, L5

Marchesi S., et al., 2016, ApJ, 817, 34

Mason C. A., Gronke M., 2020, arXiv e-prints, p. arXiv:2004.13065

Mason C. A., Treu T., Dijkstra M., Mesinger A., Trenti M., Pentericci L., de Barros S., Vanzella E., 2018, The Astrophysical Journal, 856, 2

Matthee J. J. A., et al., 2014, MNRAS, 440, 2375

Matthee J., Sobral D., Santos S., Röttgering H., Darvish B., Mobasher B., 2015, MNRAS, 451, 400

Matthee J., Sobral D., Best P., Smail I., Bian F., Darvish B., Röttgering H., Fan X., 2017a, MNRAS, 471, 629

Matthee J., Sobral D., Darvish B., Santos S., Mobasher B., Paulino-Afonso A., Röttgering H., Alegre L., 2017b, MNRAS, 472, 772

Matthee J., et al., 2017c, The Astrophysical Journal, 851, 145

McCracken H. J., et al., 2012, A&A, 544, A156

Morioka T., Nakajima A., Taniguchi Y., Shioya Y., Murayama T., Sasaki S. S., 2008, , 60, 1219

Moster B. P., Somerville R. S., Newman J. A., Rix H.-W., 2011, ApJ, 731, 113

Muzzin A., et al., 2013, ApJS, 206, 8

Nagaraj G., Ciardullo R., Bowman W. P., Lawson A., Gronwall C., 2023, ApJ, 943, 5

Nakamura F., Umemura M., 2001, ApJ, 548, 19

Narayanan D., et al., 2021, ApJS, 252, 12

Navarro J. F., Frenk C. S., White S. D. M., 1996, ApJ, 462, 563

Nonino M., et al., 2009, ApJS, 183, 244

Oh S., et al., 2020, MNRAS, 495, 4638

Oke J. B., Gunn J. E., 1983, ApJ, 266, 713

Osterbrock D. E., Ferland G. J., 2006, Astrophysics of gaseous nebulae and active galactic nuclei

Ostriker J. P., Gnedin N. Y., 1996, ApJL, 472, L63

Ota K., et al., 2010, ApJ, 722, 803

Ota K., et al., 2014, The Astrophysical Journal, 792, 34

Ota K., et al., 2017, ApJ, 844, 85

Ouchi M., et al., 2008, ApJs, 176, 301

Ouchi M., et al., 2010, ApJ, 723, 869

Palla F., Salpeter E. E., Stahler S. W., 1983, ApJ, 271, 632

Partridge R. B., Peebles P. J. E., 1967, ApJ, 147, 868

Peebles P. J. E., 1982, ApJL, 263, L1

Pentericci L., et al., 2014, ApJ, 793, 113

Penzias A. A., Wilson R. W., 1965, ApJ, 142, 419

Perlmutter S., et al., 1999, ApJ, 517, 565

Pirard J.-F., et al., 2004, in Moorwood A. F. M., Iye M., eds, Society of Photo-Optical Instrumentation Engineers (SPIE) Conference Series Vol. 5492, Ground-based Instrumentation for Astronomy. pp 1763–1772, doi:10.1117/12.578293

Planck Collaboration et al., 2020, A&A, 641, A6

Polletta M., et al., 2007, ApJ, 663, 81

Press W. H., Schechter P., 1974, ApJ, 187, 425

Pritchet C. J., 1994, PASP, 106, 1052

Ramón-Pérez M., et al., 2019, A&A, 631, A10

Reddy N. A., Steidel C. C., 2009, ApJ, 692, 778

Riess A. G., et al., 1998, AJ, 116, 1009

Robertson B. E., 2022, Annual Review of Astron and Astrophys, 60, 121

Robertson B. E., Ellis R. S., Dunlop J. S., McLure R. J., Stark D. P., 2010, Nature, 468, 49

Rubin V. C., Ford W. K. J., Thonnard N., 1980, ApJ, 238, 471

Santos M. R., 2004, MNRAS, 349, 1137

Santos S., Sobral D., Matthee J., 2016, MNRAS, 463, 1678

Santos S., et al., 2020, MNRAS, 493, 141

Schaerer D., Boone F., Zamojski M., Staguhn J., Dessauges-Zavadsky M., Finkelstein S., Combes F., 2015, A&A, 574, A19

Schechter P., 1976, ApJ, 203, 297

Scoville N., et al., 2007, ApJS, 172, 1

Shapley A. E., Steidel C. C., Pettini M., Adelberger K. L., 2003, ApJ, 588, 65

Shibuya T., Kashikawa N., Ota K., Iye M., Ouchi M., Furusawa H., Shimasaku K., Hattori T., 2012, ApJ, 752, 114

Shibuya T., et al., 2017, Publications of the Astronomical Society of Japan, 70, S14

Shioya Y., et al., 2008, ApJS, 175, 128

Siebenmorgen R., Carraro G., Valenti E., Petr-Gotzens M., Brammer G., Garcia E., Casali M., 2011, The Messenger, 144, 9

Silk J., 1977, ApJ, 211, 638

Simard L., Mendel J. T., Patton D. R., Ellison S. L., McConnachie A. W., 2011, ApJS, 196, 11

Smolčić V., Novak M., et al., 2017, A&A, 602, A6

Sobral D., Best P. N., Matsuda Y., Smail I., Geach J. E., Cirasuolo M., 2012, MNRAS, 420, 1926

Sobral D., Smail I., Best P. N., Geach J. E., Matsuda Y., Stott J. P., Cirasuolo M., Kurk J., 2013, MNRAS, 428, 1128

Sobral D., et al., 2015a, MNRAS, 451, 2303

Sobral D., Matthee J., Darvish B., Schaerer D., Mobasher B., Röttgering H. J. A., Santos S., Hemmati S., 2015b, ApJ, 808, 139

Sobral D., Matthee J., Brammer G., Ferrara A., et al., 2017, preprint, (`arXiv:1710.08422`)

Sobral D., Santos S., Matthee J., Paulino-Afonso A., Ribeiro B., Calhau J., Khostovan A. A., 2018, MNRAS, 476, 4725

Sobral D., et al., 2019, MNRAS, 482, 2422

Somerville R. S., Hopkins P. F., Cox T. J., Robertson B. E., Hernquist L., 2008, MNRAS, 391, 481

Springel V., Hernquist L., 2003, MNRAS, 339, 312

Steidel C. C., Giavalisco M., Dickinson M., Adelberger K. L., 1996, AJ, 112, 352

Stott J. P., Smail I., Edge A. C., Ebeling H., Smith G. P., Kneib J. P., Pimbblet K. A., 2007, ApJ, 661, 95

Stott J. P., Pimbblet K. A., Edge A. C., Smith G. P., Wardlow J. L., 2009, MNRAS, 394, 2098

Stott J. P., Sobral D., Smail I., Bower R., Best P. N., Geach J. E., 2013, MNRAS, 430, 1158

Stroe A., Sobral D., 2015, MNRAS, 453, 242

Stroe A., Sobral D., Matthee J., Calhau J., Oteo I., 2017, MNRAS, 471, 2558

Sutherland W., Saunders W., 1992, MNRAS, 259, 413

Tadaki K.-I., Kodama T., Koyama Y., Hayashi M., Tanaka I., Tokoku C., 2011, , 63, 437

Takahashi M. I., et al., 2007, ApJS, 172, 456

Taylor E. N., et al., 2009, ApJS, 183, 295

Thorne J. E., et al., 2021, MNRAS, 505, 540

Tilvi V., et al., 2010, ApJ, 721, 1853

Tilvi V., et al., 2014, ApJ, 794, 5

Tilvi V., et al., 2020, ApJL, 891, L10

Toomre A., Toomre J., 1972, ApJ, 178, 623

Tresse L., Maddox S. J., 1998, ApJ, 495, 691

Vanzella E., et al., 2011, ApJL, 730, L35

Weaver J. R., et al., 2022, ApJS, 258, 11

Westra E., Jones D. H., 2008, MNRAS, 383, 339

Westra E., Geller M. J., Kurtz M. J., Fabricant D. G., Dell'Antonio I., 2010, ApJ, 708, 534

Wilkins S. M., Bunker A. J., Stanway E., Lorenzoni S., Caruana J., 2011, MNRAS, 417, 717

Wilkins S. M., Bouwens R. J., Oesch P. A., Labbé I., Sargent M., Caruana J., Wardlow J., Clay S., 2016, MNRAS, 455, 659

Wold I. G. B., et al., 2021, arXiv e-prints, p. arXiv:2105.12191

Wright A. H., Driver S. P., Robotham A. S. G., 2018, MNRAS, 480, 3491

Zakamska N. L., Strauss M. A., Heckman T. M., Ivezić Ž., Krolik J. H., 2004, AJ, 128, 1002

Zheng Z.-Y., et al., 2017, ApJL, 842, L22

van der Wel A., et al., 2011, ApJ, 742, 111